ANALYSIS AND DESIGN OF NOVEL DIPLEXING AND BEAMFORMING ANTENNA SYSTEMS FOR SATELLITE COMMUNICATIONS AND IOT APPLICATIONS

By:

Farzad Karami

Thesis Presented to

Département d’informatique et d’ingénierie

Université du Québec en Outaouais (UQO)

In partial fulfillment of the requirements for the degree of Doctor of Philosophy

Ph.D.

January 2025

Board of Examiners

This thesis has been evaluated by the following board of examiners:

Thesis Supervisor: Prof. Halim Boutayeb
Département d'informatique et d'ingénierie,
Université du Québec en Outaouais.

Thesis Co-Supervisor: Prof. Larbi Talbi
Département d'informatique et d'ingénierie,
Université du Québec en Outaouais.

Committee President: Prof. Michael Korwin-Pawlowski
Département d'informatique et d'ingénierie,
Université du Québec en Outaouais.

Internal Examiner: Prof. Tinko Eftimov
Département d'informatique et d'ingénierie,
Université du Québec en Outaouais.

External Examiner: Prof. Badr Eddine Ratni

Université Paris-Nanterre

This thesis was presented and defended in the presence of the board of examiners and the public on January 29, 2025, at the département d'informatique et d'ingénierie.

ABSTRACT

Microwave and millimeter-wave wireless systems have revolutionized communication technologies, driving innovation across domains such as satellite communications, smart transportation, and the Internet of Things (IoT). Operating within the 1–300 GHz spectrum, these systems enable ultra-high data rates, efficient spectrum utilization, and reliable connectivity, making them indispensable for emerging applications. However, the implementation of these systems faces significant challenges, requiring novel design approaches to address issues such as bandwidth efficiency, cost-effectiveness, and system compactness.

This doctoral thesis presents a series of innovative designs to overcome these challenges and advance the application of microwave and millimeter-wave systems. The first study introduces a compact Ku-band diplexing structure and a two-port directive end-fire antenna for high-speed railway networks, achieving high reliability and performance. The second study focuses on a multifunctional switched-beam architecture for vehicular-to-satellite communication, significantly enhancing scanning coverage and channel capacity. The third study develops a broadband millimeter-wave rat-race coupler based on parallel microstrip lines, covering the 20–42 GHz range, which is then applied to design a thin monopulse antenna system for space debris detection on satellite exploration missions.

These contributions address critical challenges in the design and implementation of next-generation communication systems, paving the way for high-performance, cost-effective solutions in cutting-edge applications. This work advances the state of the art in wireless communication and demonstrates the potential of microwave and millimeter-wave technologies to shape the future of connectivity, safety, and efficiency in diverse fields.

RÉSUMÉ

Les systèmes sans fil à micro-ondes et ondes millimétriques ont révolutionné les technologies de communication, stimulant l'innovation dans des domaines tels que les communications par satellite, les transports intelligents et l'Internet des objets (IoT). Opérant dans le spectre de 1 à 300 GHz, ces systèmes permettent des débits de données ultra-élevés, une utilisation efficace du spectre et une connectivité fiable, les rendant indispensables pour les applications émergentes. Cependant, leur mise en œuvre présente des défis majeurs, nécessitant de nouvelles approches de conception pour résoudre des problèmes tels que l'efficacité spectrale, la rentabilité et la compacité des systèmes.

Cette thèse doctorale présente une série de conceptions innovantes visant à surmonter ces défis et à faire progresser l'application des systèmes à micro-ondes et ondes millimétriques. La première étude introduit une structure de duplexage compacte en bande Ku ainsi qu'une antenne directive à rayonnement en bout à deux ports pour les réseaux ferroviaires à grande vitesse, garantissant une fiabilité et des performances élevées. La deuxième étude se concentre sur une architecture multifonctionnelle à faisceau commuté pour la communication véhicule-satellite, améliorant considérablement la couverture de balayage et la capacité des canaux. La troisième étude développe un coupleur hybride à large bande pour ondes millimétriques basé sur des lignes microstrip parallèles, couvrant la plage de 20 à 42 GHz, qui est ensuite appliqué à la conception d'un système d'antenne monopulse mince pour la détection de débris spatiaux lors des missions d'exploration satellitaire.

Ces contributions répondent à des défis cruciaux dans la conception et l'implémentation des systèmes de communication de prochaine génération, ouvrant la voie à des solutions performantes et économiques pour des applications de pointe. Ce travail fait progresser l'état de l'art en communication sans fil et démontre le potentiel des technologies à micro-ondes et ondes millimétriques pour façonner l'avenir de la connectivité, de la sécurité et de l'efficacité dans divers domaines.

ACKNOWLEDGEMENT

This thesis was conducted under the supervision of Prof. Halim Boutayeb and co-supervision of Prof. Larbi Talbi.

First and foremost, I would like to express my deepest gratitude to my supervisors for their unwavering support, patience, open-mindedness, guidance, and encouragement throughout my Ph.D. journey. Their expertise and insights have been invaluable in shaping both my research and my future career.

I am also sincerely grateful to my committee members, Prof. Michael Korwin-Pawlowski, Prof. Badr Eddine Ratni, and Prof. Tinko Eftimov, for their valuable insights and constructive feedback, which have greatly contributed to the refinement of my work.

Finally, I extend my heartfelt thanks to my parents and wife for their unconditional love and support throughout my Ph.D. studies. Their encouragement has been the foundation of my perseverance, making this journey possible.

DEDICATION

This thesis is dedicated to

My family and wife and friends

Contents

List of Figures

List of Tables

1 INTRODUCTION

In recent years, microwave and millimeter-wave wireless systems have spearheaded a remarkable revolution in the development of wireless technologies, paving the way for emerging applications across various domains. From the development of smart homes and cities, Internet of Things (IoT) devices, and satellite communications to electric vehicles and urban intelligent transportation systems, these advanced communication systems have ushered in a new era of connectivity, innovation, and efficiency. This doctoral thesis presents several novel designs of microwave and millimeter-wave wireless systems for driving forward emerging applications and shaping the future of wireless communication.

Microwave and millimeter-wave wireless systems represent cutting-edge technologies operating within specific frequency bands, each offering distinct advantages and capabilities. Microwave systems typically operate within the frequency range of 1 GHz to 30 GHz, while millimeter-wave systems extend from 30 GHz to 300 GHz. Millimeter-wave systems leverage high-frequency electromagnetic waves to transmit data wirelessly, enabling high-speed communication over short to medium distances. One of the distinguishing features of millimeter-wave systems lies in their ability to support ultra-high data rates, thanks to their wider bandwidth compared to microwave systems. However, both microwave and millimeter-wave technologies share common characteristics such as line-of-sight propagation, which is essential for point-to-point and point-to-multipoint communication, and advanced modulation techniques that ensure efficient spectrum utilization and reliable connectivity.

Microwave and millimeter-wave wireless systems play a crucial role in the new generation of satellite communications, enabling high-speed data transmission between ground stations, satellites, and spacecraft. These systems support a wide range of applications, including telecommunication, satellite internet services, earth observation, navigation, and remote sensing. Satellite-based microwave and millimeter-wave links provide global coverage and enable connectivity in remote or underserved areas where terrestrial infrastructure is limited or unavailable. Moreover, advancements in satellite technology have led to the development of constellations of small satellites, which leverage microwave and millimeter-wave communication to deliver broadband internet services to underserved communities and facilitate real-time monitoring of environmental phenomena such as climate change and natural disasters.

Furthermore, microwave and millimeter-wave wireless systems have been driving innovation in the automotive industry, particularly in the development of electric smart vehicles and public intelligent transportation systems. 5G and 6G wireless systems enable high-speed data exchange between vehicles, infrastructure, and cloud-based services, supporting a wide range of applications aimed at enhancing safety, efficiency, and the user experience. In the realm of electric smart vehicles, microwave and millimeter-wave systems facilitate vehicle-to-satellite and vehicle-to-vehicle communication, enabling features such as remote monitoring, satellite navigation, predictive maintenance, and autonomous driving. In such vehicles, new generation of wireless systems could play a critical role in traffic management, congestion mitigation, and infrastructure optimization. These systems could enable vehicles to communicate with satellites, highways' RFID tags, traffic lights, road signs, and other infrastructure elements, facilitating dynamic routing, adaptive traffic control, and collision avoidance. As a result, transportation networks become more resilient, efficient, and responsive to changing conditions, ultimately improving the overall mobility experience for commuters and travelers. Another emerging application of microwave and millimeter-wave systems is in the development of public transportation systems. Public transportation systems such as high-speed train (HST) networks need to provide high-data-rate services with the reliability of radio access for applications such as on-board and wayside high-definition (HD) surveillance, the network access of passengers, HD train dispatching video, and some smart devices and applications such as virtual reality and augmented reality [1-3]. Besides, providing high-speed and reliable wireless services for HST networks is so critical to tracking information and their public safety issues [4].

The implementation of microwave and millimeter-wave communication systems in each of the mentioned emerging applications faces serious challenges that require the design of new communication systems. In this thesis, new designs are introduced to implement efficient microwave and millimeter-wave systems for these emerging applications that efficiently address the challenges ahead. As the first study of this research project, first a diplexing structure will be presented for Ku-band applications. Then, by the proposed topology, a new, compact and low-cost two-port millimeter-wave diplexing directive end-fire antenna for high-speed railway wireless networks will be presented. As the second study, a multifunctional beam forming architecture for vehicular-to-satellite communication will be studied in detail. The proposed structure can radiate or receive multiple beams simultaneously. This system can significantly improve scanning coverage and channel capacity based on a switched beam methodology. As the third study, a novel mm-wave rat-race coupler with broadband operating bandwidth based on parallel microstrip lines will be presented. The useful practical bandwidth for this hybrid covers a frequency range 20-42 GHz for both sum and difference modes. Then, by using this mm-wave component, a novel thin mm-wave monopulse antenna system for detecting space debris on space missions will be presented.

2 State of The Art and Problem Definition

As mentioned earlier, with the simultaneous expansion of emerging technologies and the emergence of the fifth and sixth generations of wireless communication systems, new challenges have arisen for the designers of these systems, which may have been less noticed by anyone in the past. In the following, the challenges and problems addressed in this research project will be explained.

2.1 *Problem 1: High-Data-Rate Communication Services in High Speed Train Networks*

After the urban residential environments, high-mobility environments such as subways, and HSTs have registered the highest mobile data traffic and they have been among the most dynamic environments for using IoT [5]. According to International High-speed Rail Association, the current evolutionary trend of the world HST network reveals a very sharp increase in the rail length of the HST network. Statistics show that only in 2019, China's high-speed railway network transported over 2.2 billion passengers [6]. An explosive increase in the number of HST passengers has caused serious challenges to provide high-speed wireless communications to their consumers [7]. HST networks need to provide high-data-rate services with the reliability of the radio access for applications such as the on-board and wayside HD surveillance, the network access of passengers, HD train dispatching video, and some smart devices and applications such as virtual reality and augmented reality [8-10]. Besides, providing high-speed and reliable wireless services for HST networks are so critical to tracking information and their public safety issues [11].

Currently, high-speed railways are supported by some commercialized 4G communication services such as Mobile Worldwide Interoperability for Microwave Access (WiMAX) on rails [12], Long-Term Evolution (LTE) [13], LTE-Advanced (LTE-A) [14], and LTE for railways (LTE-R) [15]. All of these communication services are available below the 6 GHz frequency spectrum. For example, the LTE-R communication systems are usually designed at 0.45, 0.8, 1.4, and 1.8 GHz with an available bandwidth of about 20 MHz. Such narrow bandwidths are not adequate to meet the requirements of high-rate transmissions. Thus, they are not satisfying options to support high-data-rate IoT-based services in HST networks.

Therefore, it seems that HST communications infrastructure needs dozens of GHz of bandwidth to accommodate over 100 Gbps data rates [16]. The new generations of mm-wave 5G and beyond networks can support higher capacities (100-1000 fold compared to the current 4G networks), faster data speeds, as well as low latency, and high reliability [17-20]. All these reasons have motivated researchers to develop 5G HST communication systems at mm-wave frequencies. In some literatures, mm-wave bands such as 30 GHz, and 24-40 GHz are introduced as important bands to boast the transmission capacity in HST communications [21-23].

Each wireless communication system needs a critical component named antenna which must be low profile and low cost as well [24]. Recently, a few kinds of literature in the domain of IoT-based antennas have been reported which operate at different mm-wave frequency ranges [25-27]. Among them, a few works have focused on designing antennas for HST applications. In designing HST antennas, some requirements could be considered by designers. Since HST environments can be described as long and narrow tunnels that contain different scenarios like underground mines or subways [28], in such environments using end-fire antennas with high gain are quite essential to have an appropriate connection [29]. The end-fire antennas are utilized to propagate electromagnetic waves into free space along the direction of antenna extension [30-31]. In these antennas, the main direction of radiated EM waves is parallel with the antenna structure. End-fire antennas benefit from a great aerodynamic condition in practical applications such as HST networks, high-speed aircraft, missiles, and radars in comparison to broadside antennas [32].

Recently, a few studies on the development of mm-wave end-fire antennas have been conducted [33-34]. All these studies already introduced antennas that just could be used as one transmitter antenna or one receiver antenna. However, the HST industry requirement and its desire to achieve an on-board connected environment, for both customer and operational purposes, need for the installation of a wide variety of transmitting and receiving antennas on the rooftop of trains. Due to a physical size limitation on the rooftop of HSTs, the transmitter and receiver antennas often need to be installed in close proximity to each other. It can lead to revealing technical conflicts in installation, harmful interaction and interference between the transmitting and receiving signals, and also causes additional challenges in the terms of mutual coupling and correlation between the antennas [35]. Potentially, these conflicts can limit the performance of radio systems and raise serious concerns about safety and reliability.

In such circumstances, transceiver antenna systems can be a viable solution to overcome mentioned conflicts between transmitter and receiver antennas on the rooftop of trains. A transceiver antenna system refers to an RF device that can transmit and as well receive EM waves through a single antenna [36]. Actually, in a transceiver antenna, transmitting and receiving functions are served by a single antenna to reduce fabrication costs, conflicts between transmitter and receiver, the number of antenna elements, and hardware size as well. In this thesis, an end-fire transceiver antenna system with two separate frequency bands is presented for future HST communications as the first study. According to our best knowledge and the review done, it can be found that currently the 4G systems are used in high-speed trains, which cannot meet the increasing needs of users. Very limited research has been done on the development of new generation communication systems for high-speed trains, which do not cover all the needs of the railway industry. Considering the research gaps in this field, there is a lot of research potential for the design of millimeter wave transceiver systems.

2.2 *Problem 2: Multi-functional Antenna Systems for Vehicular to Satellite Applications*

Recently, there has been a rapid revolution in developing smart cities, electrical vehicles, intelligent transportation systems, and wireless sensor devices that significantly have affected human communities [37]. All aspects of our real lives could be gradually affected by billions of smart wireless devices [38-39]. On the other hand, by spreading modern technologies, many environmental problems have appeared through human activities, such as greenhouse gas emissions from burning fossil fuels and climate change [40]. Hence, developing clean, renewable, natural resources as sustainable energy sources for modern systems is becoming increasingly important as environmental problems worsen. In the newest generation of intelligent transportation systems and electric vehicles, it is essential to offer multifunctional systems that can integrate and obtain their power consumption via renewable energy sources [41-42].

Beamforming systems are widely used nowadays in modern wireless communication systems. In intelligent vehicular, the beamforming system is an example of a multifunctional reconfigurable system that can be used for space division and multiple access. The beamforming system can mitigate the multipath fading phenomenon by directing the radiation beam in the desired direction, thus minimizing interference and noise sources. These systems offer higher single-to-noise ratios (SNRs), better diversity gains, and faster data transmission rates. An antenna array should be cascaded with a beamforming network (BFN) in order to achieve a beamforming system [43]. A BFN produces the multibeam in desired directions by providing the required phase and amplitude to the radiating array elements [44]. Depend on multibeam applications, beamforming systems are categorized in two different types; 1D scanning and 2D scanning systems [45]. The desired BFN for 1D beam-scanning systems could be realized by Butler matrix [46], reflector system [47], or Rotman lens [48]. Among applied techniques for designing 1D beam-scanning systems, the Butler matrix is one of the most popular types of BFNs. With the balance of excitation and configuration flexibility, the Butler matrix has an advantage over other beamforming techniques reported in [49-50]. In addition, a Butler matrix requires fewer couplers and has a low design difficulty compared to other ones. Its theoretically loss-free structure and the use of the smallest number of components have led many studies to explore the Butler matrix.

In comparison with 1D scanning, 2D scanning offers higher beam steering resolution and greater versatility [51]. Leaky-wave antennas, whose radiation pattern is influenced by frequency manipulation, are one of the available approaches for adding one more dimension to scanning capability [52-53]. However, in the most of cases, it is not possible for communication systems to use beam-scanning properties that are frequency-dependent. 2D BFNs are another solution for generating 2D beams. Several 2D scanning methods are discussed in [54-55]. These methods could include passive network, active network, series-fed method, and mutual-coupled method. There appears that 2D scanning properties causes to become BFNs structure more complex. Hence, there are fewer studies on 2D scanning applications than on 1D scanning applications. Although beamforming systems have a number of advantages, whether they are 1D or 2D, such as higher throughputs and longer ranges, providing continuous energy supply remains as one of the biggest challenges for them that needs to be addressed.

In our ambient environment, there are a variety of energy sources to be harvested. These include solar energy, kinetic energy, electromagnetic energy, and thermal energy, all of which have different power levels and harvesting conditions. Simultaneously with the rapid progress of wireless technologies, radiofrequency (RF) energy harvesting has rapidly become a hot research topic [56]. Since electromagnetic (EM) waves are found in different directions of the urban environment, there has been considerable literature on EM energy harvesting and its rectifying technology. This application requires antennas to possess certain characteristics such as broadband [57], multifrequency [58], polarization-insensitive [59], and wide-angle coverage [60]. However, in an urban environment, the maximum RF power can reach approximately -50 dBm [61], and the current rectifier diodes cannot handle such low power levels. Even if we assume that diodes can rectify RF power with lower efficiency in these cases, the charge speed will be so slow that it will not satisfy the power requirements of the terminal equipment [62]. Solar energy is the best environment-friendly energy source to harvest. It is a renewable and never-ending energy source. Solar panels can capture and store the sun's energy. For the integration of RF antennas with solar panels, it is necessary to ensure that both antenna performance and harvesting energy are not adversely affected by each other [63]. In the RF/solar hybrid harvesting designs [64-67], solar panels have been placed on nonradiated surfaces of the antenna dielectric substrate. These surfaces are positioned where the antenna has a limited current distribution. Thus, solar panels and antennas don't interfere with each other on these surfaces.

The second study of this thesis proposes a new multifunctional device that is integrated with solar panels for the new generation of vehicular and advanced transportation systems. According to the best of our knowledge, there is no study on multi-beam antenna systems covered by solar panels for vehicular to satellite communication. Considering the research gaps in this area, there is great research potential for the aforementioned topics.

2.3 *Problem 3: Radar Systems for Detecting Space Debris in Satellite Exploration Missions*

Today, there are more than 6,000 artificial satellites orbiting the Earth. They mainly serve as communication devices between IoT devices, weather forecasting systems, remote sensing systems, GPS systems, imaging systems, and satellite Internet access [68-72]. In recent years, space debris has increased significantly as a result of the constant launch of artificial satellites. Due to this, artificial satellites are at a greater risk of colliding with space debris [73]. As the European Space Agency reported recently, space debris poses the greatest threat to future satellite communications and space exploration missions. In the meantime, the damage caused by space debris fragments larger than several centimeters could be more harmful. These space debris are like bullets that can destroy entire satellite systems in a matter of seconds. To address this pressing concern, smart systems are being developed to be installed on satellites to detect small fragments to maintain control and minimize damage caused by space debris.

Detection and monitoring of these fragments can be accomplished efficiently using radar techniques. Since the advent of space exploration in the 1960s, the monitoring and tracking of objects in Earth's orbit have been facilitated by advanced radar systems. Among the most widely employed tracking systems is monopulse radar, a technology that has played a pivotal role in detecting and characterizing targets in space [74]. The fundamental principle underlying monopulse radar involves the comparison of amplitude and phase signals received through both sum and difference beams. In this radar configuration, the sum beam is crafted to produce a radiation beam characterized by low sidelobe levels, optimizing its efficiency in target detection.

On the other hand, the difference beam is engineered to create a deep null in the boresight direction, providing precise angle information about the detected target [75].

A typical monopulse radar system comprises two key components: the comparator feeding network and the radiation component. The former is responsible for generating either a sum or difference mode, while the latter manages pattern diversity. In traditional monopulse radar systems, the comparators, such as rectangular waveguides and reflectors, and monopulse feeders, have been intricate and bulky. This complexity has resulted in challenges during assembly, making the overall system cumbersome and expensive [76]. However, recent advancements in radar technology have ushered in a new era with the development of monopulse antennas featuring planar structures. These structures, including substrate-integrated waveguides (SIW), microstrip lines, and strip lines, represent a departure from the traditional, costly, and bulky designs. The transition to planar structures offers several advantages, including a more compact form factor, increased affordability, and simplified fabrication processes. This evolution marks a significant leap forward in the quest for efficient and cost-effective monopulse radar systems, with the potential to enhance tracking capabilities while streamlining the manufacturing and deployment processes [77]-[78].

With the mentioned technologies, a comparator can be successfully realized by components such as different kinds of hybrid couplers, Magic-Ts, and phase shifters on single- or multi-layer substrates. However, these monopulse systems may suffer from reduced isolation and interference caused by spurious radiation caused by comparators, specially at higher frequencies. Moreover, these structures typically operate within a narrow operating bandwidth [79]. Furthermore, these systems often use broadside antennas. In detection and tracking systems that are carried by high-speed aircraft, missiles, and artificial satellites, end-fire radiation patterns are highly useful [80]. In end-fire antennas, electromagnetic waves are propagated into free space along the direction of antenna extension. In these antennas, the main direction of radiated EM waves is parallel to the antenna structure. Therefore, it seems that end-fire antennas could exhibit better aerodynamic performance than broadside antennas in the mentioned specific applications, especially in space missions [81]. In the tracking system of modern artificial satellites, single-layer monopulse antennas are increasingly required, as they could be able to integrate with microwave devices in a compact package and deliver excellent performance in detecting targets.

The aim of third study of this thesis is to design a wideband mm-wave monopulse antenna based on a thin single-layer Printed Circuit Board (PCB) laminate to produce the difference and sum patterns simultaneously. After doing an extensive literature review, and according to the best of our knowledge, there is a few studies on detecting space debris through mm-wave compact radar systems in space missions. Considering the research gaps in this area, there is a great opportunity to conduct more studies on the aforementioned topics.

3 Objectives

The goal of this research project is to propose novel microwave and millimeter-wave devices to address the problems ahead in emerging technologies. To this end, the following specific objectives are presented and described in details:

3.1 *Objective 1: Directive Millimeter-Wave End-Fire Diplexing Antenna for IoT Applications*

The first objective will be achieved through the following two parts:

- **Part I of Objective 1:**

In the first part of objective 1, an innovative technique for designing a diplexing circuit for Ku-band applications will be presented. The proposed structure is designed on multilayer PCBs and the utilization of a transition based on an extended SMA connector. The extended SMA connector provides two separate paths for the transmission of the RF signals. Hence, the proposed structure eliminates the need for intricate and bulky bandpass filters, allowing seamless integration with other planar devices and components within Ku-band satellite subsystems. Then, a new technique for integrating diplexers and power dividers will be proposed and validated experimentally at Ku-frequency.

- **Part II of Objective 1:**

In the second part of objective 1, the designed Ku-band diplexing circuit is extended to Ka-band frequency range. Then, a new, compact and low-cost two-port millimeter-wave diplexing directive end-fire antenna, which is designed, fabricated and tested, will be discussed in details. The proposed antenna system is made of a tapered slot antenna and a diplexing structure based on transitions in stacked PCBs. The proposed antenna system exhibits symmetric directive end-fire radiation patterns that are obtained experimentally, with low side lobe level and low front-to-back ratio. The performance of the proposed diplexing antenna make it suitable for high-speed railway wireless networks.

3.2 *Objective 2: Multifunctional Switched-beam Antenna Located on Solar Panels for Vehicular to Satellite Communication*

The second objective will be achieved through the following two parts:

- **Part I of Objective 2:**

In this part, a multifunctional beam forming architecture is proposed in detail for intelligent transportation systems and advanced vehicular technologies. The proposed structure can radiate or receive multiple beams simultaneously. This system can significantly improve the scanning coverage and channel capacity based on a switched beam methodology. The antenna has eight distinct ports to propagate eight beams at 28 GHz.

- **Part II of Objective 2:**

Nowadays, leading vehicular companies are developing an upcoming generation of electric vehicles (design concept). These smart vehicular are equipped with high-efficiency solar panel systems that cover their roofs. This surface covered with solar panels can generate a stable power supply for moving cars, allowing them to store enough energy. In the second part of object 2, an innovative study is proposed that aims to integrate an antenna propagation mechanism (part I) into the roof of the car in order to create a communication link with the sky. In such circumstances, signal propagation and solar energy harvesting should have minimal interaction in this link. In the second study of this thesis, a solar-powered multifunctional 2D beam-steering antenna system will be discussed in detail. The proposed multifunctional system can be installed on top of vehicles to create short- to medium-range communication links toward required system directions, including artificial satellites, drones, helicopters, and highway RFID tags. This architecture is capable of generating high-gain radiation patterns to cover a wide range of angles for an electronically controlled multifunctional unit. Sunlight energy harvesting, antenna propagation, beamforming, vehicular application, and communication toward the sky are among the multidisciplinary aspects of the structure.

3.3 *Objective 3: Millimeter-Wave Monopulse Radar System for Detecting Space Debris in Satellite Exploration Missions*

The third objective will be achieved through the following two parts:

- **Part I of Objective 3:**

Microwave hybrids 180 degrees (or rat-race couplers) are among the most suitable four-port microwave devices for providing phases 0 and 180 degrees in monopulse comparators and beamforming networks [82-84]. There are unique features in a rat-race component for dividing amplitude with phases 0 and 180 degrees. Frequency converters, mixers, balanced amplifiers, and push-pull amplifiers use rat-race couplers extensively. Despite their features, they are limited specially in mm-wave applications where wide operating bandwidth is required. Rat-race couplers are among the most critical components of monopulse radar systems and a limitation in their bandwidth can reduce the system operational bandwidth. In the first part of objective 3, a great deal of effort will be put into designing the perfect mm-wave rat-race couplers with increased bandwidth and a reduced circuit footprint. Then, an even-odd mode analysis of the proposed circuit will be presented in details.

- **Part II of Objective 3:**

In today's world, artificial satellites serve a variety of vital applications, ranging from communication and navigation to weather monitoring and scientific research. In the meantime, increasing space debris could threaten artificial satellites' functionality and safety. Currently, a large amount of space debris orbits the earth at high speeds, such as defunct satellites, rocket stages, and fragments from collisions with other objects. These debris particles can collide with operational satellites, damaging or destroying them. In addition to jeopardizing the billions invested in satellite technology, such collisions might also have broader implications. In response to this challenge, this part presents a novel thin mm-wave monopulse antenna system for detecting space debris on satellite missions. The proposed monopulse antenna system compares amplitude and phase signals received through both sum and difference beams, facilitating the detection of targets in space. The proposed system comprises a tapered slot antenna integrated with a mm-wave rat-race design on parallel transmission lines on a PCB with a thickness of 0.17 mm.

4 ORIGINALITY AND CONTRIBUTIONS

As described in section 2, while many studies can be found in the literature on microwave and millimeter-wave devices, there is only a few studies on problems aforementioned for emerging applications. Therefore, the current research project addresses this research gap by evaluating the problems ahead designers from different perspectives, proposing novel topologies, and validating them using fabrication and measurement. The contributions of the objectives in this research project are presented in the following.

4.1 *Directive Millimeter-Wave End-Fire Diplexing Antenna for IoT Applications*

The contributions of each part of the first objective of this research project can be listed as follows:

Part I of Objective 1:

- Designing a diplexing circuit without using bulky bandpass filters or complex circuits.
- Proposing a Ku-band diplexing power divider.
- Validating the performance of the proposed component by fabricating prototype and measuring parameters.

Part II of Objective 1:

- Developing and proposing a novel IoT-based diplexing antenna system for transferring/receiving applications in HST networks;
- Validating the performance of the developed system with fabricating prototype and measuring parameters.

4.2 *Multifunctional Switched-beam Antenna Located on Solar Panels for Vehicular to Satellite Communication*

The contributions of each part of the second objective of this research project can be listed as follows:

Objective 2:

Part I of Objective 2:

- Proposing a multi-beam antenna system with 2-D beam scanning capabilities.
- Developing the proposed multi-beam system to integrate with solar panels for using in electric vehicular technologies.

Part 2 of Objective 2:

- Conducting an analysis of the effects of solar panels on antenna's radiation performance.
- Validating the proposed system performance with fabricating a prototype and measuring parameters.

4.3 *Millimeter-Wave Monopulse Radar System for Detecting Space Debris in Satellite Exploration Missions*

The contributions of each part of the third objective of this research project can be listed as follows:

Part I of Objective 3:

- Proposing a mm-wave rat-race coupler with broadband operating bandwidth based on parallel microstrip lines.
- Conducting an even-odd mode analysis on the proposed rat-race coupler.

Part II of Objective 3:

- Proposing a millimeter-wave broadband monopulse radar antenna for space debris detection.
- Validating the performance of the proposed system with fabricating prototype and measuring parameters.

5 METHODOLOGIES

5.1 *Analysis and Design of a Diplexing Power Divider for Ku-Band Satellite Applications*

Authors: Farzad Karami, Halim Boutayeb, Ali Amn-e-Elahi1, Larbi Talbi1, and Alireza Ghayekhloo

[85]: Journal Sensors MDPI, Impact factor: 4.1

5.1.1 Abstract:

In dual-band RF front-end systems, to transmit different frequency signals in different paths, each path requires the power to be divided along two transmission channels. In such systems, a circuit is created in which the input ports of power dividers with different frequency bands are connected to the output ports of a diplexing circuit in a cascade form. These circuits often contain different band filters in their schemes and have a complicated design. In this paper, an innovative technique for designing a diplexing power divider for Ku-band applications is presented. The proposed structure is designed on multilayer PCBs and the utilization of a transition based on an extended SMA connector. The extended SMA connector provides two separate paths for the transmission of the RF signals. Hence, the proposed structure eliminates the need for intricate and bulky bandpass filters, allowing seamless integration with other planar devices and components within Ku-band satellite subsystems. In fact, the proposed architecture channelizes the divided output electromagnetic signals into two separate frequency spectrums. With the presented technique, two frequency ranges are envisaged, covering Ku-band applications at 13–15.8 GHz and 16.6–18.2 GHz. With the proposed structure, an insertion loss as low as 1.5 dB was achieved. A prototype of the proposed power divider diplexing device was fabricated and measured. It exhibits a good performance in term of return loss, isolation and insertion losses.

5.1.2 Introduction:

Recent years have seen the development of highly integrated multifunction devices as an effective means of high-performance and low-cost solutions. Incorporating solar panels into electronic devices is a prime example of multifunctionality [86]. This approach is particularly crucial in space communication when sunlight energy harvesting is required [87-88]. Power dividers and diplexers are pivotal elements in RF systems and instruments. They find extensive application in novel space telecommunications for segregating dual communication pathways. In wireless systems, power dividers are commonly used for power division and power combining with proper isolation and frequency filtering features [89]-[93]. Diplexing circuits play a significant role in transceiver front-end wireless systems. They can effectively separate Tx/Rx channels connected to common wideband or dual-band antennas [94]-[97]. Therefore, a diplexer technique can be employed to accommodate a system with multiple frequency bands and multiple functionalities. They can be used, for example, in a deep space probe antenna system, in which the transmit and receive signals are divided to cover a wide communication delay and the space probes are assumed to be far from Earth [98]. Diplexing circuits provide essential filtering characteristics and isolation between Tx and Rx channels in multi-input and multi-output services for a space link. In this scenario, diverse communication links are harnessed to transmit or receive signals from the deep space probe. This covers extensive distances while minimizing potential interference [99-100].

Diplexers are often designed using two bandpass filters with coupled resonators or cavities [101]-[104]. However, using a combination of low-pass and high-pass filters rather than two bandpass filters is preferable in some cases where the relative bandwidth of the transmit and receive channels is large [105]. Conventional diplexers are usually designed by using a rectangular waveguide, metal cavity junctions, or gap waveguide topologies to achieve desirable filtering performance [106]. However, when implemented in a practical array of probe antennas, these configurations can be cumbersome, heavy, and financially challenging [107], particularly in the context of space explorations in the future.

One of the main challenges for modern circuit designers is to design high performance, modular, and integrated microwave components with a compact topology [108]-[110]. Several researchers have been focused on designing planar diplexing systems [111-112]. Certain types among them necessitate the utilization of the low-temperature cofired ceramic (LTCC) fabrication process to attain a more compact (packed) and densely arranged (miniaturized) device. Other types of these components employ microstrips, striplines, planar traces, and coplanar waveguides (CPW). Typically, these components comprise a duo of bandpass filters functioning in distinct frequency bands, interconnected through a distribution network [113]-[115]. These combined distribution networks often occupy considerable space and lead to increase the overall size of the circuits. Although these planar architectures present good performances at lower frequencies, they strongly suffer from undesired emission and radiation at high frequencies.

Substrate integrated waveguide (SIW) is a renowned and currently well-established technological planar platform for RF, microwave, and millimeter-wave communication systems [116]-[118]. SIW is the most effective alternative to traditional microstrip or coplanar waveguides at high frequencies with extra performance. They have many features of rectangular waveguides, with the advantage of a low-cost fabrication process based on regular PCB technology [119]. SIW technology has found application in the design of various microwave and millimeter-wave components, such as filters, sensors, and reconfigurable electronics [120]-[122]. This technology offers compact dimensions, cost-effectiveness, high quality, and exceptional performance. To develop SIW duplexing devices (means the separation function of transmission and reception), a T-junction is often required to provide the matching and isolation requirements between the input port and two separate channel filters. This T-junction occupies a certain space in architecture [123]. Dual-mode duplexing can remove T-junction size overhead while maintaining design flexibility and performance improvement. These structures have a compact size, but suffer from a narrow operating bandwidth.

Designing high-performance and compact components with integration and modularity features for radio frequency front ends is highly desirable in many communication systems [124]. The concept of modularity presents a promising avenue for seamlessly integrating cutting-edge electronics, an apt approach to the cost-effective implementation of fully tailored and adaptable electronic devices. By embracing modularity, the capacity to assemble and integrate individual modules with distinct functionalities provides a flexible framework for crafting customized and responsive electronic systems that align precisely with specific requirements. This approach not only streamlines the development process but also can significantly reduce costs associated with intricate electronic device realization [125-126]. A lot of interest has been attracted to the integration of multifunctional microwave components, such as multiband and filtering dividers [127-130], diplexer antennas [131-134], etc. In long-distance communication systems, low-profile diplexing devices are paramount. These devices play a pivotal role in efficiently guiding and separating electromagnetic signals along designated pathways. By integrating these compact and versatile diplexers into the communication infrastructure, the transmission and reception of signals across long distances are optimized. This optimization is achieved by strategically channelling distinct frequency bands through the diplexing components. This enhances the overall efficacy and reliability of the communication system. The utilization of these diplexing devices improves signal management and reduces interference and signal degradation. This ensures seamless and dependable long-distance communication. The integration of these components with power dividers could benefit from size reduction and loss reduction of antennas used, for example, in deep space telecommunications.

The following section presents the analysis and design of an innovative compact Ku-band SIW duplexing power divider. The proposed concept is based on extended SMA connectors, which are used as a transition between two stacked SIW channels. This innovative approach aims to achieve improved signal integrity and efficient signal propagation in Ku- band frequency applications. The proposed transition behaves like two pairs of bandpass filters effectively separating the channels. However, the unique aspect lies in its compact size, which the occupied size is much smaller than the size of two regular bandpass filters. The developed duplexing power divider has a simple topology and shows a great potential for excellent integration with other planar components.

5.1.3 Geometry of the Proposed Diplexing Structure and Performance Analysis:

5.1.3.1 Overall Structure:

The geometry of the proposed SIW diplexing network is depicted in Figure 1, encompassing all aspects of design, layers, and the advanced SMA port. It is composed of two stacked SIW channels from top to bottom, including two Ro 4003c PCB laminates (εr = 3.55 and $\tan\delta$ = 0.0027). Both PCB laminates have the same height of 1.6 mm.

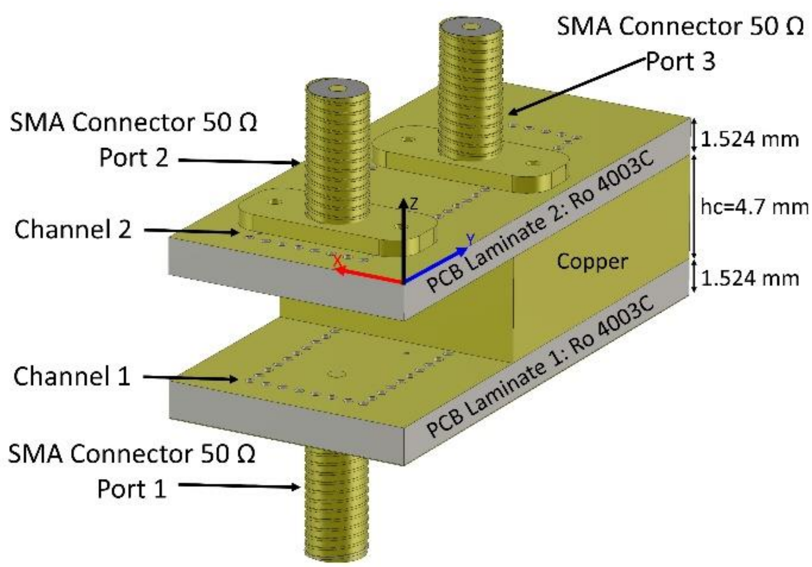

(a)

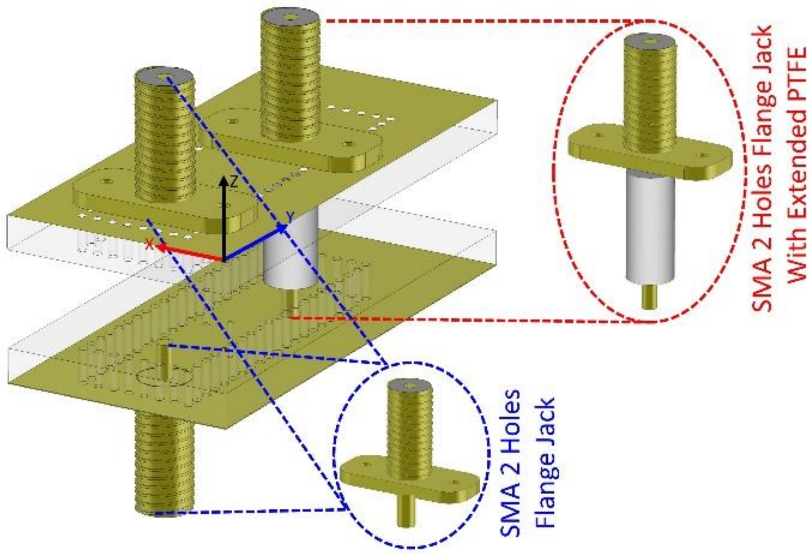

(b)

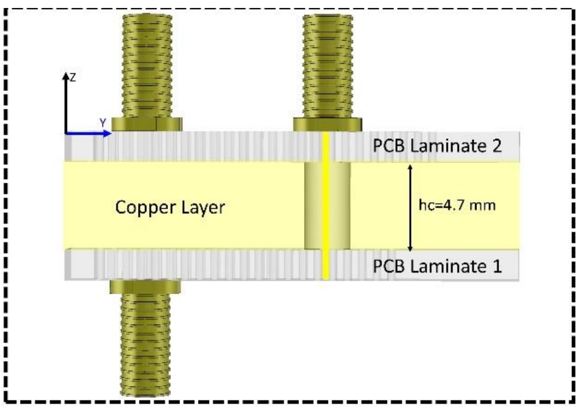

(c)

(d)

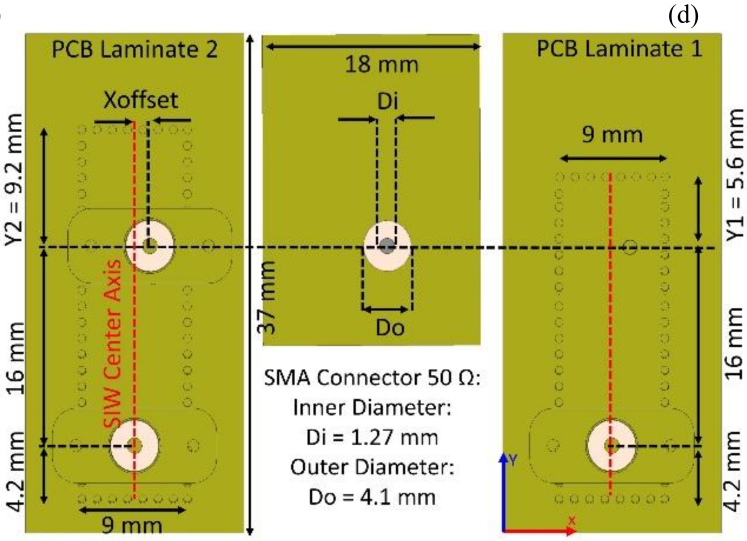

(e)

Figure 1. Different views of the proposed diplexing network. (a) Full view schematic, (b) without copper layer (in place material) view, (c) side view, (d) view of the advanced SMA connector with extended dielectric, and (e) top view of each layers (All dimensions are in mm).

There is a whole copper layer between the two PCB laminates, which thickness is 4.5 mm. Figure 1(a) shows the complete geometry of the proposed structure. In Figure 1(b), the copper layer has been hidden for a better view of the internal connections in the proposed structure. The top view of PCB laminates and the copper layer is shown in Figure 1(e). The proposed structure has three ports, which are numbered 1, 2, and 3. Ports 1 and 2 are made with two 50-ohm typical SMA connectors, as shown in Figure 1(b) with blue arrows. Port 3 is implemented using an SMA connector of 50 Ohms with an extended dielectric. The side view of the proposed structure is shown in Figure 1 (c). The end pin of SMA connectors 1 and 2 are soldered in the center of the SIW channel axis. Connector 3 has an extended dielectric, as shown in Figure 1 (d). The extended dielectric SMA port is the prepared interface that seamlessly penetrates the central copper layer without interference. The material of this dielectric is PTFE (εr = 2.1 and tanδ = 0.0002). The PTFE dielectric is 4.5 mm long. It can be easily removed from the connector metallic pin for the structure assembly. The cylindrical dielectric has an inside diameter of 4.1 mm, and an outside diameter of 1.27 mm. Figure 1(d) illustrates the extended dielectric and its connector together.

The proposed diplexing network is made up of three stacked PCB layers, as can be seen in Figure 1. The primary component of the suggested architecture is the vertical transition. The transition starts at the top layer, and its end is soldered to the bottom copper layer. In this structure, the cut cylindrical PTFE (shown in figure 1(d)) is placed inside a hole made in a copper layer. In the copper layer, there is a hole whose diameter is 4.1 mm (the same as the outer diameter of PTFE). The copper layer serves as a protective electromagnetic shield for the PTFE-covered conductor. The termination point of SMA connector pin 3 involves soldering it to the lower ground of the PCB's bottom layer, following its traversal through the first PCB layer, the copper layer, and eventually the lower PCB layer. This meticulous arrangement ensures optimal signal integrity and grounding in the design. In contrast to connectors 1 and 2, connector 3 is not located on the central axis of the SIW channel. The distance between SMA connector 3 and the SIW center axis is 3.2 mm.

5.1.3.2 Analysis:

In the proposed design, signals between SIW channels are then divided or separated by shifting the vertical transition from the central axis to the narrow walls of SIWs. Dividing or separating electromagnetic signals between SIW channels depends on the position of the SMA connector 3. By relocating SMA connector 3 from the center of the SIW axis to its walls, the suggested topology modification has the potential to alter transition behavior significantly. Illustrated in Figure 2 are the scattering parameters of SMA connector 3, demonstrating an extended dielectric connector's role as a via coupling topology when situated along the central axis of the SIW. In this particular arrangement, the RF signal undergoes a division between SIW channels 1 and 2. Assigned as the input port, port 3 serves as the point of entry for the RF signal, which subsequently gets distributed between the two aforementioned SIW channels (channels 1 and 2). This configuration showcases how the placement of SMA connector 3 along the SIW axis center can facilitate signal division and coupling through the extended dielectric connector. It is important to note that this arrangement holds implications for signal distribution and interaction within the SIW structure. Engineers and designers can leverage this insight to optimize signal routing, distribution, and interaction within the SIW, thereby tailoring the topology to specific performance objectives. The coupling values between the two output ports exhibited a notable similarity, while the reflection coefficient of port 3 was sufficiently low.

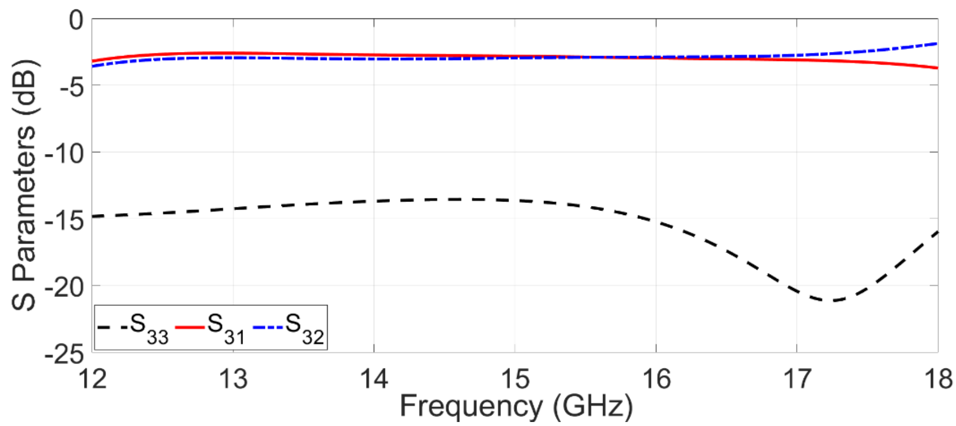

Figure 2. Simulated S-parameters of the proposed structure if the vertical transition is positioned at the SIW center axis.

By moving the transition toward the SIW walls, a distinct separation of electromagnetic signals emerges, channeling them into channels 1 and 2 at varying frequency bands. For the optimization, parameters Hs, Xoffset, Y1, and Y2 are changed. These four parameters have the most effect on scattering parameters. By working on these parameters, shifts occur in the values of inductance, capacitive reactance, and conductance within the impedance characteristics of the system. To determine the optimal values for these key parameters, comprehensive full-wave simulations employing CST software were executed. An evaluative exploration is undertaken through a parametrical analysis, depicted in Figure 3, showing the impact of these parameters. Notably, only a singular parameter is altered in each analysis iteration, maintaining constancy across all other parameters. Between these parameters, it seems that Hs, Y1, and Y2 cause to shift S_{33}, S_{31}, and S_{32}, respectively.

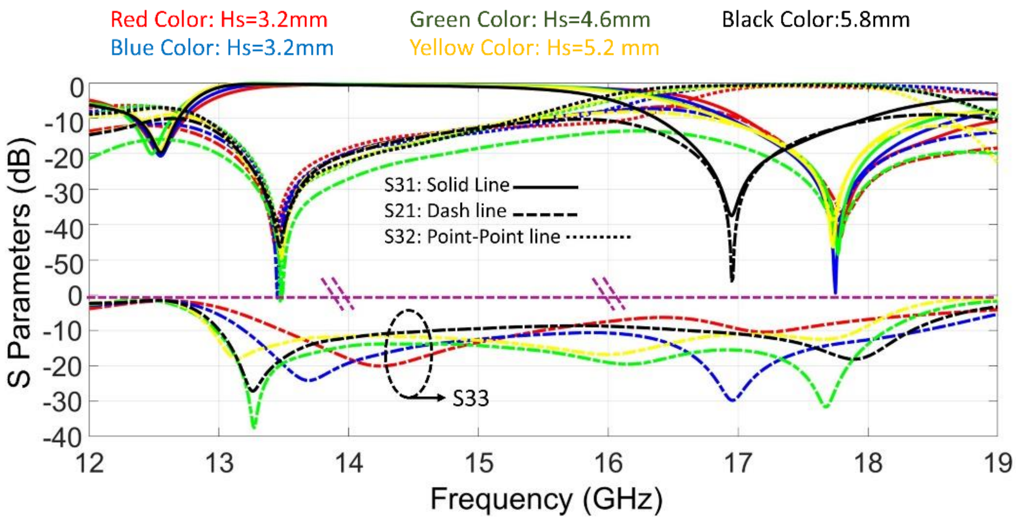

Red Color: Hs=3.2mm
Blue Color: Hs=3.2mm
Green Color: Hs=4.6mm
Yellow Color: Hs=5.2 mm
Black Color:5.8mm
S31: Solid Line
S21: Dash line
S32: Point-Point line
S33
S Parameters (dB)
Frequency (GHz)

(a)

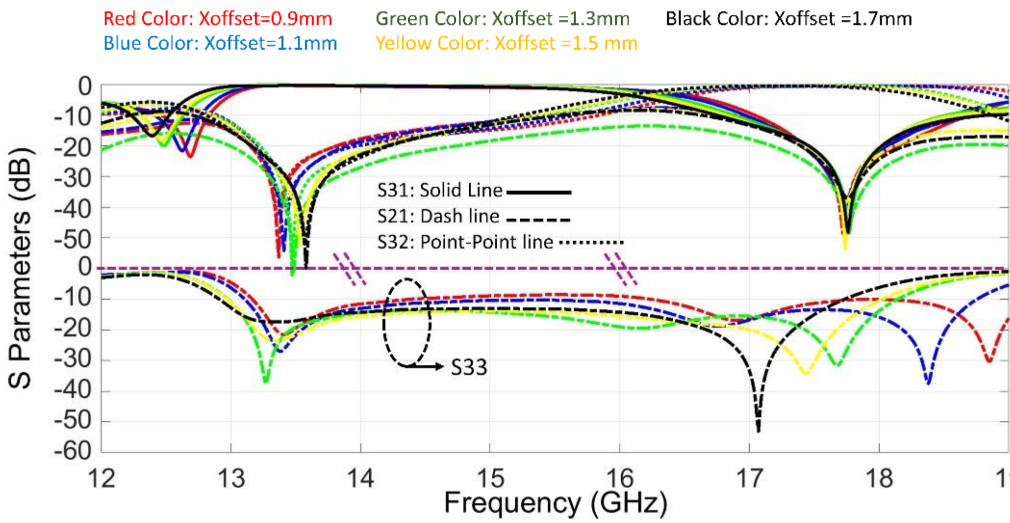

Red Color: Xoffset=0.9mm
Blue Color: Xoffset=1.1mm
Green Color: Xoffset =1.3mm
Yellow Color: Xoffset =1.5 mm
Black Color: Xoffset =1.7mm
S31: Solid Line
S21: Dash line
S32: Point-Point line
S33
S Parameters (dB)
Frequency (GHz)

(b)

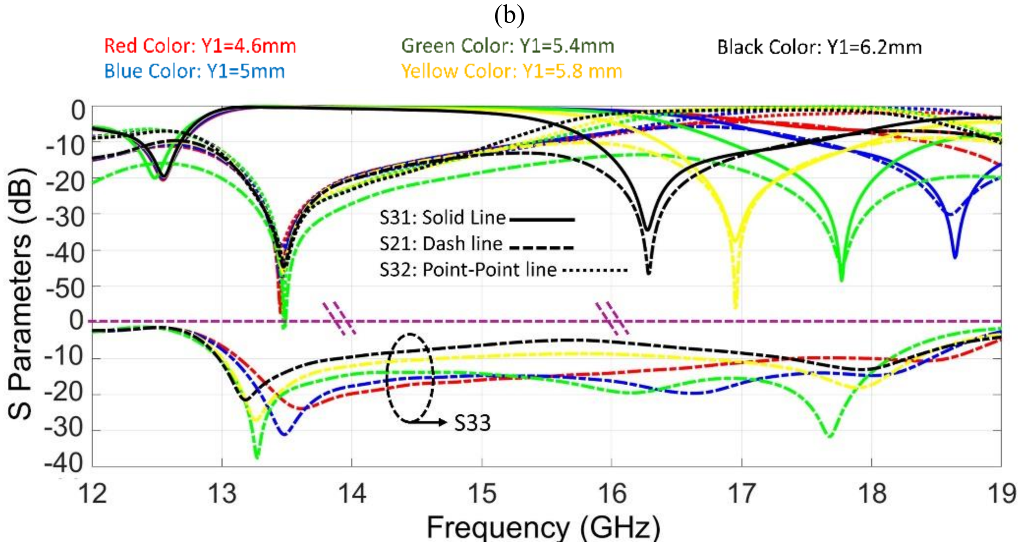

Red Color: Y1=4.6mm
Blue Color: Y1=5mm
Green Color: Y1=5.4mm
Yellow Color: Y1=5.8 mm
Black Color: Y1=6.2mm
S31: Solid Line
S21: Dash line
S32: Point-Point line
S33
S Parameters (dB)
Frequency (GHz)

(c)

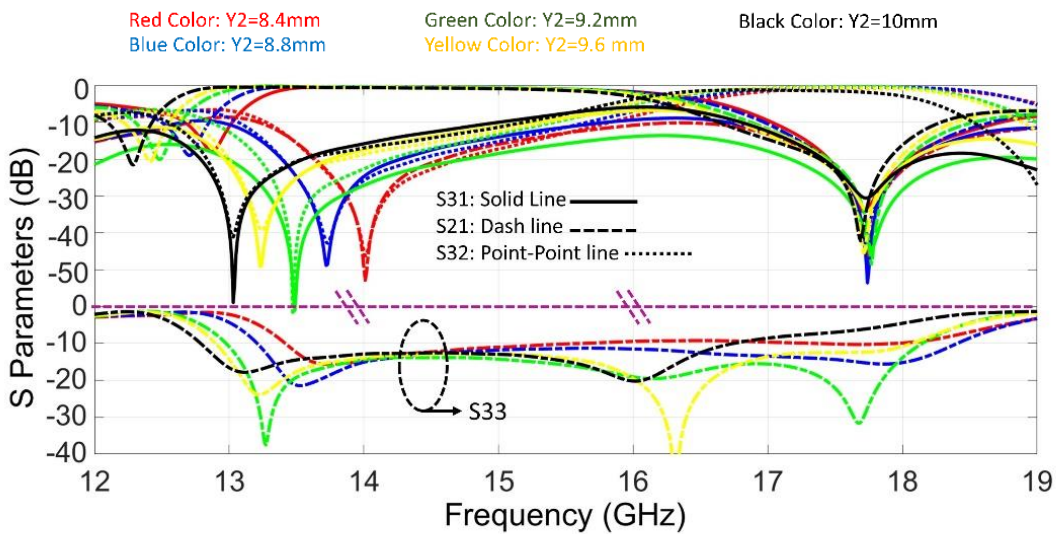

(d)

Figure 3. Parametric studies of the proposed structure. (a) Different values of thickness of copper layer, Hs from 3.2 to 5.8 mm. (b) Different values of Xoffset from 0.9 to 1.7 mm. (c) Different values of Y1 from 4.6 to 6.2 mm. (d) Different values of Y2 from 8.4 to 10 mm. (Solid Lines, Dash Lines, and Point-Point Lines present the S_{31}, S_{21}, and S_{32} parameters respectively, while the Dash circle specifies charts for S33).

Figure 4 illustrates the distribution of the electric fields on the SIW channels at 14 GHz (low-frequency band) and 17 GHz (high-frequency band) of the diplexing net-work. In this case, the mechanism's topology can be comprehended. If port 1 is excited in the low-frequency band, the RF signal first propagates in SIW channel 1. After that, the propagated signal is vertically transitioned by the proposed transition. Once the signal is propagated into the vertical transition, port 3 becomes active. In this configuration, no RF signal propagates into SIW channel 2. Channels 1 and 2 are thus isolated from one another. If port 2 is excited in the high-frequency band, the RF signal is transmitted in SIW channel 2, and it enters the proposed vertical transition at the end of channel 2. After that, it reaches the vertical transition, and port 3 becomes active. In this configuration, no RF signals pass through SIW channel 1. Channel 1 and channel 2 are therefore again isolated.

Likewise, by exciting port 3 with a wide-frequency band signal, signals within SIW channels 1 and 2 are propagated across distinct frequency bands. The vertical transition channelizes the RF signal between SIW channels 1 and 2 if port 3 is excited.

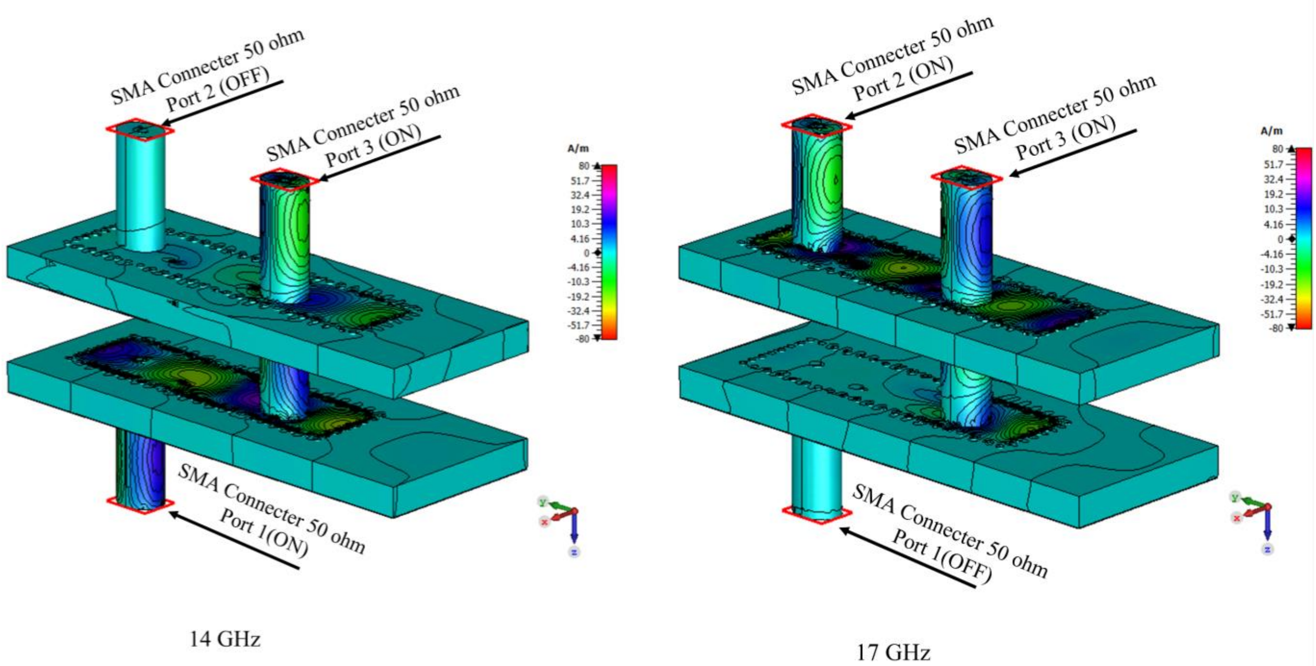

(a) (b)

Figure 4. Simulated electric field distribution for proposed architecture and two different frequencies; (a) when exiting port 1, and (b) when exiting port 2.

The simulated scattering parameters (S-parameters) of the optimized diplexing network are graphically depicted in Figure 5. Within this representation, it becomes evident that the lower channel (SIW channel 1) demonstrates an insertion loss of less than -1.5 dB, spanning the frequency range of 13 to 15.8 GHz, which corresponds to approximately 19.45% of the total bandwidth (Figure 5(a)). Concurrently, in the frequency interval of 16.6 GHz to 18.2 GHz, encompassing about 9.3% of the bandwidth, the upper channel (SIW channel 2) exhibits an insertion loss also below -1.5 dB (Figure 5(b)).

Further analysis of the simulation reveals matching bandwidths for amplitudes of S11 and S22 that are less than -10 dB. Specifically, the optimized diplexing network presents a matching bandwidth of around 20%, spanning from 12.6 to 15.4 GHz, for S11. For S22, the corresponding matching bandwidth covers a range of approximately 9.15%, spanning from 16.7 to 18.3 GHz. These findings underscore the effectiveness of the optimized network in achieving favorable insertion losses and suitable matching band-widths, thereby substantiating its potential for efficient diplexing operations.

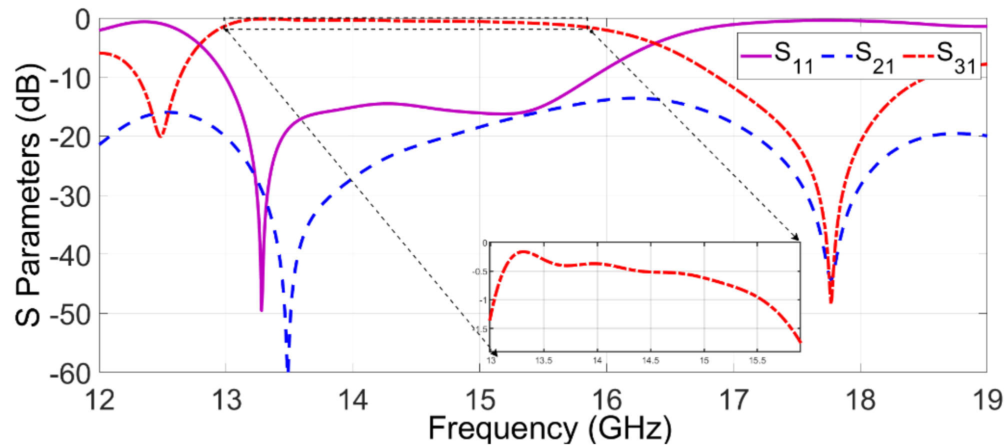

(a)

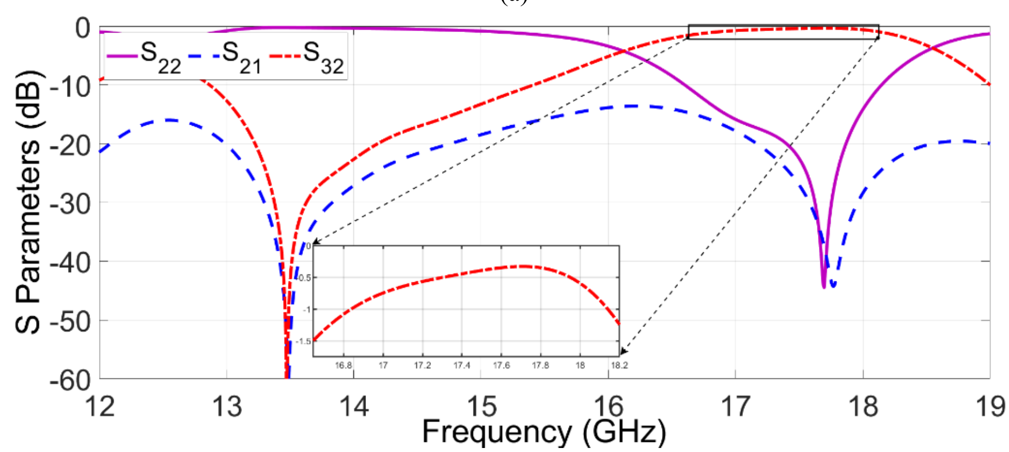

(b)

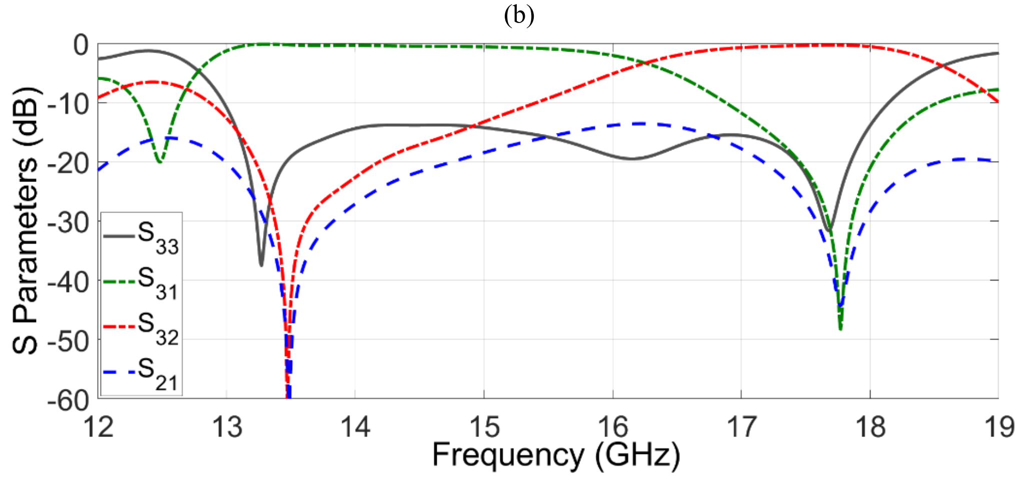

(c)

Figure 5. Simulated scattering parameters for the proposed diplexing structure. (a) Port 1 is excited. (b) Port 2 is excited. (c) Port 3 is excited.

5.1.4 Diplexing-Power Divider: Design and Performance:

The geometry of the proposed diplexing structure demonstrates its seamless integration potential with various planar microwave components, serving as a versatile modular device. This integration capability positions it favorably for inclusion in communication systems such as space applications when the necessitating dual operating frequency bands are met. The configuration of the ultimate diplexing power divider is depicted in Figure 6. This arrangement involves the interconnection of two pairs of Y-junction power dividers with the output ports of the aforementioned diplexing structure. In Figure 6(a), the output ports for each power divider are denoted as SMA connectors 3 and 4. Notably, the structure geometry was optimized using the CST software suite.

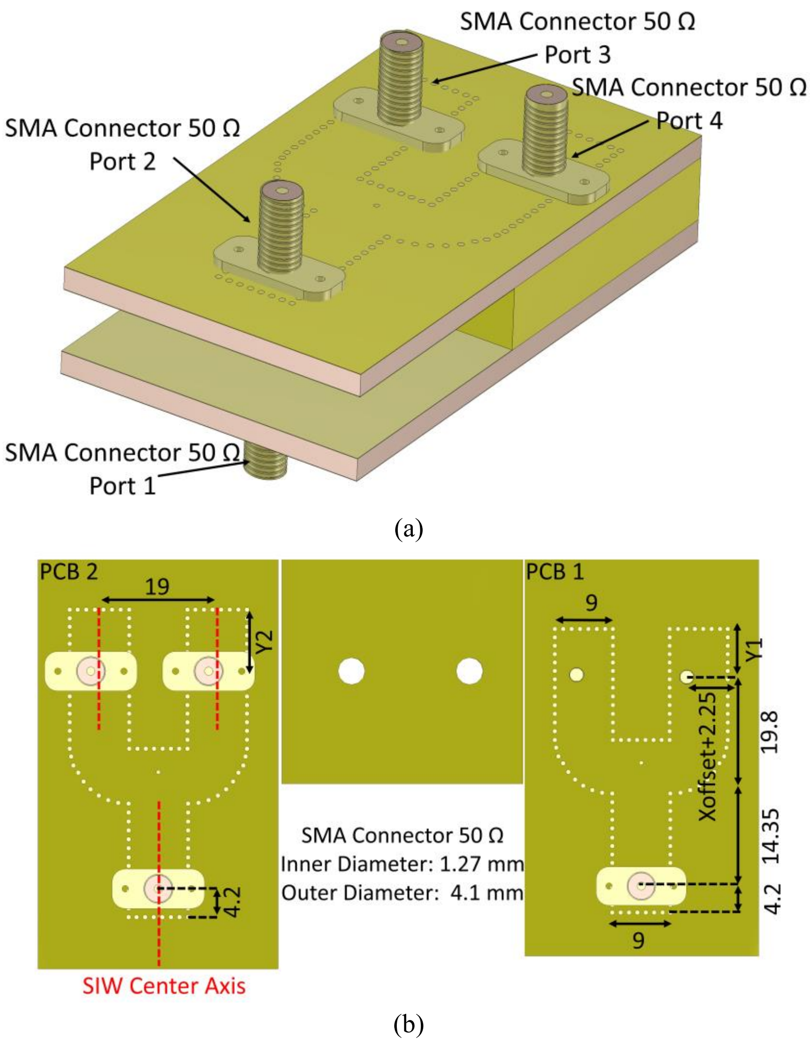

Figure 6. Different views of the final diplexing-power divider system working at Ku frequency band. (a) Configuration of the proposed architecture, and (b) top views of each layer (All dimensions are in mm). (Xoffset: 1.7mm, Y1: 5.9mm, Y2: 10.1mm)

The simulated S-parameters of the proposed diplexing-power divider are presented in Figure 7, originating from the simulation software. They show that the amplitude of the transmission coefficients from port 1 to port 3 or 4 surpasses the -4.5 dB threshold (Figure 7(a)). The same result is obtained when observing the transition from port 2 to ports 3 and 4 (Figure 7(b)). Given the inherent necessity to distribute power across two distinct ports, we can conclude that the achieved insertion loss was less than 1.5 dB. The impedance bandwidths for amplitudes of S_{11} and

S_{22} less than -10 dB are 10.2% (13 GHz to 14.4 GHz) and 9.2% (16.6 GHz to 18.1 GHz), respectively.

Isolation between uncoupled ports (ports 1 and 2) is more than 17 dB in the low-frequency band and more than 15 dB in the high-frequency band, based on the achieved charts in Figure 7. If port 1 is excited in the low-frequency band, the RF signal propagates into the lower power divider. After that, the propagated signal is vertically transitioned into the vertical transition. Once the signal is propagated into the vertical transition, ports 3 and 4 become active. The amplitude and phase of the signal at ports 3 and 4 are equal. In this situation, ports 1 and 2 are isolated from one another. On the other hand, if port 2 is excited in the high-frequency band, the RF signal is transmitted in the top power divider and it enters the vertical transition at the end of the top power divider. After it reaches the vertical transition, ports 3 and 4 become active. In this configuration, channel 1 and channel 2 are again isolated.

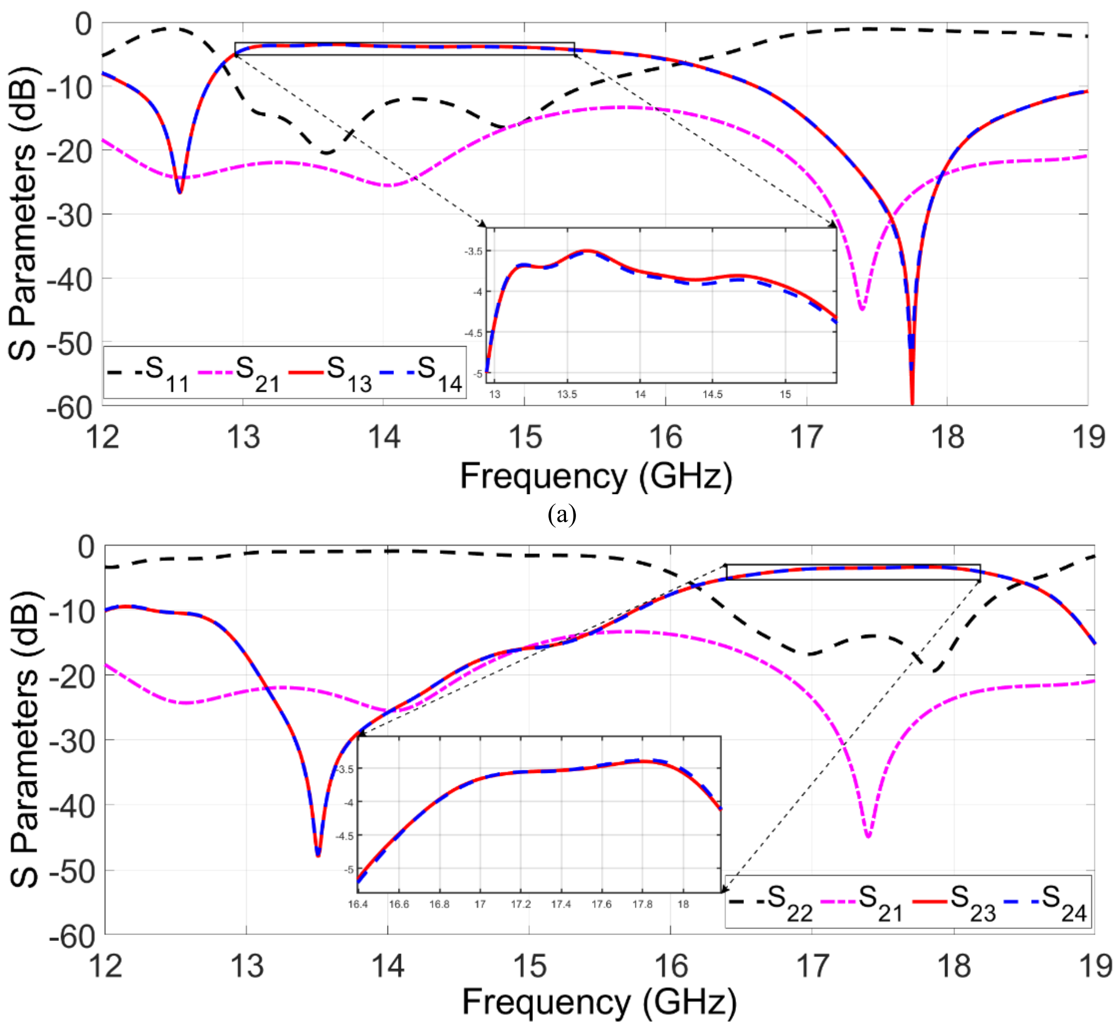

Figure 7. Simulated S-parameters for the final diplexing power divider. (a) Excitation of port 1, and (b) the case of exciting port 2 as the input signal source.

For further assessment of the operational dynamics of the final power divider employing this compact module, an analysis of electric fields and their trajectories is prepared in Figure 8. In particular, Figure 8(a) portrays the scenario wherein port 1 serves as the designated input port, effectively isolating it from any potential interference between port 2. This configuration illuminates the transmission path of the wave reaching the output ports with equitably distributed power. Similarly, Figure 8(b) captures another electric field distribution path. This time port 2 is the input source and equal power is divided between the two outputs and no coupling to the other input connector is observed.

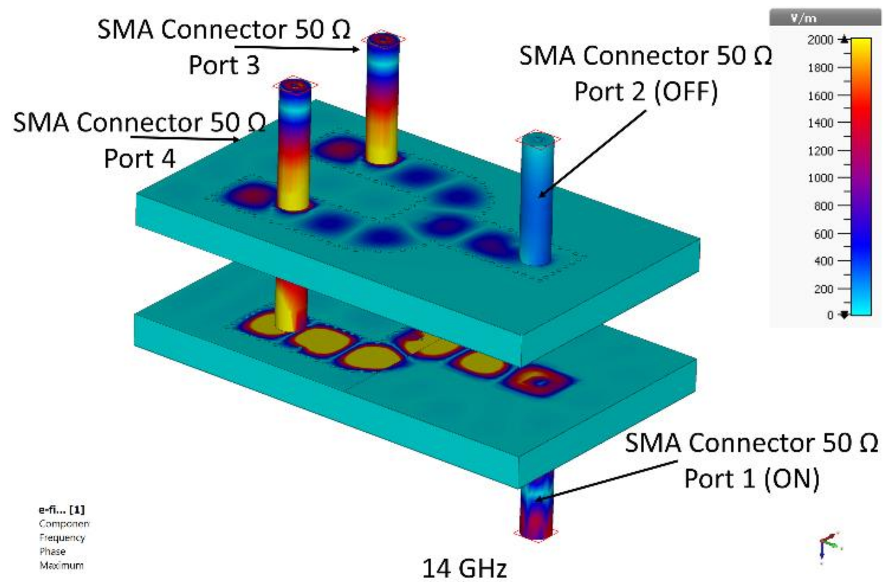

(a)

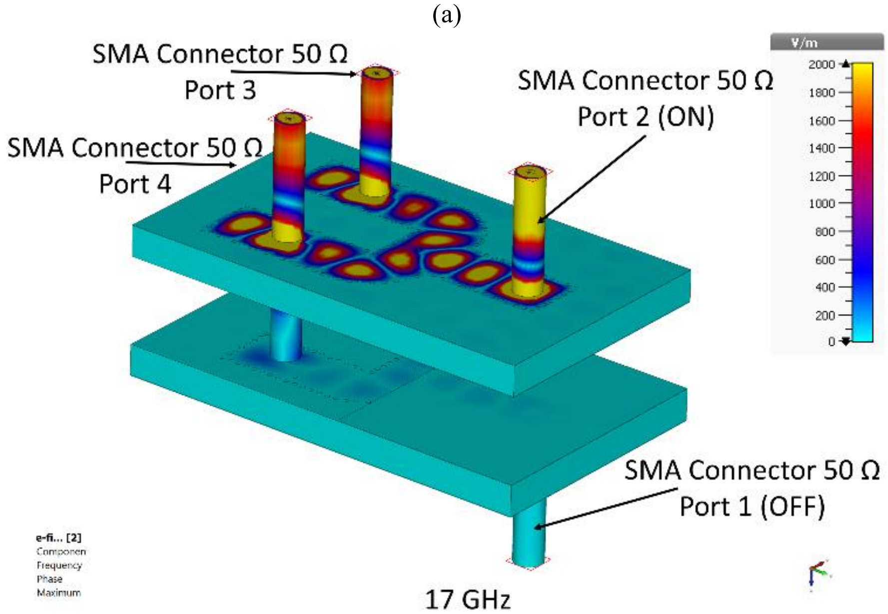

(b)

Figure 8. Simulated electric field distribution for proposed diplexer-power divider for different frequencies. (a) Exiting port 1. (b) Exiting Port 2.

As the last step towards validating the simulated performance of the proposed diplexer-power divider, a tangible prototype was fabricated and tested, as shown in Figure 9. During the assembly process, the layers are placed on top of each other and then screwed together (via threaded connections.). The metal pins of the SMA connectors 3 and 4 enter the top PCB layer and pass through the copper and the second PCB layer. Then this metal pin is soldered to the copper layer at the bottom of the second PCB layer. Figure 10 shows the measured S-parameters of the prototype, which are in good agreement with the previously presented simulated results. These acceptable results from two different solutions underscore the reliability of the proposed design. Figure 11 shows a photograph of the measurement setup with the help of a facilitated vector network analyzer (VNA) and high-frequency cables. A short, open, match load, through (SOLT) technique with mechanical kits was employed to calibrate the system for the desired frequency to achieve precise scattering parameters. In this step, a short (a piece of coaxial cable with a short circuit at the end) is connected to the VNA and performed a short calibration. Then, an open (a piece of coaxial cable with an open circuit at the end) is connected to the VNA and performed an open calibration. Finally, a load (a piece of coaxial cable with a matched impedance at the end) is connected to the VNA and performed a load calibration. In addition to the open, short, and load standards, through calibration has been used to improve accuracy.

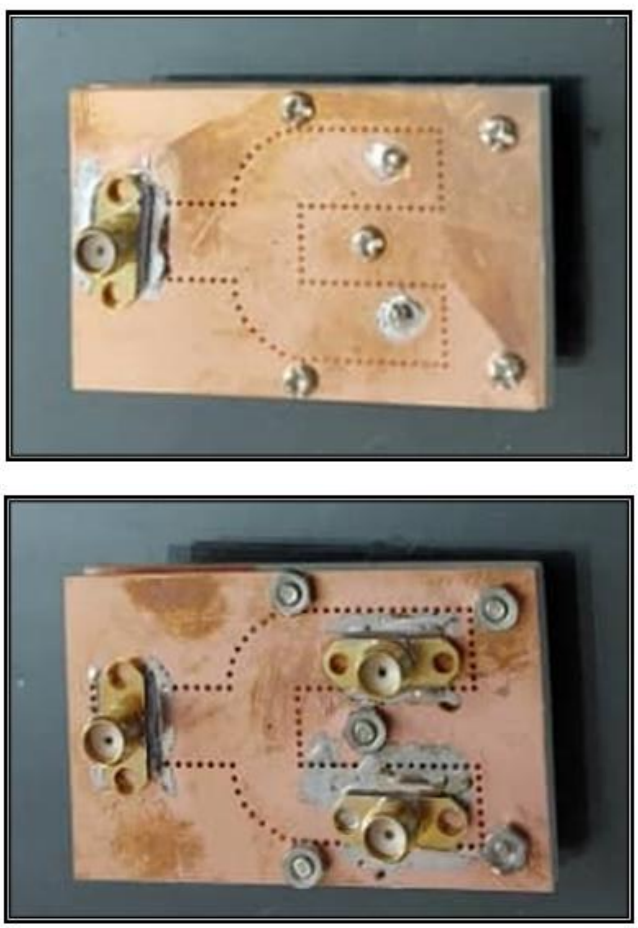

Figure 9. Photograph of fabricated diplexer-power divider prototype.

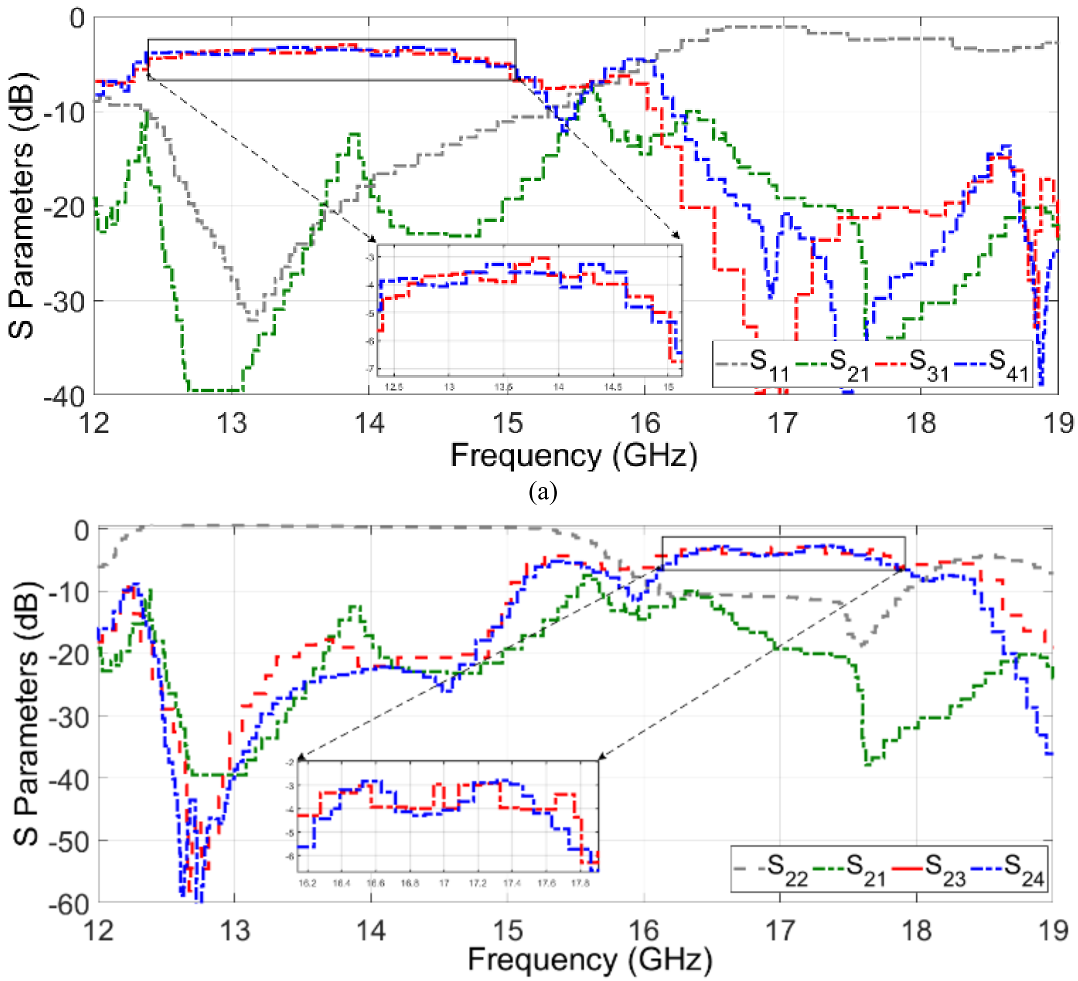

Figure 10. Measured S-parameters for the proposed diplexer-power divider. (a) Port 1 is excited. (b) Port 2 is excited.

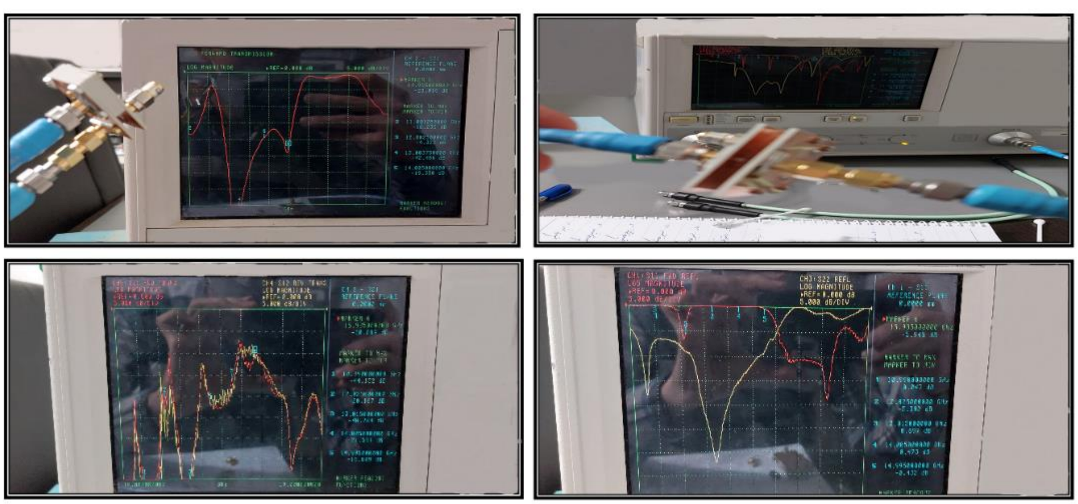

Figure 11. Photograph of measurement setup.

A comparison between various characteristics of the proposed design and previously reported results in terms of operation frequency, fractional bandwidth, insertion losses, and return losses is provided in Table 1. Several techniques have been reported in the literature to design diplexing power dividers [135], [136]. Even though these techniques result in good performance, their bandwidth is still limited. The implementation of some of these topologies requires several band-pass filters, increasing the complexity of the design.

Table 1**.** A comparison of some similar works in literature with the proposed results

Ref.	Center Frequency (GHz)	Fractional Bandwidth (%)	Insertion Losses (dB)	Return Losses (dB)	Isolation (dB)	Structure Technology
[150]	28.2 / 29.2	> 2.3 / > 2.2	0.9 / 0.9	13 / 13	55	Waveguide
[135]	73.5 / 83.5	> 6.8 / > 6	Not Given	13 / 13	50	Waveguide
[136]	2.45 / 2.98	< 10 / < 10	1.6 / 1.9	19.2 / 15.3	24	Microstrip
This Work	14.4 / 17.4	19.4 / 9.2	1.5 / 1.5	10 / 10	15-40	SIW

5.1.5 *Conclusion:*

A new technique for integrating diplexers and power dividers was proposed and validated experimentally at Ku-frequency with the aim of application in space communication. For space exploration and deep space probe observation, precise multiband and multifunction communication devices are required. The proposed device is based on extended connectors, via transitions, substrate integrated waveguides and stacked printed circuit boards that make it a modular device. Two different frequency spans of 13- 15.8 GHz and 16.6-18.2 GHz are envisioned with this technique covering Ku-band applications. The achieved insertion loss for the power divider was less than 1.5 dB. This compact structure with diplexing power dividing features was designed, fabricated, and tested in various solutions.

5.2 *Directive Millimeter-Wave End-Fire Diplexing Antenna for IoT Applications*

Authors: Farzad Karami, Halim Boutayeb, and Larbi Talbi1

[132]: IEEE Internet of Things Journal, Impact factor: 10.6

5.2.1 *Abstract:*

Millions of passengers use HSTs daily, in the world. The roofs of HSTs can be equipped with a variety of transmitting and receiving antennas to accommodate high-data-rate Internet services with reliable radio access for passengers. The design of commercial antenna systems is a compromise between cost, size, manufacturability, and performance. This paper proposes a new, compact and low-cost two-port millimeter-wave diplexing directive end-fire antenna, which is designed, fabricated and tested. The proposed antenna is made of a tapered slot antenna and a diplexing structure based on transitions in PCBs. The ports of the antenna cover the frequency band 25.9-32.4 GHz (6.5 GHz) and 34.6-37.1 GHz (2.5 GHz). In all operating frequency bands, measured isolation between input ports exceeds 24 dB. Furthermore, symmetric directive end-fire radiation patterns are obtained experimentally, with low side lobe level and low front-to-back ratio. All these features make the proposed diplexing antenna suitable for high-speed railway wireless networks.

5.2.2 Design Procedure:

5.2.2.1 Specifications and Requirements:

Nowadays, the footprints of wireless sensors and the IoT devices can be seen in all emerging technologies such as driverless cars, smart homes, drones, unmanned aerial vehicles (UAVs), healthcare smart sensors, advanced transportation systems, logistics control, and location tracking [137-139]. The main challenge of this research was to design an mm-wave transceiver antenna with features of low profile, wide operating bandwidth, dual isolated channel, and high-end-fire gain for mounting on an HST rooftop. The scenario of the railway communications systems is shown in figure 12. As bringing in this scenario, the HST wireless control systems are connected to the base station antennas located on the railroad track. In these systems, low-profile transmitting and receiving antennas are demanded to be installed on the train roof. Moreover, the radiation pattern direction of this antenna should be along with the railway track.

Traditionally, the transceiver devices would only transmit or receive on one channel. However, with the development of 5G and beyond 5G technology, the use of carrier aggregation has been proposed. In carrier aggregation, the device can transmit or receive on several channels simultaneously for an increased data rate. The used channels can exist within the same frequency band (intra-band carrier aggregation) or in separate bands (inter-band carrier aggregation) [140]. The proposed architecture operates at two isolated frequency bands as a transceiver antenna.

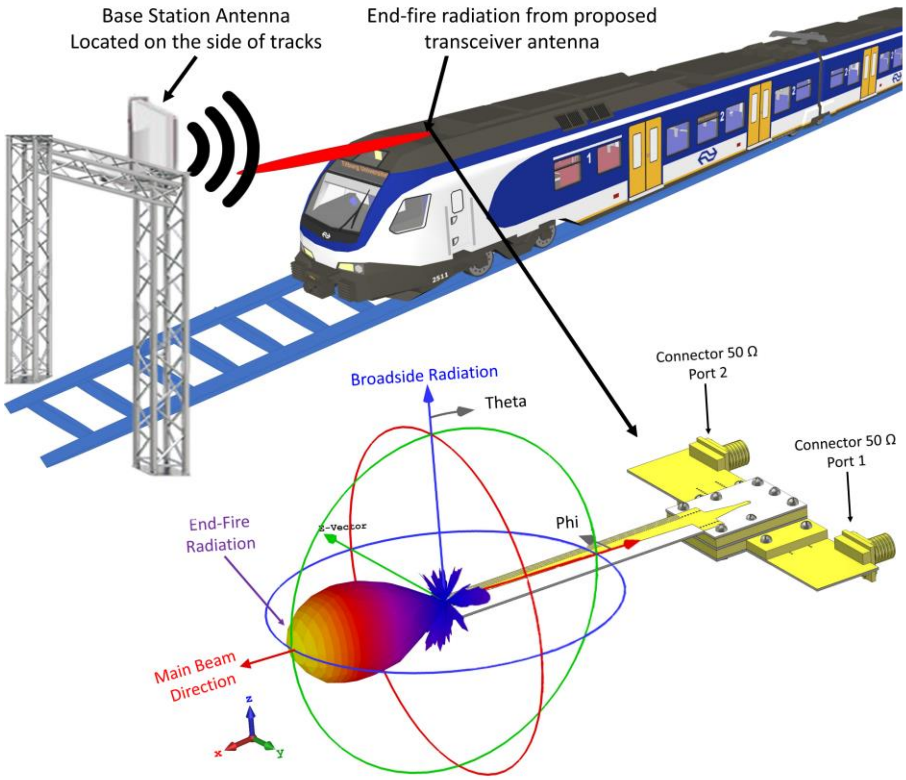

Figure 12. Illustration of the proposed end-fire transceiver antenna in the HST communications systems.

5.2.2.2 Proposed Feeding Network:

An initial architecture as a starting point for the design of the proposed substrate integrated waveguide (SIW)-based feeding network has been drawn out in Fig. 13(a). As shown in Fig. 13(a), the initial sketch of the proposed EM signal distribution network is composed of two stacked back-to-back SIW channels. Both channels are designed on Ro6002 PCB laminates (ε_r = 2.94 and tanδ = 0.0012). Both PCB laminates have the same thickness of 0.508 mm.

SIW technology has gained considerable attention in recent years due to its good performance, low fabrication cost, low losses, and ease of integration with other circuits. SIW structures are easily fabricated by PCB technology [141]. Also, SIWs have low radiation loss and hence they are the best alternative choice for metallic RWG in micro-wave and mm-wave applications. In the SIW channel design process, several primary geometries are selected as follows.

A SIW channel consists of a dielectric substrate, metalized on both faces, and two rows of metallic cylinder holes (vias) that are defined instead of the sidewalls of the RWG. A SIW channel can handle modes that practically coincide with a subset of the guided modes of the RWG, namely with the TE_{n0} modes, with n = 1, 2, …. The fundamental mode of a SIW channel is resembling the first mode (TE_{10}) of an RWG. The dominant mode of RWG is where the cut-off frequency (f_c) is.

The cut-off frequency of the RWG can be calculated using the following formula [142].

$$f_c = \frac{1}{2\pi\sqrt{\mu\varepsilon}} \sqrt{(\frac{m}{\pi a})^2 + (\frac{n}{\pi b})^2}$$

Where c is the speed of the light inside the RWG, a is the width, b is the height of the RWG, and m and n are the numbers that define the mode of propagation. In the dominant mode, TE_{10} (m=1, n=0) electric current density is vertical on the side walls. Due to the similarity between SIW and rectangular waveguide with the same propagation characteristics, the following empirical relationships are established between the geometrical dimensions of the SIW and the width of the rectangular waveguide [143].

$$W_{SIW} = a + 1.08\,\frac{d^2}{s} - \frac{d^2}{w}$$

where d (=0.4) is the diameter of SIW vias, S (=0.8) is the center-to-center distance of the two adjacent vias. To avoid the EM signal leakage, the diameters of the metallic vias, which form the SIW channels, should be appropriately selected, and the following two conditions are enforced;

$$\frac{S}{d} \leq 2 \text{, and } \frac{d}{\lambda_0} \leq 0.1$$

Where λ_0 is the free-space wavelength at the center frequency. Within the architecture shown in figure 13, a vertical coupling mechanism has been implemented between two stacked SIW channels. In this coupling mechanism, EM signal is transferred from the input ports toward the output. Figure 13(d) illustrates the proposed transition's inside dimensions from a cutting view perspective. As shown in this figure, the vertical transition includes two annular slots (named ring slots 1 and 2) surrounding a metal pin with a diameter of 0.6 mm. The diameter of ring slots 1 and 2 are 1.524 and 1.2 mm, respectively.

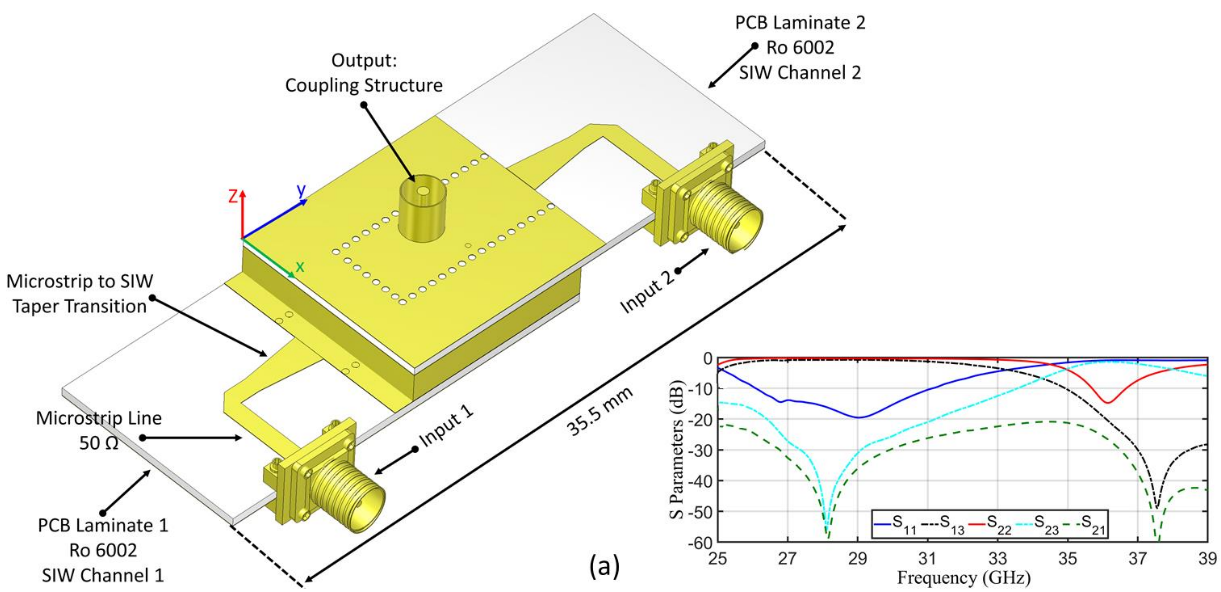

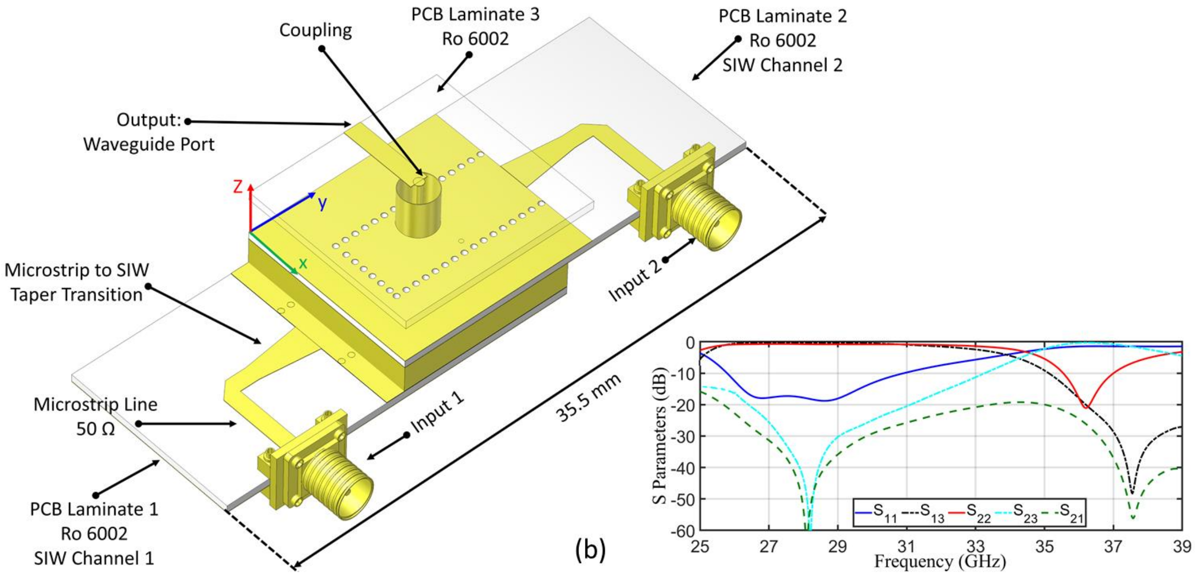
Coupling
PCB Laminate 3
Ro 6002
PCB Laminate 2
Ro 6002
SIW Channel 2
Output:
Waveguide Port
Microstrip to SIW
Taper Transition
Input 2
Microstrip Line
50 Ω
Input 1
35.5 mm
PCB Laminate 1
Ro 6002
SIW Channel 1
S Parameters (dB)
Frequency (GHz)
S_{11} S_{13} S_{22} S_{23} S_{21}

(b)

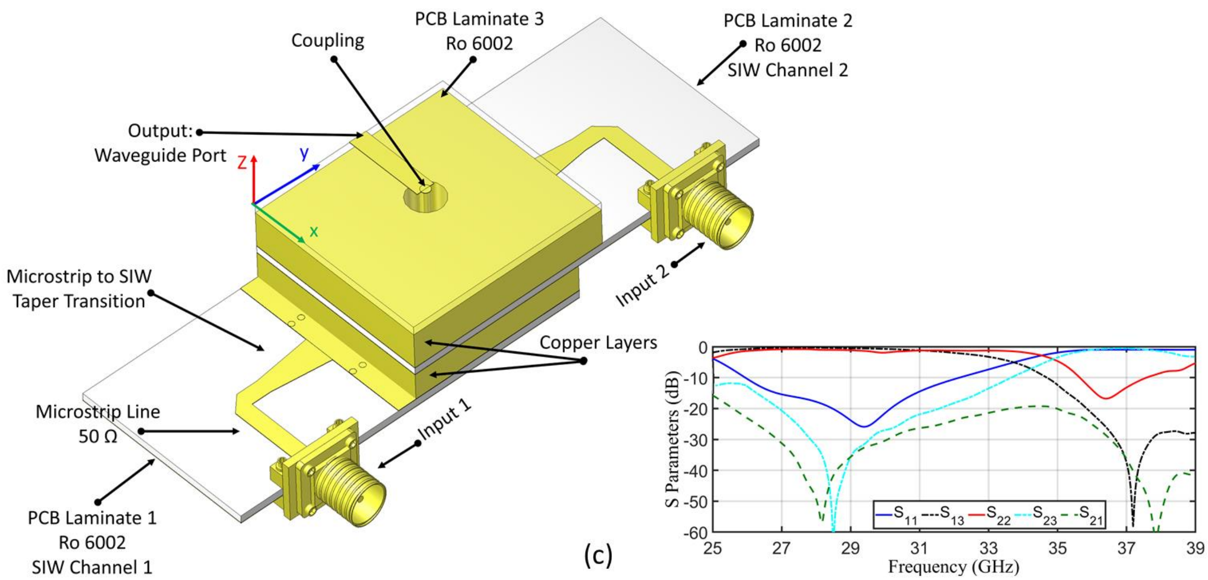
Coupling
PCB Laminate 3
Ro 6002
PCB Laminate 2
Ro 6002
SIW Channel 2
Output:
Waveguide Port
Microstrip to SIW
Taper Transition
Input 2
Copper Layers
Microstrip Line
50 Ω
Input 1
PCB Laminate 1
Ro 6002
SIW Channel 1
S Parameters (dB)
Frequency (GHz)
S_{11} S_{13} S_{22} S_{23} S_{21}

(c)

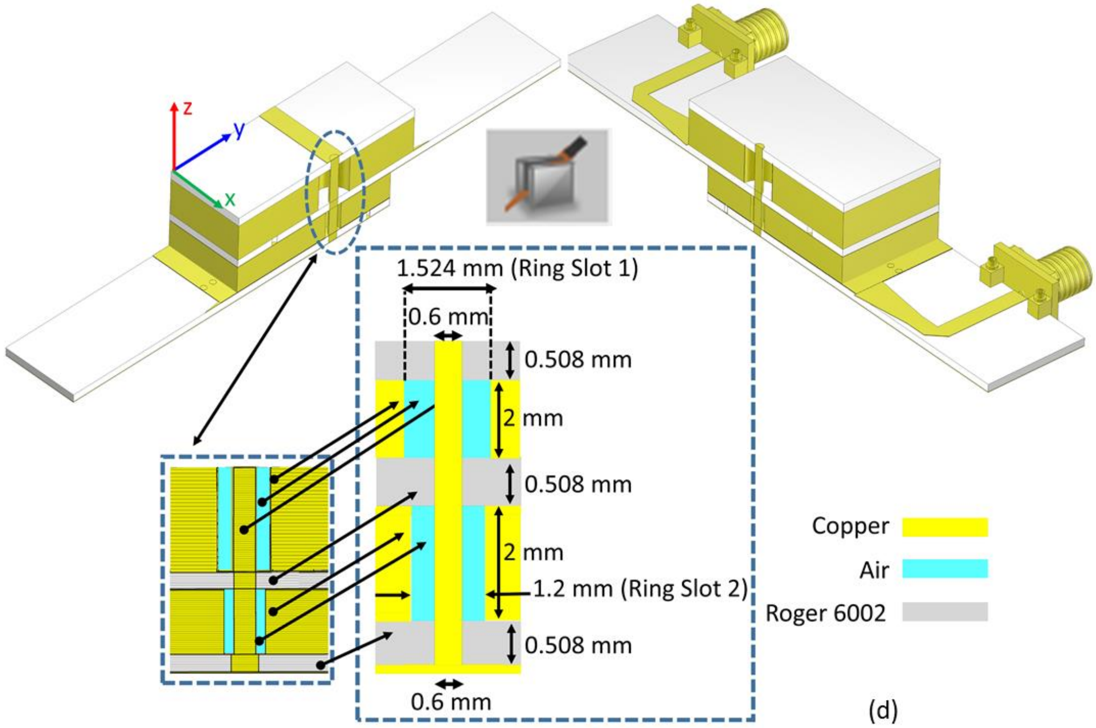

Figure 13. Architecture of the proposed feeding network. (a) Initial design, (b) Second design. (c) Third design. (d) The cutting view.

5.2.2.3 Coupling Mechanism and Performance:

In figure 13(a), the end sector of the vertical transition is labeled "Output". The Output includes a metallic pin surrounded by ring slot 1. This vertical coupling can be modeled by an L-shaped LC network. In this network, the metallic pin and the ring slots have inductance and capacitive reactance features, respectively. The value of these parameters can be controlled by changing the diameter of the vertical coupling mechanism. Mathematically, it is challenging and complicated to calculate these parameters. The optimal values of the proposed vertical transition are achieved using the full-wave simulation CST software. The simulated S-parameters of the initial design of the EM signal distribution network can be seen on the right side of Fig. 13(a).

Figure 13(b) illustrates the second architecture of the proposed distribution network. In this scheme, upon ring slot 1, a microstrip line is placed. The microstrip line was printed on a Ro6002 PCB laminate with a thickness of 0.508 mm. From Fig. 13(b), it can be observed that the end of the metallic pin is soldered to the edge of the microstrip line. Ring slot 1 and accompanied pin underneath this PCB laminate excites the microstrip line like a probe. The right side of Fig. 13(b) shows the simulated S-parameters of the second design. Figure 13(c) shows the final architecture of the proposed EM signal distribution network. In the last design, three 6002 PCB laminates are stacked from top to bottom, all with a thickness of 0.508 mm. Figure 13(c) shows two copper layers sandwiched between three PCB laminates. In this design, ring slots 1 and 2 of vertical coupling transition were realized using these copper layers. The thickness of each copper layer is

2 mm. In the manufacturing process, the copper layers were cut by a water jet machine, then two holes were created by a drill on them as ring slots 1 and 2.

In Figure 14, the top view of each layer of the last architecture is shown in detail. In the rest of the paper, the dimensions are all expressed in millimeters. Simulated S-parameters indicate that the proposed EM signal distribution network operates on two separate channels. The first channel covers a frequency spectrum from 25.7-32.2 GHz, whereas, channel 2 supports a frequency range between 34.8-37.4 GHz. The maximum insertion loss (S_{23} and S_{13}) is 1.1 dB in the whole operating for both channels. The isolation between the two channels seems to be larger than 20 dB.

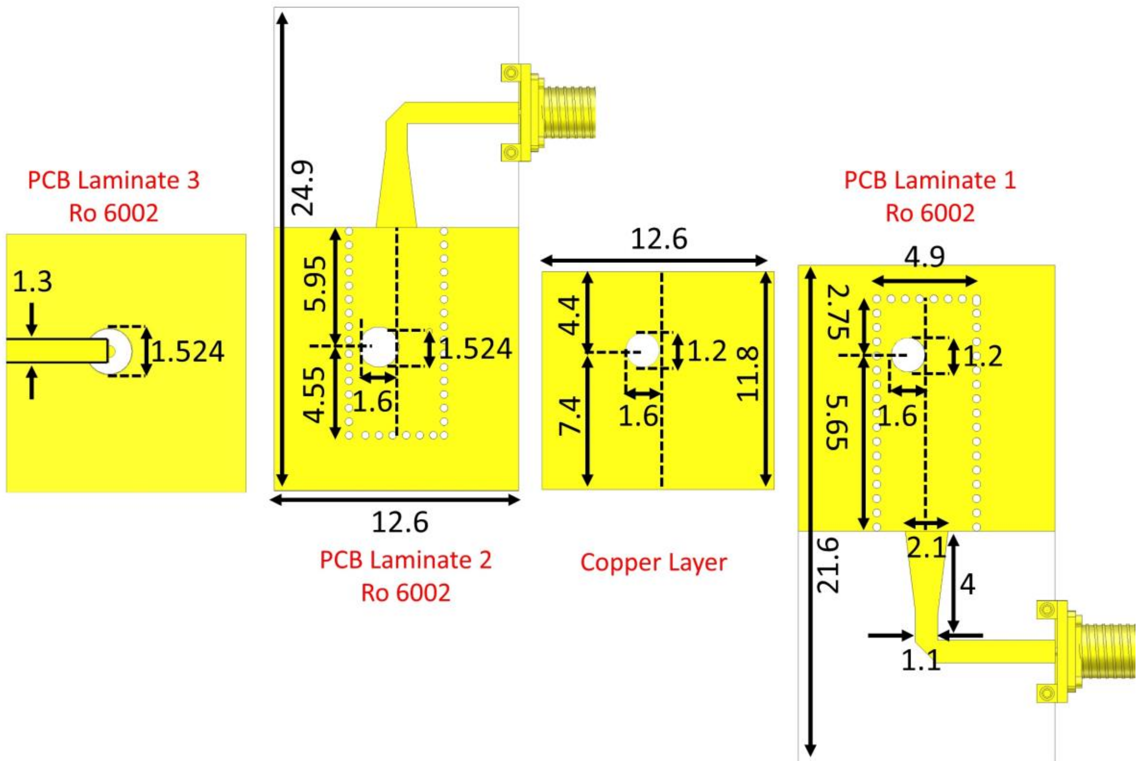

Figure 14. Top view of each layer of the proposed feeding network (Third design).

The proposed EM signal distribution network allows for more flexibility in the two isolated frequency spectrums while meeting the low-profile, low-cost structure. It can be integrated with different types of a planar broadside or end-fire antennas.

5.2.2.4 Design Procedure of the End-fire Antenna:

Figure 15 shows the configuration and dimensions of a SIW-based tapered slot antenna with a microstrip-to-SIW tapered transition. The tapered slot antenna is one of the most popular broadband antennas due to its simplicity, ease of fabrication, end-fire radiation pattern, high gain, and low fabrication cost. In this type of antenna, the configuration of the slot tapering may take various shapes, such as exponentially or linearly tapered form, constant-width form, and broken linearly tapered slot. The design guidelines of these antennas are expressed here.

Based on [144], the opening width of the tapered slot is equal to or larger than $\frac{\lambda_0}{2}$. Also, the effective thickness of the slot opening width is:

$$0.005 < \frac{t_{eff}}{\lambda_0} < 0.03, \text{ and } t_{eff} = (\sqrt{\varepsilon_r} - 1) \times h$$

Where h (=0.508 mm) is the dielectric thickness and ε_r (= 2.94) is the dielectric permittivity. Moreover, the antenna length can be chosen between $3\lambda_0$ and $8\lambda_0$.

Figure 15 illustrates a tapered slot antenna with corrugated shapes printed on its top and bottom. According to [145-146], corrugations have a beneficial effect on reflection coefficients, gain, and cross-polarization levels as well.

Different types of transitions can be used to excite the SIW feeding network of a taper slot antenna such as tapered, multilayer microstrip line, strip line, and grounded coplanar waveguide. The proposed tapered slot antenna is fed by a microstrip-to-SIW tapered transition. This transition could effectively provide a broad impedance matching.

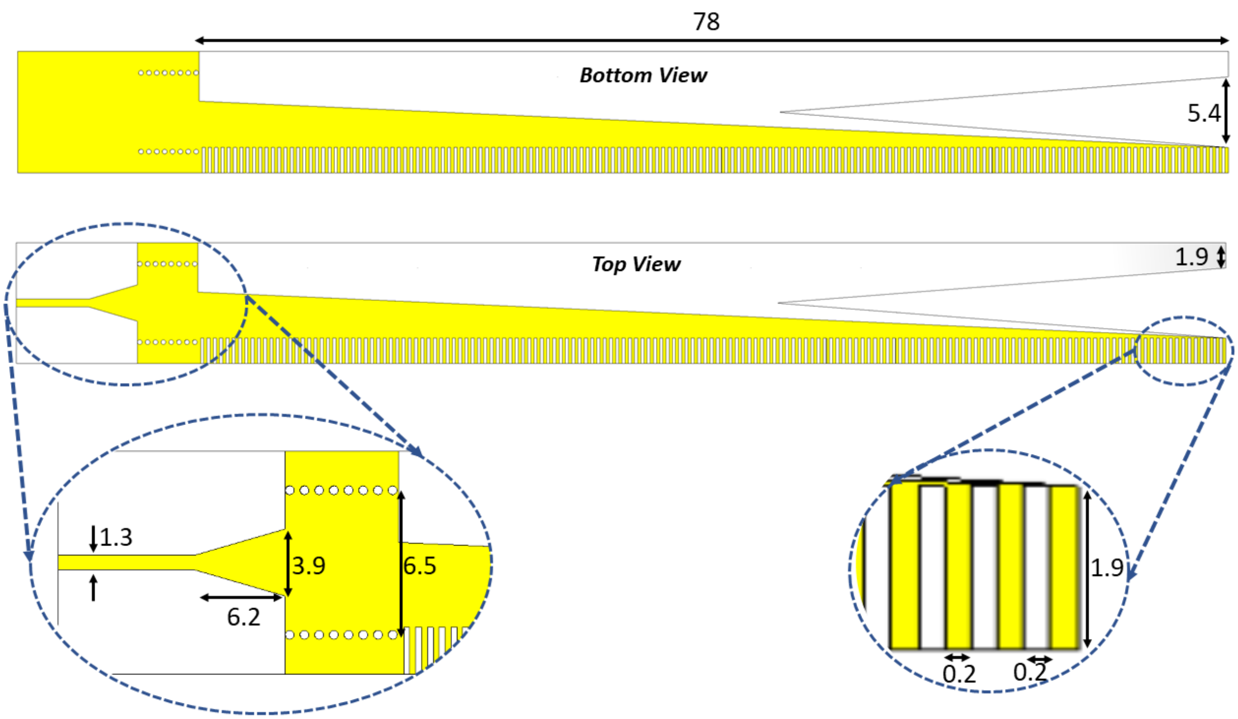

Figure 15. Configuration of the proposed tapered slot antenna printed on a Ro 6002 dielectric.

The simulated return loss and the realized gain of the proposed tapered slot antenna are illustrated in figure 16. The simulated S-parameters of this antenna for S11<-10 dB cover a frequency spectrum from 25-39 GHz. Based on the simulation results, the antenna's gain is almost stable between 13-15 dBi throughout the whole operating bandwidth. The gain of tapered slot antennas is independent of the aperture size [147].

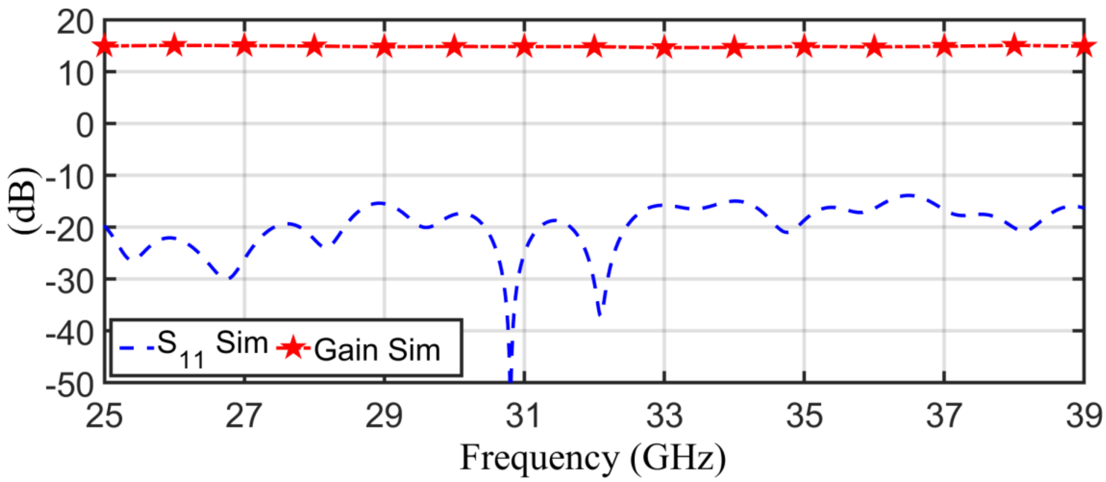

Figure 16. Simulated S_{11} and realized gain of the designed tapered slot antenna.

5.2.2.5 Dual-channel End-fire Transceiver Antenna Topology:

The different perspective views of the proposed dual-channel end-fire transceiver antenna system is illustrated in Fig. 17. This architecture consists of five stacked layers from top to bottom, which includes three Ro 6002 PCB laminate with a thickness of 0.508 mm, and two copper layers with a thickness of 2 mm. The proposed transceiver system is created after directly connecting the third design of the EM signal distribution network (Fig. 13(c)) to the proposed tapered slot antenna (Fig. 15). The proposed system forces its antenna to operate in two independent operating bandwidths.

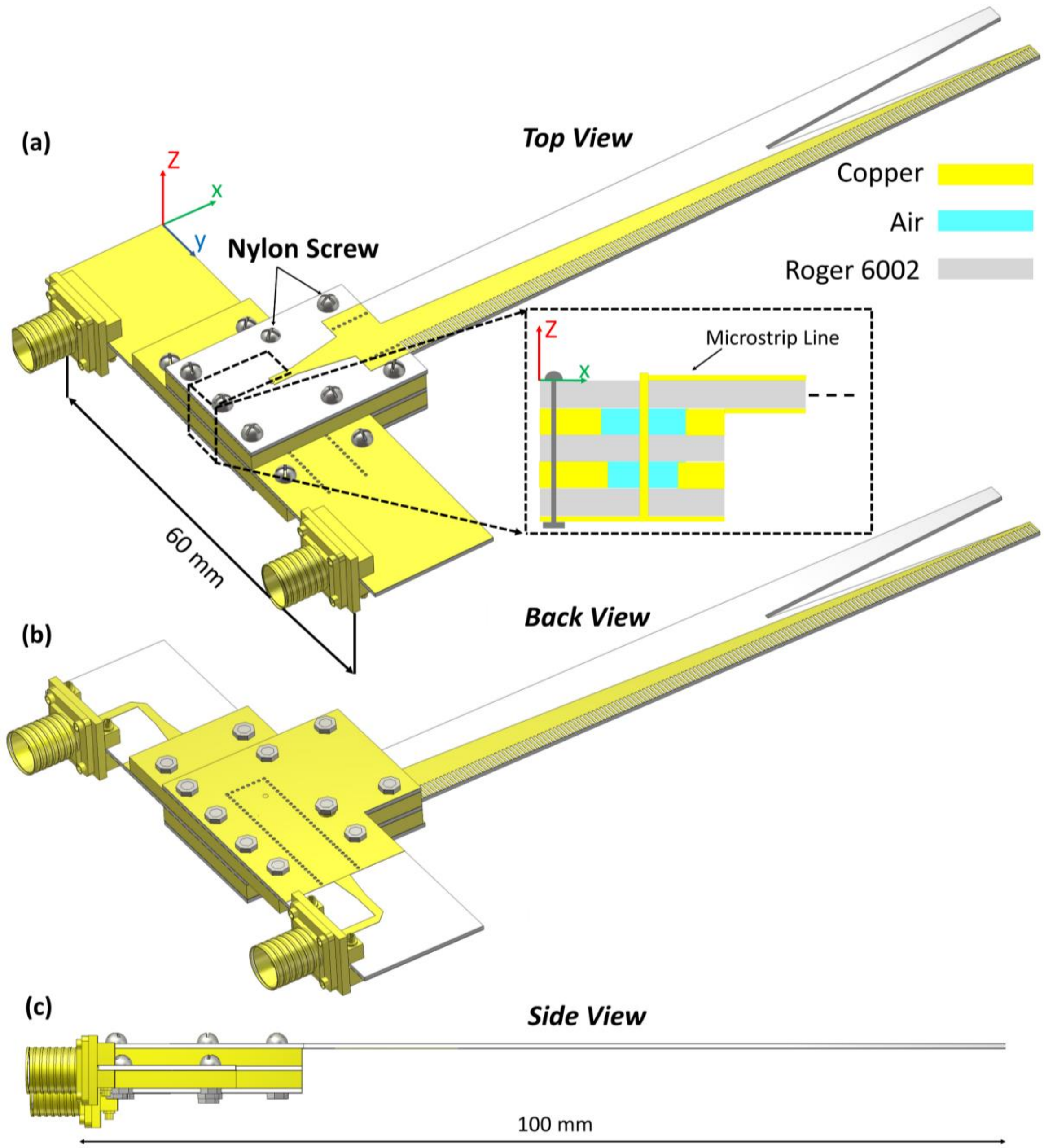

Figure 17. Configuration of the proposed dual-channel end-fire transceiver antenna. (a) Top view. (b) Back view. (c) Side view.

Figure 18 illustrates the distribution of electric fields for the proposed transceiver antenna system at 29 GHz (center frequency of channel 1) and 36 GHz (center frequency of channel 2). When input 1 is excited, the EM signal flows in SIW channel 1 at a frequency range from 25.7-32.1 GHz. After, the propagated EM signal is vertically transmitted toward the microstrip line through the vertical coupling mechanism. Once the EM signal reaches the microstrip line, the tapered slot antenna will be radiated.

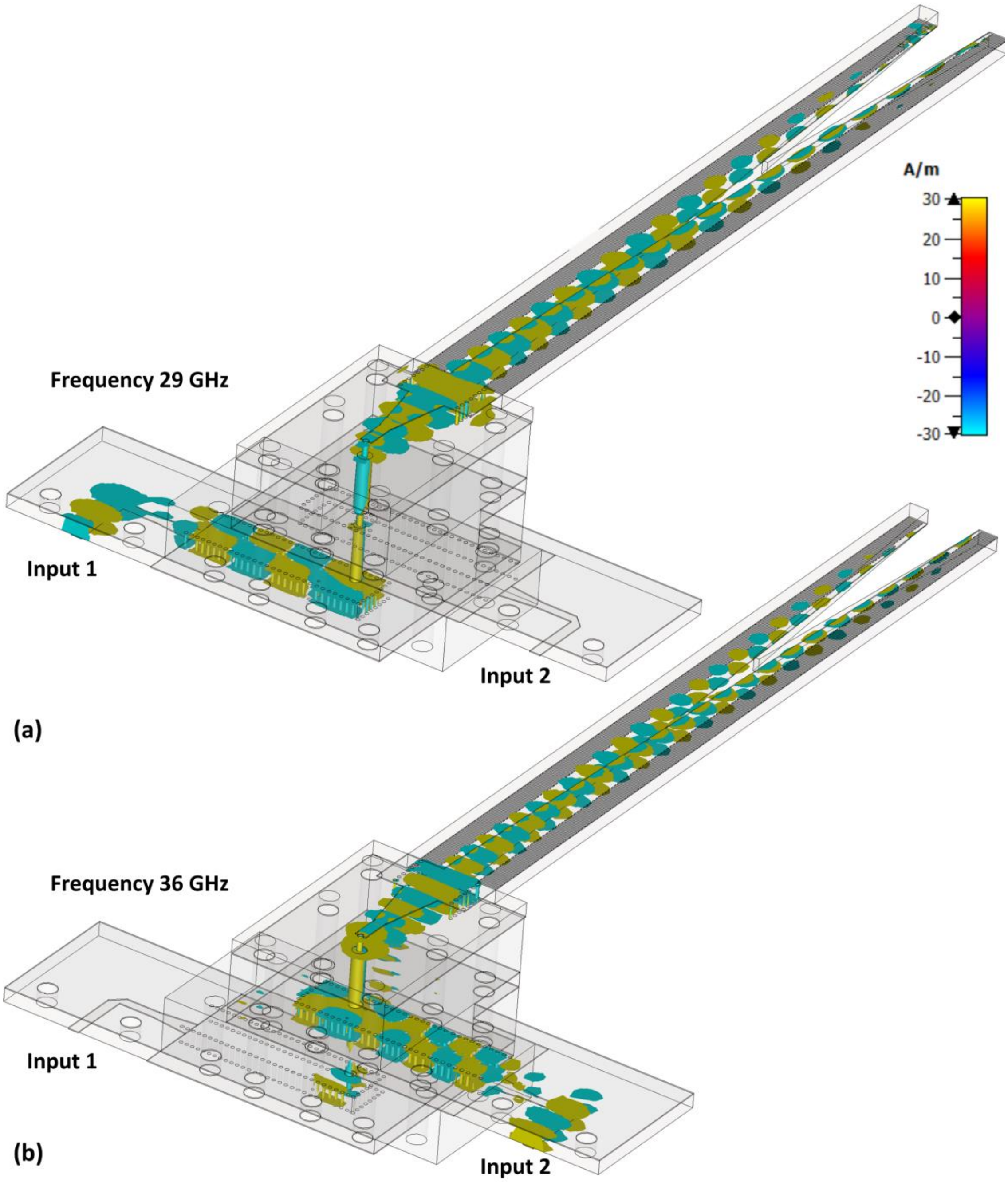

Figure 18. Simulated electric field distribution for proposed end-fire transceiver antenna (a) Exiting port 1 (frequency 29 GHz). (b) Exiting Port 2 (frequency 36 GHz).

Two standard RF connectors 2.92 mm were used for inputs 1 and 2. In the vertical coupling mechanism, after the excitation of input 1, no RF signal propagates into SIW channel 2. From Fig. 18(b) can be observed that when input 2 is excited, the EM energy propagates in the SIW channel 2. Then it enters the vertical coupling transition at the end of SIW channel 2. After it reaches the microstrip-to-SIW taper transition, the tapered slot antenna begins to radiate. For this configuration, due to the existence of isolation, no RF signals pass through SIW channel 1 when SIW channel 2 is activated.

Some simulated transceiver antenna properties are summarized in Fig. 19 to gain deep insight into the behaviour over two frequency ranges from 25-39 GHz, specifying the proposed antenna's operating frequency range in two separate channels. It is confirmed by the simulated scattering parameters of the proposed transceiver system that it operates at two different frequency channels, 25.7-32.1 GHz and 34.7-37.1 GHz. The useful bandwidth of channels 1 and 2 is 6.4 and 2.4 GHz, respectively. The isolation between two channels (S_{21}) is much more than 20 dB in the whole operating bandwidth. It can be observed from Fig. 19(b) that the simulated realized gain of the proposed transceiver system for both channels varies between 12.3-14.7 dBi.

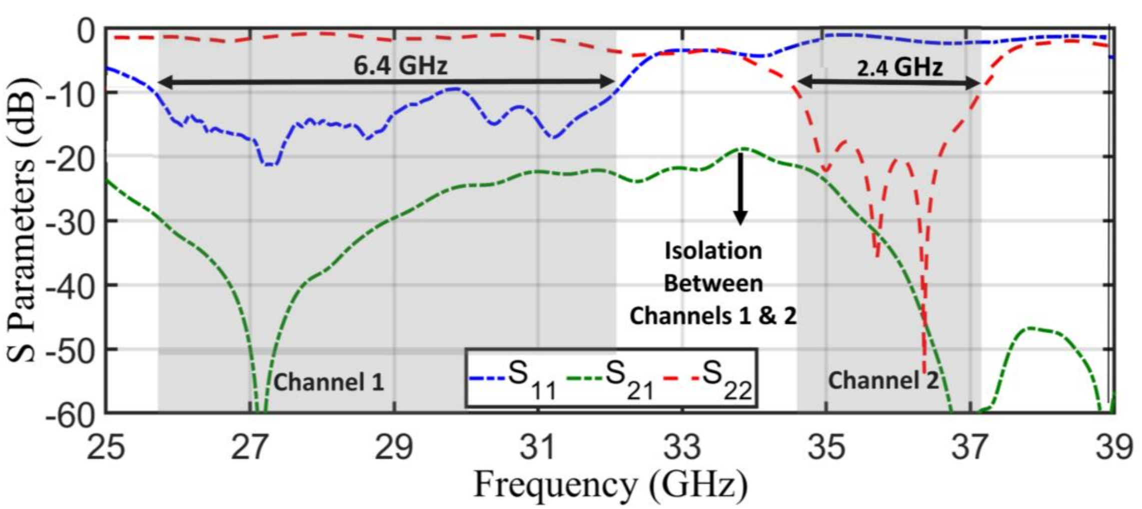

(a)

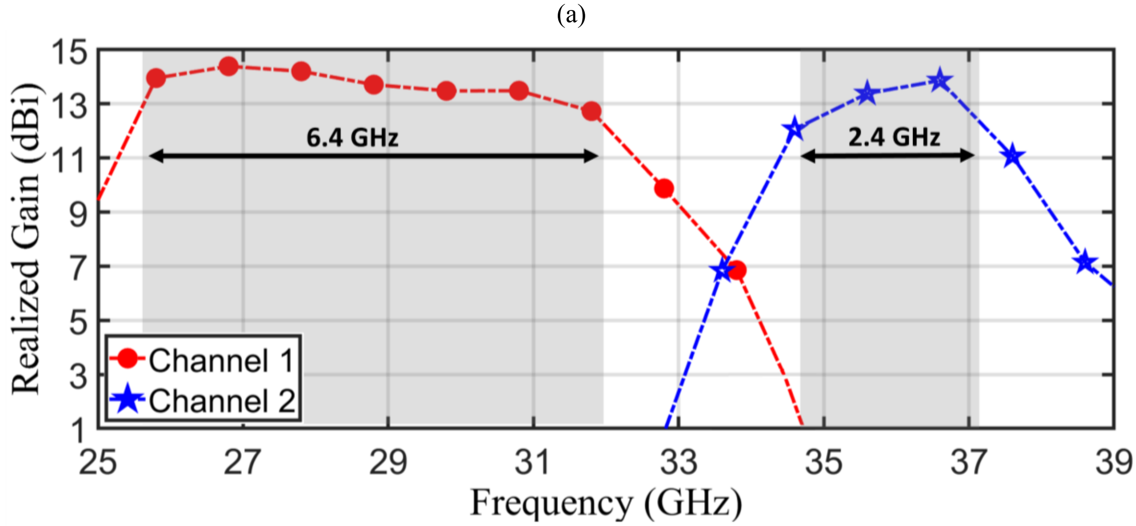

(b)

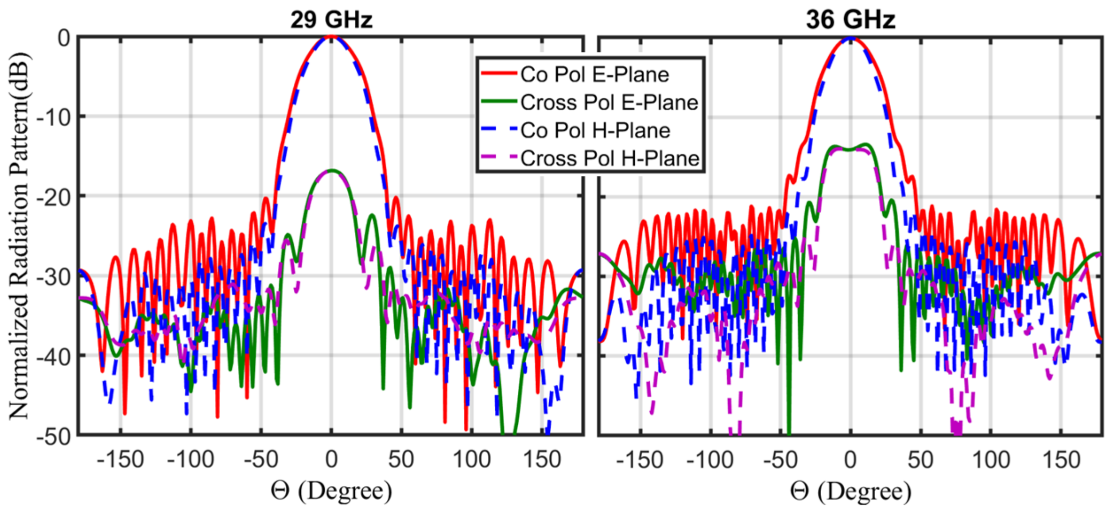

(c)

Figure 19. Simulated results of the proposed dual-channel end-fire transceiver antenna. (a) S-parameters. (b) Realized gain. (c) Radiation patterns at 29 GHz (center frequency of channel 1) and 36 GHz (center frequency of channel 2).

In Figure 19(c), the simulated normalized radiation patterns of the proposed end-fire transceiver antenna are shown at the centre frequency of channels 1 and 2. The simulated radiation patterns of the proposed transceiver antenna exhibit symmetrical unidirectional radiation patterns with a front-to-back ratio better than 30 dB. The sidelobe levels remain at the same good level as for 29 and 36 GHz and are smaller than 18 dB over both channels' entire bandwidth.

5.2.3 Experimental Results and Performance

5.2.3.1 Antenna Characteristics:

To validate the proposed concepts, a prototype of the end-fire transceiver antenna system is manufactured and measured. A photograph of the fabricated transceiver antenna system is illustrated in figure 20. Each layer of PCB laminates can be easily fabricated by a single-layered PCB technology and also copper layers can be made by a simple and accurate machined process. Afterward, all of the PCB laminates and copper sheets are stacked and fixed together with nylon screws.

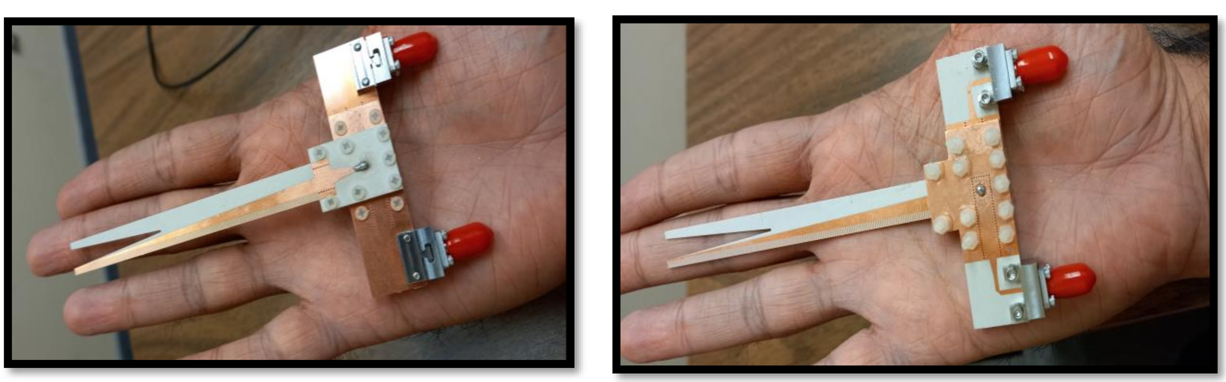

(a) (b)

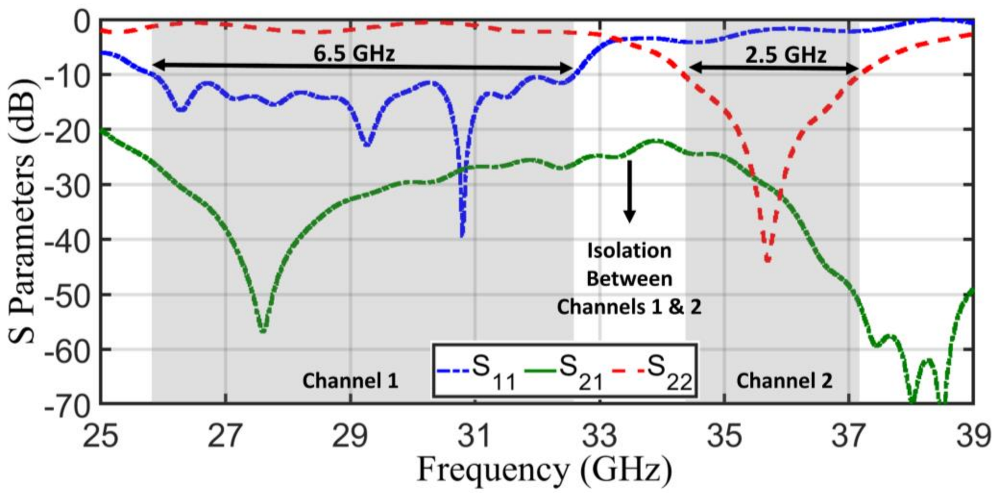

(c)

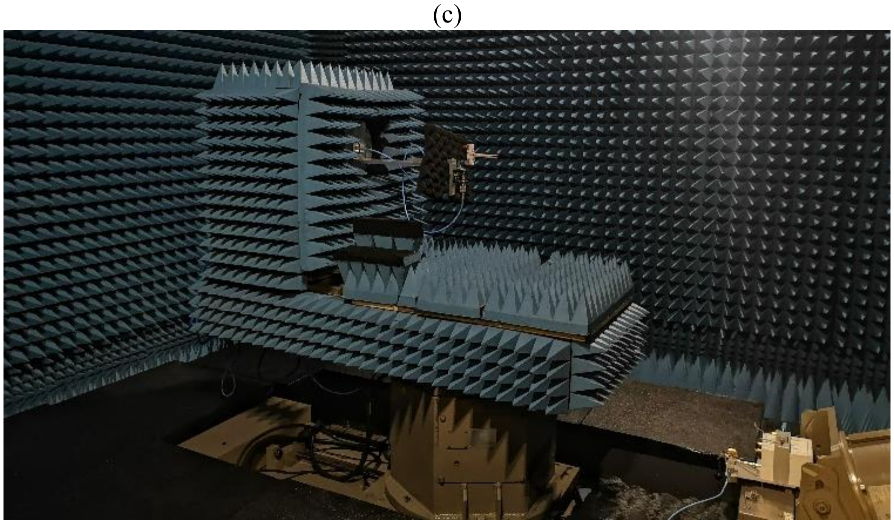

(d)

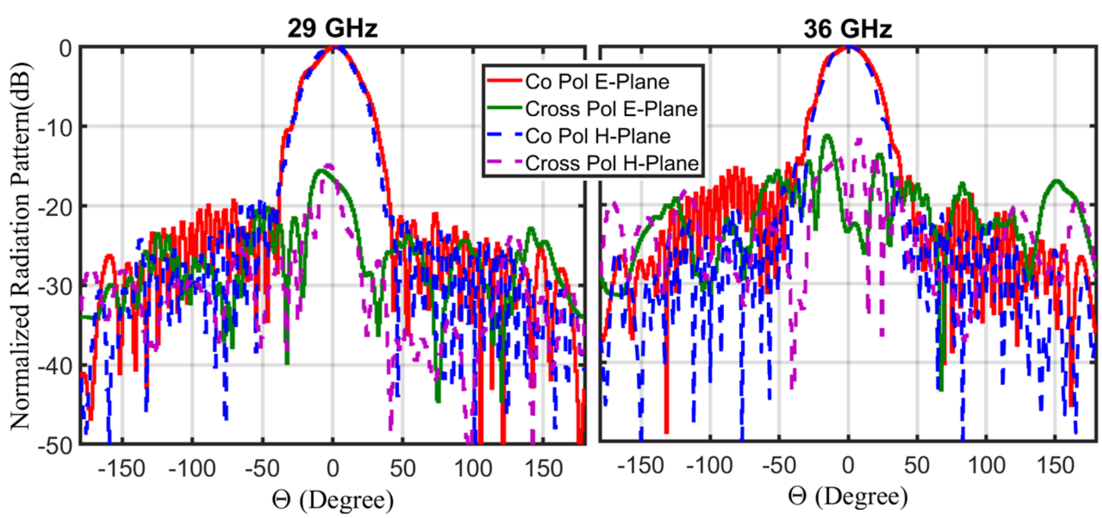

(e)

Figure 20. Configuration of the proposed Ka-band transceiver antenna: (a), (b) Photograph of the top and back views. (c) Measured scattering parameters. (d) Photograph of the antenna under test in the anechoic chamber. (e) Measured end-fire radiation patterns at frequencies 29 and 36 GHz.

The −10-dB impedance bandwidth was measured in the two frequency spectrums of 25.9-32.4 GHz (6.5 GHz) and 34.6-37.1 GHz (2.5 GHz). Moreover, the end-fire radiation pattern of the proposed transceiver system was measured and depicted at 29 and 36 GHz in an anechoic chamber. The transceiver antenna under test within the anechoic chamber can be seen in Fig. 20(d). The measured radiation patterns at frequencies of 29 and 36 GHz are shown in Fig. 20(e) for both cutting planes of $\phi = 0^\circ$ and $\phi = 90^\circ$. The main beam direction of the measured radiation beams is observed along the antenna direction. The measured side lobe levels were obtained also below 15 dB in the whole operating bandwidth.

5.2.3.2 Comparison and Discussion:

In recent years, railroad operators have launched innovative campaigns that are evolving the concept of "smart rail". With smart rail services, travellers are experiencing a variety of services, such as onboard video surveillance, train multimedia dissemination, the IoT for the railways, and autonomous driving. Accommodating these data-craving applications for the smart rail concept and high-speed railway scenarios is potentially challenging. Currently, HST communication networks such as, Mobile Communications for Railways (GSM-R) only support a 9.6 kbps maximum transmission rate, and the available bandwidth of the ongoing LTE-R is limited to 20 MHz [148]. To satisfy the increasing demands and provide high-data-rate services, broadband mm-wave communication networks are proposed for 5G HST wireless networks. This valuable frequency spectrum can provide a substantial increase in the capacity of HST wireless systems and offer a robust platform to support wireless services with over 100 Gbps data rates and low latency.

HST networks need to install transmitting and receiving antennas on their top roof to provide wireless services. Owing to the limitation of space for embedding antennas on HST top roofs, transmitting and receiving antennas should be placed close to each other. It reveals many technical problems and conflicts in transmitting and receiving performance. Transceiver antenna systems could be an appropriate option to use in HST networks to overcome the mentioned drawbacks. Table 2 compares the characteristics and performances of the proposed transceiver antenna system with those of other antennas from the literature.

Structures such as a single antenna with a diplexer or dual-band antennas could be used for HST applications. A system made of an antenna and a diplexer provides multi-service and multi-band communication platforms and it can significantly improve the performance of frequency-division duplexing communication links [149]. An antenna with a diplexer has been proposed in [150] for millimeter-wave frequency bands, but with the operating frequency bandwidth is relatively small. Furthermore, the diplexer is usually designed separately and then it is connected to the antenna. For this reason, the diplexer with the antenna occupied a large space in the system. Moreover, the size of the diplexer is often larger than the size of the antenna. Dual-band antennas with a single feeding port can be another option for HST transceivers. In [151], the authors propose a millimeter-wave fully additively dual-band slotted patch antenna. In transceiver applications, this antenna can use both frequencies individually or simultaneously, but complex and expensive equipment and systems are needed to achieve this purpose.

Table 2**.** a comparison between the proposed antenna and state-of-the-art.

Reference		[25]	[150]	[151]	This work
Technology		PCB	Gap Waveguide	PCB	PCB
Antenna Type		Patch	Slot Array	Patch	Tapered Slot
Size	Length	100	180		100
	Width	20	180	N.A.	35
	Thickness	N. A.	10		5.5
No. Band		Single-band	Dual-band	Dual-band	Dual-band
Frequency Bandwidth @Centre frequency (GHz)		1.3 @ 28	0.65 @ 28.21 and 0.65 @ 29.21	0.5 @ 28 and 0.8 @ 37.8	6.4 @ 28.9 and 2.4 @ 35.9
Peak Gain (dBi)		10.38	32	6.83	14.7
Radiation Pattern Type		End-fire	Broadside	Broadside	End-fire

The proposed diplexing antenna is compact, low-cost and present good performance in terms of impedance bandwidth and gain. It does not require complex and high-cost equipment, as opposed to dual-band antennas with a single port. The overall size of the proposed architecture is 100×35×5.5 mm3. It covers 9 GHz bandwidth for two different channels. Directive end-fire radiation patterns are obtained, with low sidelobe level and low front-to-back ratio. The proposed transceiver antenna exhibits a great aerodynamic condition compared with broadside antennas.

Another essential factor in raising the reliability of wireless communication systems is radiation efficiency. According to IEEE standards, antenna radiation efficiency is defined as: “The ratio of the total power radiated by an antenna to the net power accepted by the antenna from the connected transmitter’’ [152]. The radiation efficiency of the proposed transceiver antenna is larger than 80%

over the whole operating bandwidth. All mentioned features make the proposed antenna a good candidate for 5G HST applications.

5.2.4 Conclusion:

In this paper, a new compact and low-cost millimeter-wave diplexing end-fire antenna which is made of a tapered slot antenna and an integrated feeding network based on staked PCBs has been proposed. The first port of the antenna operates in the frequency range 25.9-32.4 GHz (6.5 GHz bandwidth), whereas the second port operates in the frequency range 34.6-37.1 GHz (2.5 GHz bandwidth). The measured isolation between the two ports are higher than 24 dB in all operating frequency bands. Good performances have been obtained in terms of gain, low front-to-back ratio, and low side lobe level. The proposed diplexing antenna is suitable for smart railway applications.

5.3 Multifunctional Switched-beam Antenna Located on Solar Cell for Vehicular to Satellite Communication

Authors: Farzad Karami, Halim Boutayeb, Larbi Talbi, Khelifa Hettak, and Alireza Ghayekhloo.

IEEE Transactions on Vehicular Technology, Impact factor: 6.8

5.3.1 Abstract:

In this section, a multifunctional beam forming architecture is studied in detail for intelligent transportation systems and advanced vehicular technologies. The proposed structure can radiate or receive multiple beams simultaneously. This system can significantly improve the scanning coverage and channel capacity based on a switched beam methodology. A solar panel layer is integrated with the designed architecture in order to provide a sustainable renewable energy source for the envisioned system. The proposed multifunctional antenna is oriented towards the space direction with sunlight energy harvesting capabilities and vehicular satellite communication ability, all at the same time. Furthermore, an automated antenna system based on the proposed multidisciplinary structure can be applied for highway-to-vehicle connections.

5.3.2 Geometry of the Proposed Multifunctional Architecture and Analysis of the Performance:

This part proposes a new multifunctional device that is integrated with solar panels for the new generation of vehicular and advanced transportation systems. The proposed architecture is composed of three layers: an antenna layer, a solar panel layer, and a BFN layer. The antenna section is printed on a PCB laminate and it is composed of symmetric 4 × 4 arrays of radiating patches combined with a series of high-impedance microstrip lines. The solar panel lies on the BFN layer. Two orthogonal BFNs are printed on a PCB laminate. This PCB laminate forms the third layer of the proposed structure. The electromagnetic signals transfer from BFN to the antenna layer through eight half cavities with a coupling mechanism. By mounting the proposed multifunctional system on top of vehicles, they can be linked to satellites and highway RFID tags. With this architecture, multiple radiation patterns with 2D scanning capability can be generated for a vehicle.

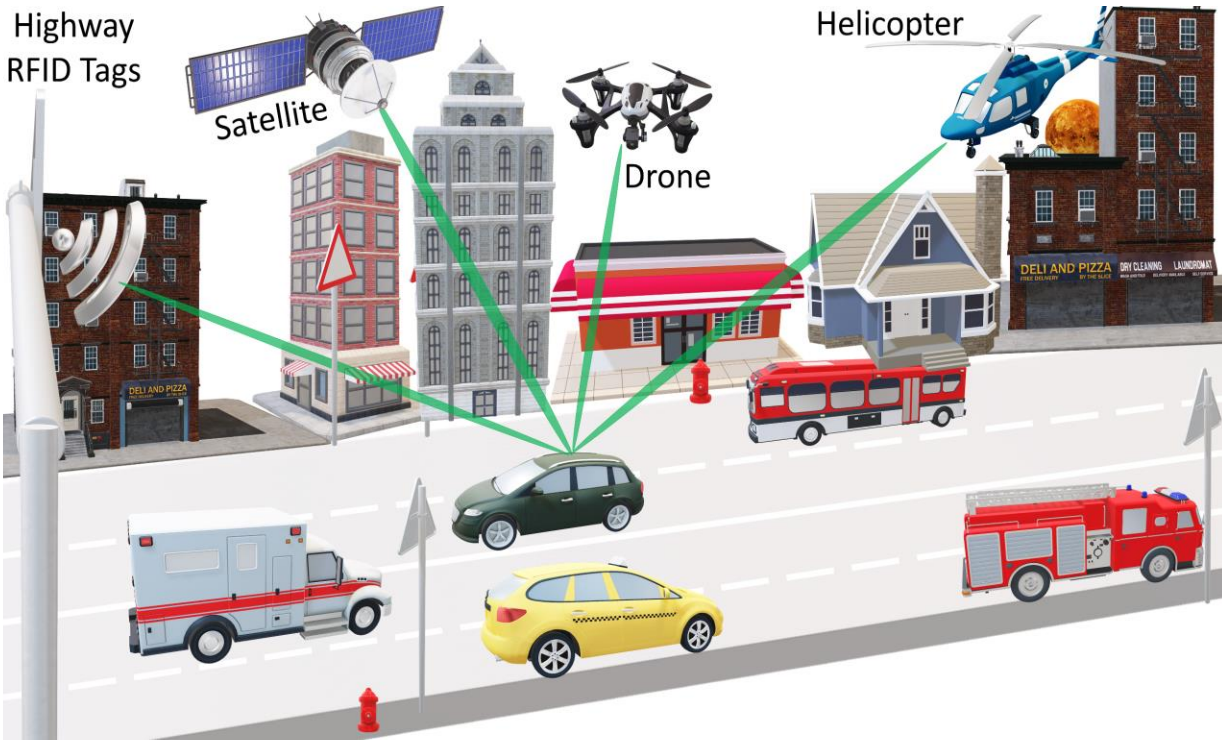

Figure 21. Schematic perspective of the multifunctional antenna device integrated with solar panel. Multiple 2D patterns in vehicular networks for improving connectivity are suggested such as satellite, drone, and highway communications with a vehicle.

5.3.2.1 Overview of the proposed system:

The proposed design consists of three stacked layers, as shown in Figure 22, including one PCB laminate as the antenna layer, one PCB laminate as the BFN layer, and a solar panel layer as an energy supplier. The radiator patches are etched on the upper layer, whereas the substrate integrated waveguide (SIW) BFN is printed on the lowest PCB laminate. On top of the BFN substrate, solar panels are pasted on a nonradiated surface.

5.3.2.2 Beamforming Network:

SIW technology has gained considerable attention in recent years due to its good performance, low cost, low losses, and ease of integration with other active and passive circuits [153-154]. In addition, SIW has many propagation characteristics similar to hollow rectangular waveguides. Therefore, the SIW has been an alternative for these heavy and costly structures as an attractive choice for microwave and mm-wave applications [155-156]. SIW technology can be used to design multi-beam systems such as Butler matrix. By using the Butler matrix, scanning capabilities, sufficient bandwidth, and beam-width can be achieved. The Butler matrix can efficiently increase scanning coverage and channel capacity. Components such as hybrid couplers, crossovers, and phase shifters are inseparable parts of Butler matrices. The arrangement of these components ensures the required phase difference and amplitude in output ports. As a result, the antenna array that is connected to the Butler matrix will be able to generate multiple beams in different directions.

Figure 23 shows a detailed block diagram of the proposed BFN. In this block diagram, the amplitude and phase of the proposed antenna array's inputs are controlled using two orthogonal Butler matrices with the same geometry. Each Butler matrix consists of two 90-degree couplers, two cross-overs, and four phase-shifters. It can be seen that each Butler matrix comprises four input channels and four output channels. When an EM signal enters one of the input channels, the other inputs are isolated. In theory, an exciting input channel will provide -6 dB of power to each output port, while adjacent output ports will have a uniform phase difference.

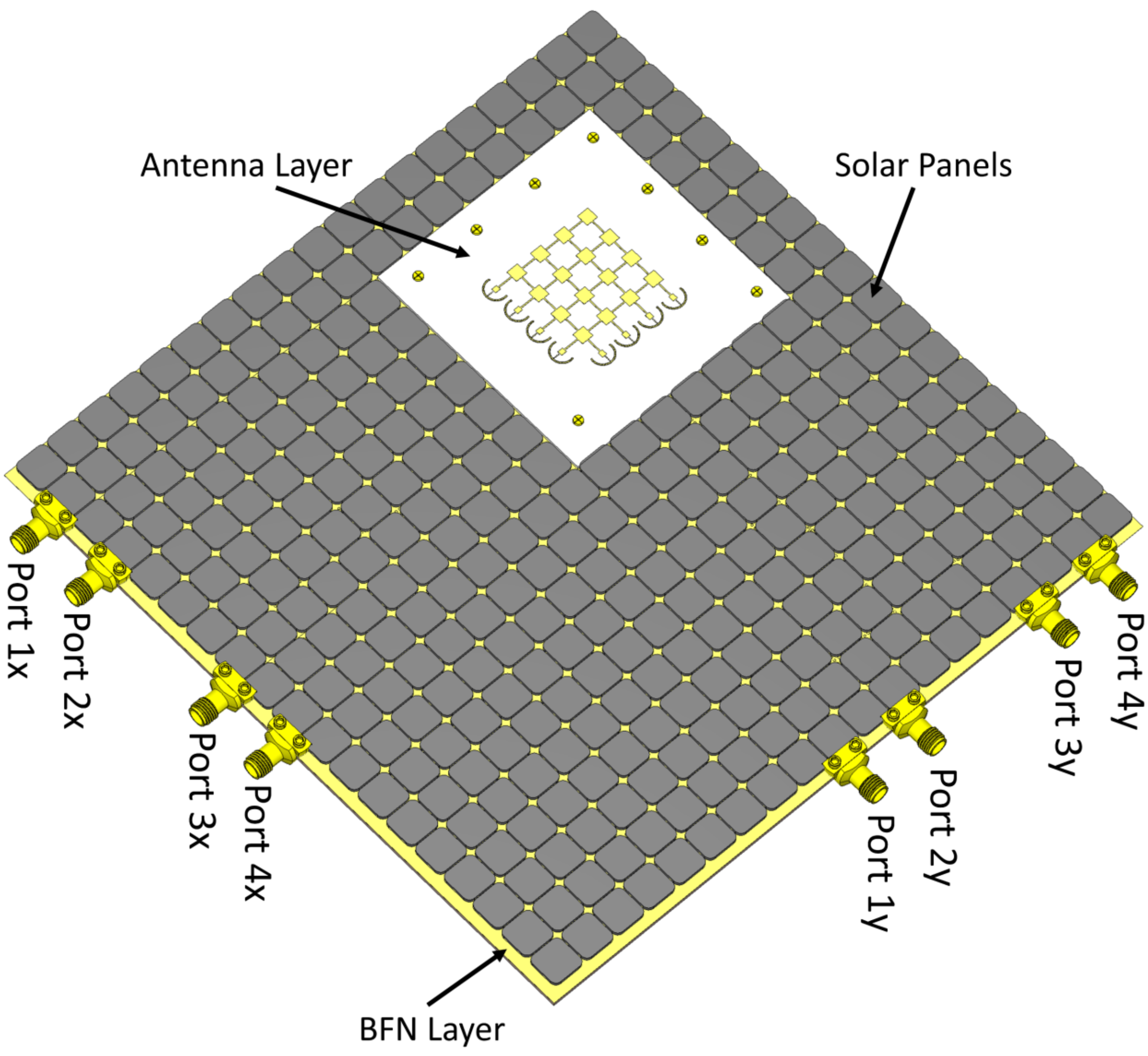

(a)

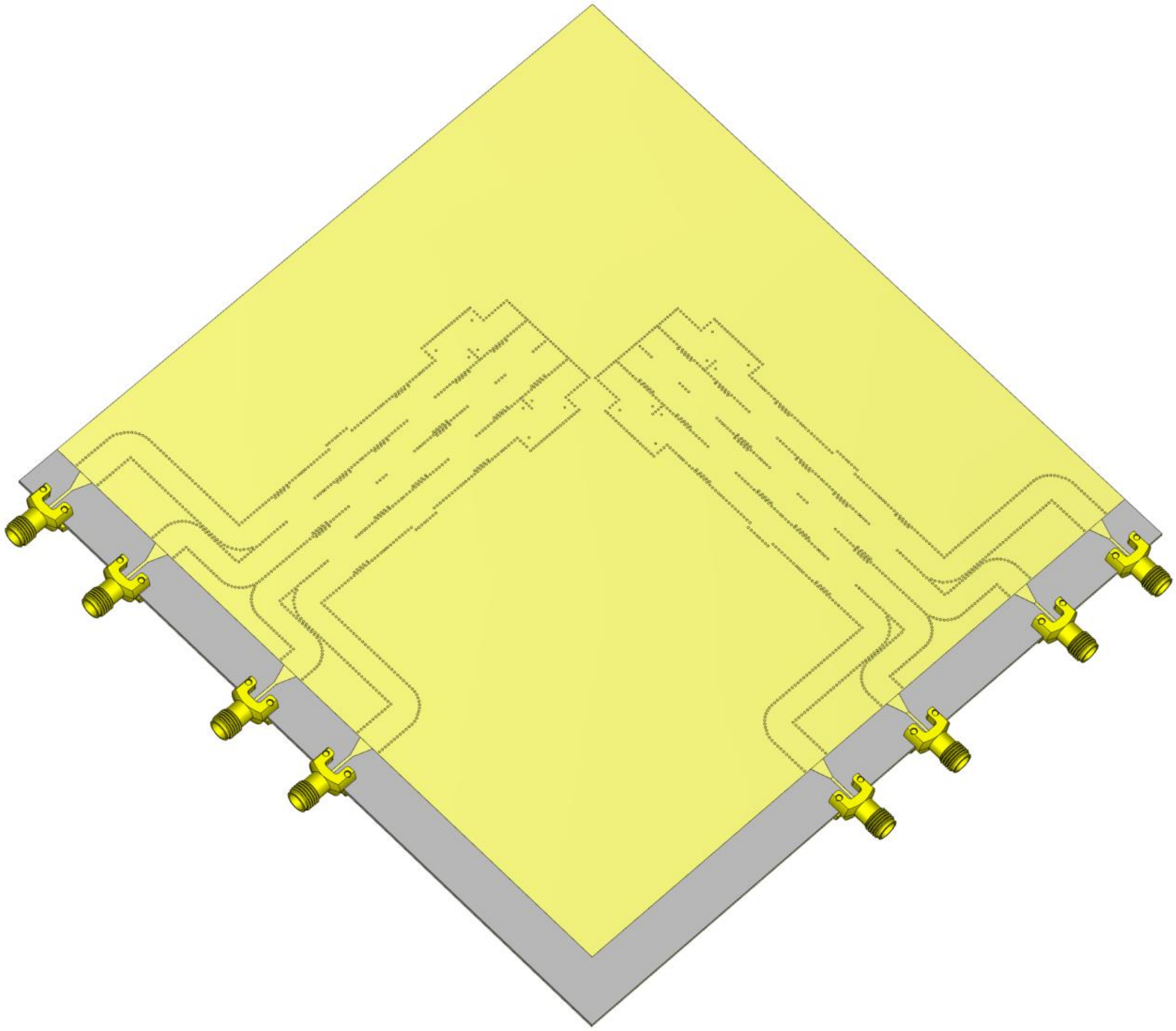

(b)
Figure 22. Overall configuration of the proposed multifunctional structure integrated with solar panels. (a) Top view, and (b) back view.

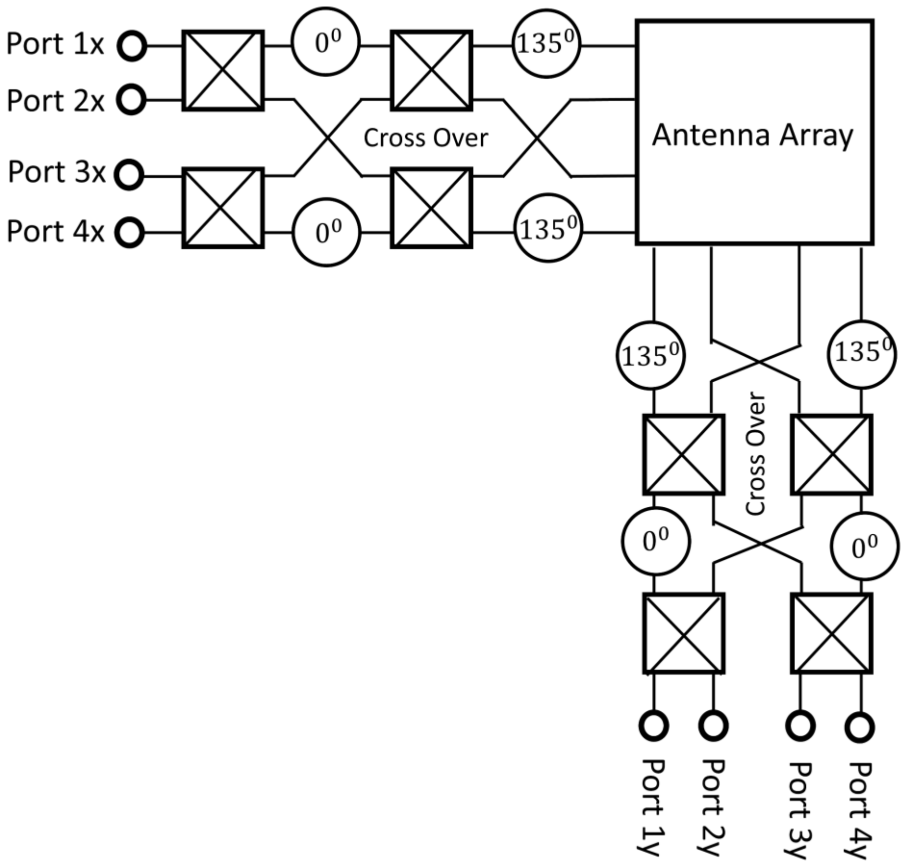

Figure 23. Block diagram of the proposed beamforming network (BFN).

B. 1) Hybrid Couplers and Crossovers:

In the topology of a Butler matrix, hybrid couplers are one of the critical components, providing an equal output power of -3 dB with a 90◦ phase difference for their output ports. Figure 24(a) shows the configuration of the designed SIW hybrid coupler. These couplers are well-known as Riblet short slot couplers [157]. In the designed coupler, the divided output power and phase shift can be adjusted by changing the dimensions of the slot coupling section. The scattering parameters of the proposed coupler are shown in figure 24(c) for the 26-32 GHz range. It is shown in this figure that the EM power is approximately -3 dB in the whole bandwidth for ports 2 and 3. The parameters S_{11}, S_{21}, S_{31}, and S_{41} indicate reflection coefficient, directivity, coupling coefficient, and isolation, respectively. Within the operating bandwidth, it can be seen that S_{11} and S_{41} are less than -20 dB. Compared to the theoretical hybrid 90°, the phase error for the proposed coupler is approximately one degree.

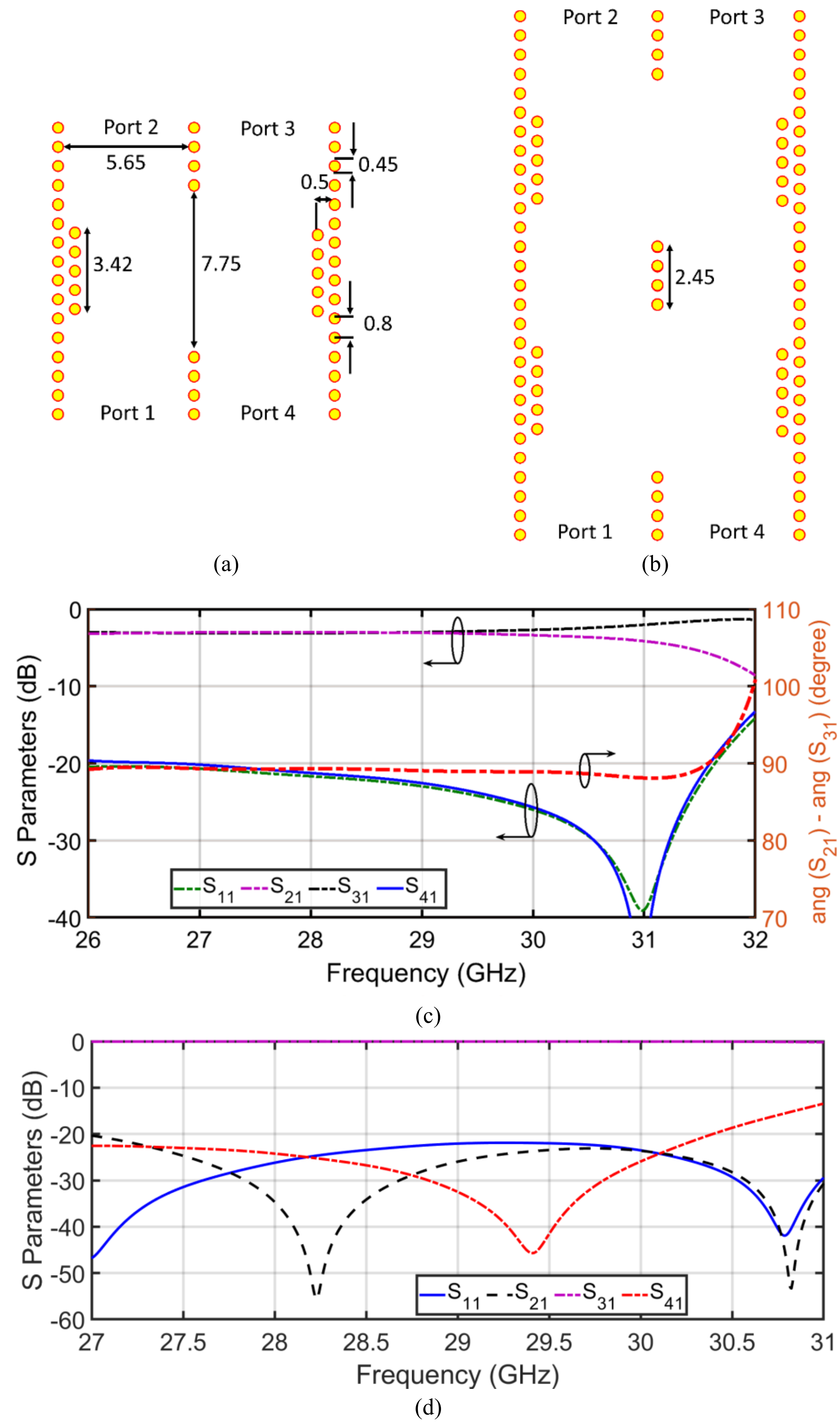

Figure 24. Detailed topology of the designed feeding line; (a) hybrid coupler, and (b) crossover (the dimensions are in mm). (c) Simulated scattering parameters of the hybrid coupler and the phase difference of its outputs. (d) Simulated scattering parameters of the proposed cross over.

Figure 24(b) shows the proposed crossover. It is designed with a cascaded connection between two hybrid couplers. The simulated scattering parameters for the proposed crossover are illustrated in figure 24(d).

B. 2) Phase Shifters:

The phase shifters play an essential role in providing the stable output phase difference required by phased arrays. Figure 25 (a) and (b) illustrate the geometry for 135- and 0-degrees phase shifters, respectively. A SIW channel's phase constant changes by varying the width of its wide wall. Figure 25 illustrates how the SIW wide wall should be changed in order to achieve 135 and 0 degrees of phase shifting.

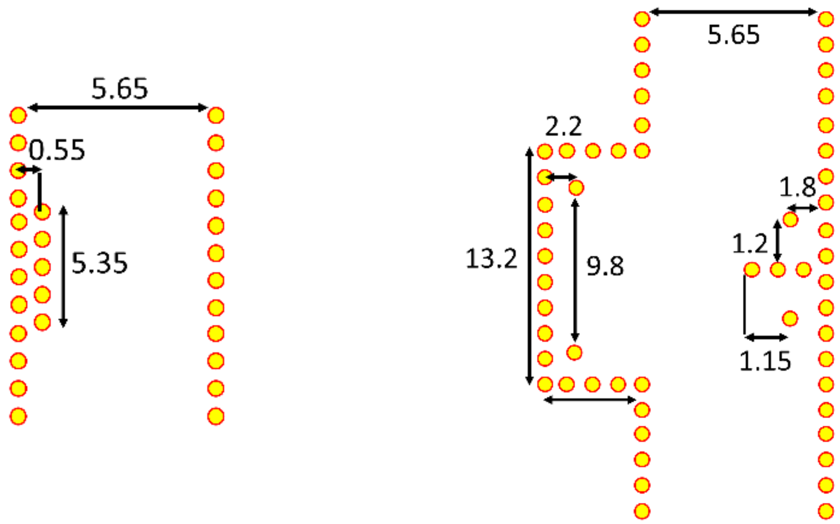

(a) (b)

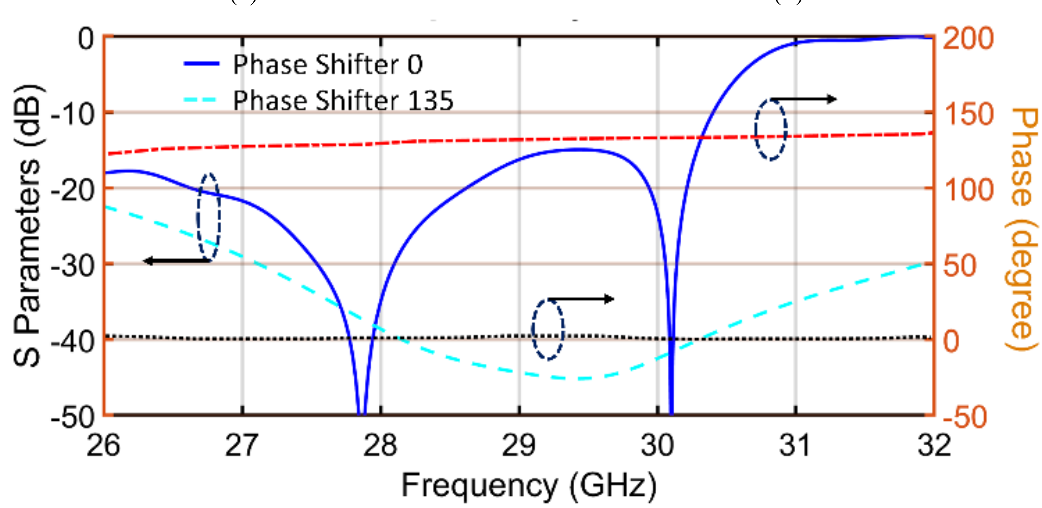

(c)

Figure 25. Detailed topology of the designed phase shifter with the substrate integrated waveguide (SIW); (a) 135 degree, and (b) 0 degree. (c) Simulated return loss and phase difference of the designed phase shifters of 135 and 0 degrees.

On the 26-32 GHz frequency spectrum, scattering parameters and phase differences for 135° and 0° phase shifters are shown in figure 25(c). From this figure, it can be seen that the phase error for 135- and 0-degrees phase shifters is less than four degrees.

B. 3) Butler Matrix:

An overall view of the proposed BFN is shown in Figure 23. It consists of two orthogonal Butler matrixes. The proposed BFN is designed on a single PCB laminate of Rogers 5880 (εr = 2.2 and tanδ = 0.009) with a thickness of 0.81 mm. The designed Butler Matrix is comprised of four 3-dB hybrid couplers, two SIW phase shifters and two crossovers as shown in Fig. 23. Each Butler Matrix has four input ports (namely Port 1, 2, 3, and 4) and four output ports (namely Port 5, 6, 7, and 8). In the configuration of the proposed Butler Matrix, the phase difference between output ports depends on input port excitation. Based on the excitation of each input port, the following table shows the phase differences between the output ports.

Table 3**.** Relationship between input ports and progressive phase when each input port is excited individually.

Input Ports	Output Ports				Progressive Phase
	Port5	Port6	Port7	Port8	
Port1	-270°	-135°	0°	135°	+135°
Port2	90°	45°	0°	-45°	-45°
Port3	-90°	-45°	0°	45°	+45°
Port4	270°	135°	0°	-135°	-135°

The phase differences between two adjacent output ports after the excitation of input ports are revealed in table 3. It can be seen that the phase differences between two adjacent output ports of the proposed Butler after the excitation of ports 1, 2, 3, and 4 are 135◦, −45◦, 45◦, and −135◦, respectively.

Figure 26 depicts the electrical distribution fields of the proposed Butler matrix. The simulated scattering parameters of the input ports 1 and 2 of the Butler matrix are shown in Figure 27. For excitation in port 1, the reflection coefficient (S_{11}) is less than -15 dB in the frequency spectrum 25-30.5 GHz. In addition, the transmission coefficients of port 1 are around -6dB after excitation.

Figure 27(b) shows the scattering parameters of the proposed Butler matrix when Port 2 is excited. As the proposed Butler matrix has a symmetric topology, the simulated result for Port 1 is the same as Port 4 (and Port 2 is the same as Port 3). Consequently, we don't report the scattering parameters for Ports 3 and 4.

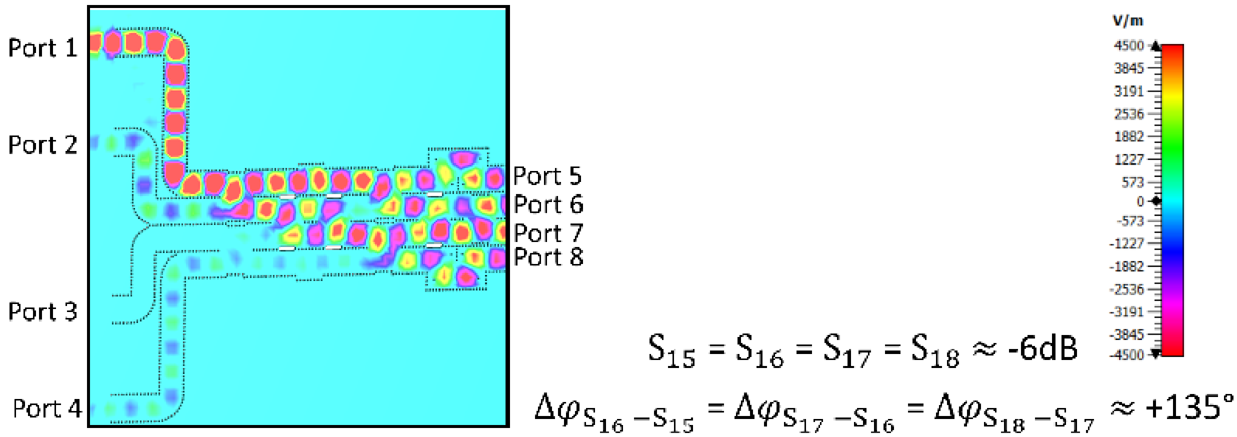
Port 1
Port 2
Port 3
Port 4
Port 5
Port 6
Port 7
Port 8
V/m
4500
3845
3191
2536
1882
1227
573
0
-573
-1227
-1882
-2536
-3191
-3845
-4500
$S_{15} = S_{16} = S_{17} = S_{18} \approx$ -6dB
$\Delta\varphi_{S_{16}-S_{15}} = \Delta\varphi_{S_{17}-S_{16}} = \Delta\varphi_{S_{18}-S_{17}} \approx +135°$

(a)

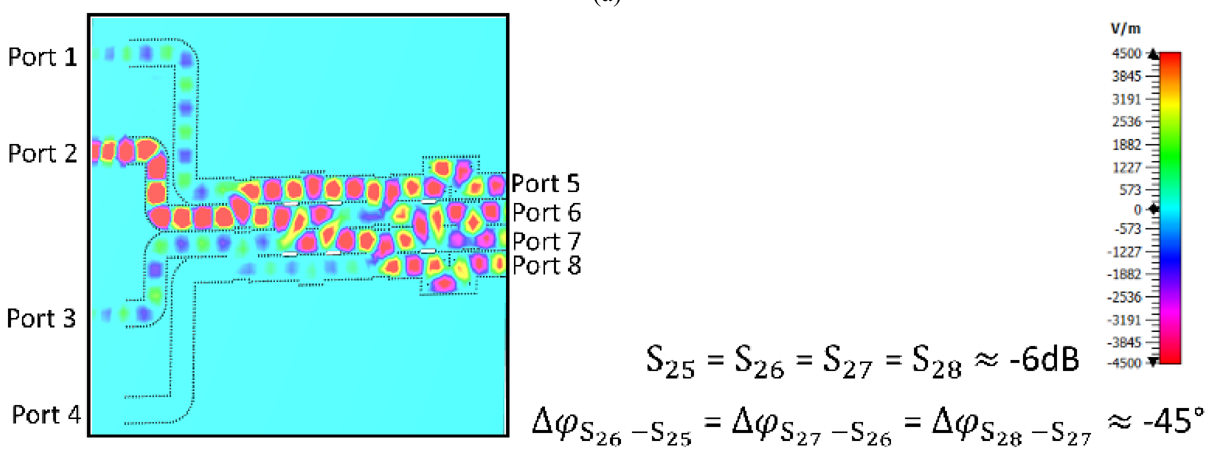
Port 1
Port 2
Port 3
Port 4
Port 5
Port 6
Port 7
Port 8
V/m
4500
3845
3191
2536
1882
1227
573
0
-573
-1227
-1882
-2536
-3191
-3845
-4500
$S_{25} = S_{26} = S_{27} = S_{28} \approx$ -6dB
$\Delta\varphi_{S_{26}-S_{25}} = \Delta\varphi_{S_{27}-S_{26}} = \Delta\varphi_{S_{28}-S_{27}} \approx -45°$

(b)

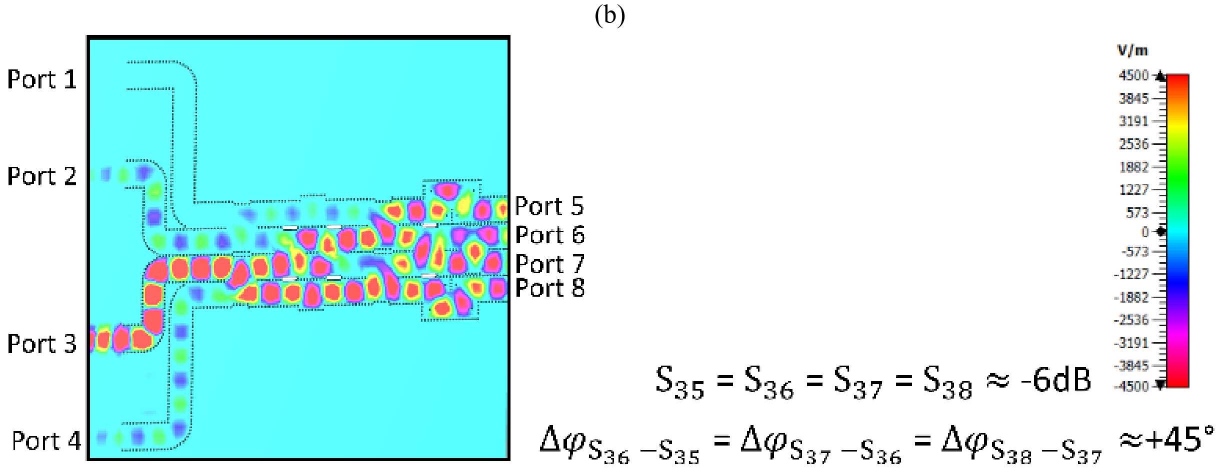
Port 1
Port 2
Port 3
Port 4
Port 5
Port 6
Port 7
Port 8
V/m
4500
3845
3191
2536
1882
1227
573
0
-573
-1227
-1882
-2536
-3191
-3845
-4500
$S_{35} = S_{36} = S_{37} = S_{38} \approx$ -6dB
$\Delta\varphi_{S_{36}-S_{35}} = \Delta\varphi_{S_{37}-S_{36}} = \Delta\varphi_{S_{38}-S_{37}} \approx +45°$

(c)

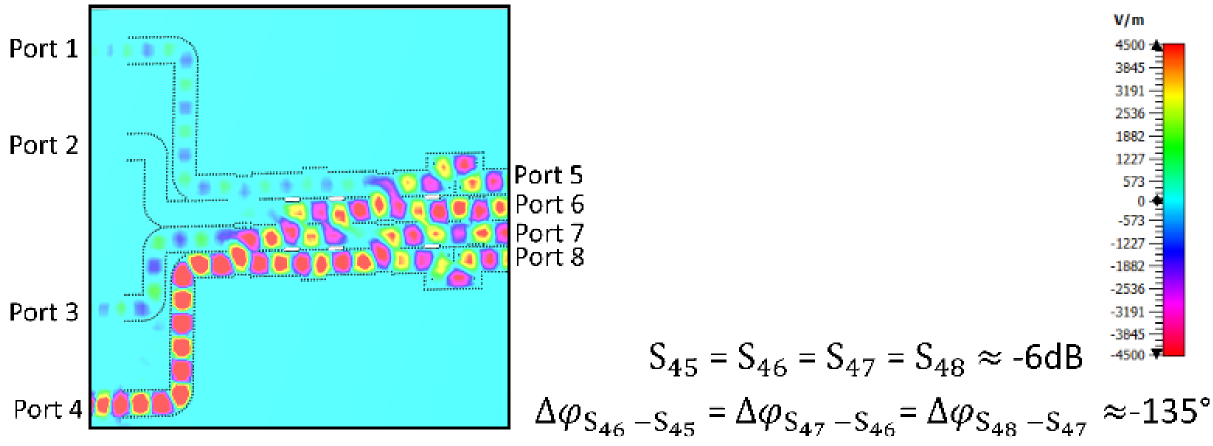

(d)

Figure 26. Procedure of the switched beam transmission from the proposed Butler matrix to the propagation unit by showing the EM field distributions of different port excitations of (a) Port 1, (b) Port 2, (c) Port 3, and (d) Port 4.

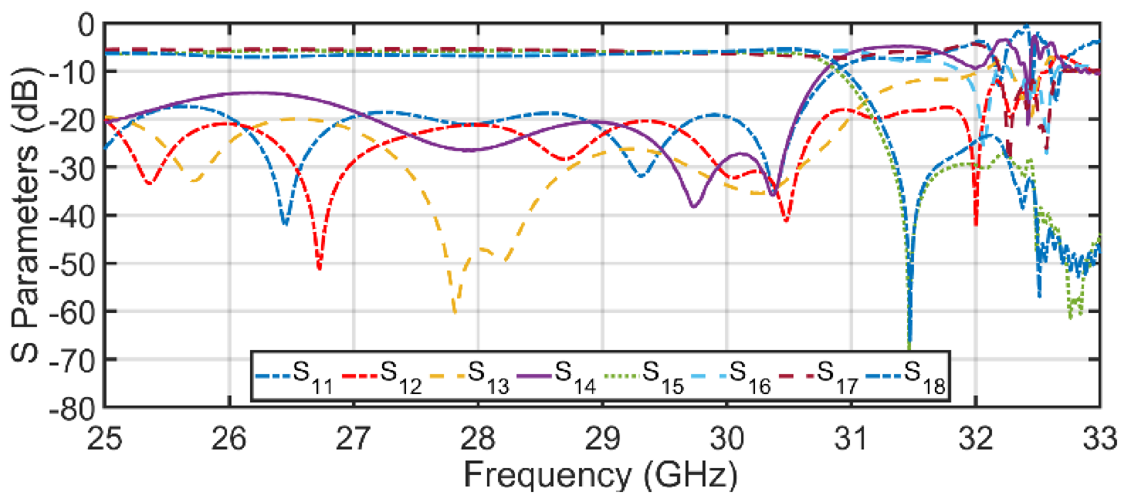

(a)

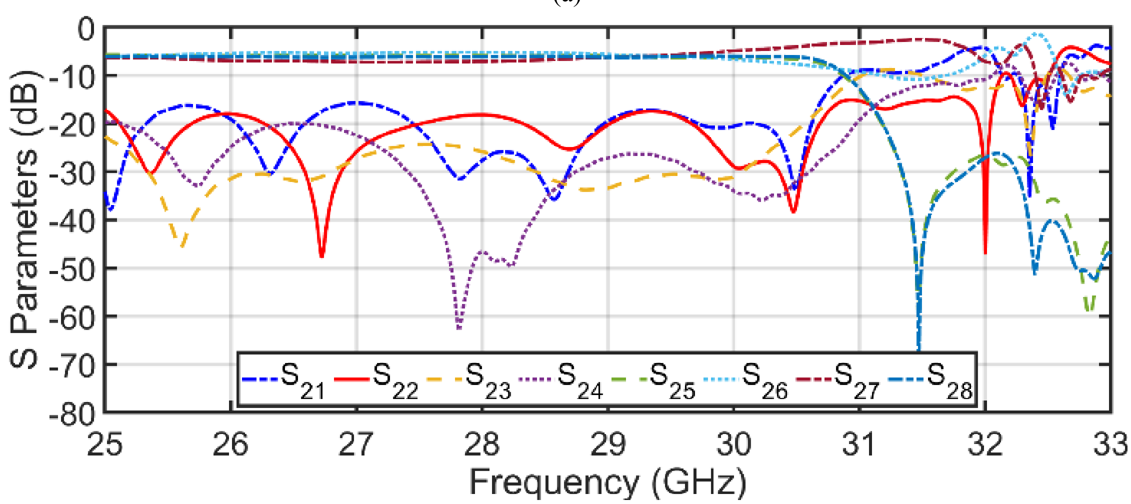

(b)

Figure 27. Simulated scattering parameters of the designed Butler matrix with SIW topology. (a) Excitation of Port 1. (b) When Port 2 is excited.

Table 3 shows the relationship between input ports and progressive phase, when each input port of Butler matrix (along X- or Y- axis) is excited individually. There are three more excitation states included in the proposed Butler Matrix in addition to the states mentioned in table 3. When two input ports are excited simultaneously, these states occur. Table 4 explains how the proposed BFN could provide more progressive phase.

In table 4, these three states are identified as State M1, State M2, and State M3. State M1 refers to the scenario in which Ports 1x and 2x (or Ports 1y and 2y) are excited concurrently with the same amplitude and phase. State M2 is activated as Ports 1x and 3x (or Ports 1y, and 2y) are excited simultaneously with the same amplitude and a +90° phase difference. State M3 is activated as Ports 2x and 4x (or Ports 2y, and 4y) are excited simultaneously with the same amplitude and a -90° phase difference. The amplitude and phase of Butler Matrix's outputs for three states of the excitation named States M1, M2, and M3 are reported in table 4.

Table 4**.** Relationship between input ports and progressive phase when two input port are excited simultaneously.

Input Ports	Amplitude and phase	Output Ports				Progressive Phase
		Port5	Port6	Port7	Port8	
Port2 & Port3 = State M1	Same amplitude and phase	0°	0°	0°	0°	0°
Port1 & Port3 = State M2	Same amplitude and out of phase	-180°	-90°	0°	90°	90°
Port2 & Port4 = State M3	Same amplitude and out of phase	180°	90°	0°	-90°	-90°

C. Antenna Topology:

In the proposed structure, the antenna layer is printed on a Rogers 4003C PCB laminate with (εr = 3.55 and tanδ = 0.0027) thickness of 0.8 mm. The antenna layer comprises a cluster of radiating patches arranged symmetrically in four rows and four columns, together with a series of high-impedance microstrip lines (width of 0.25 mm and length of 3 mm), as shown in figure 28(a).

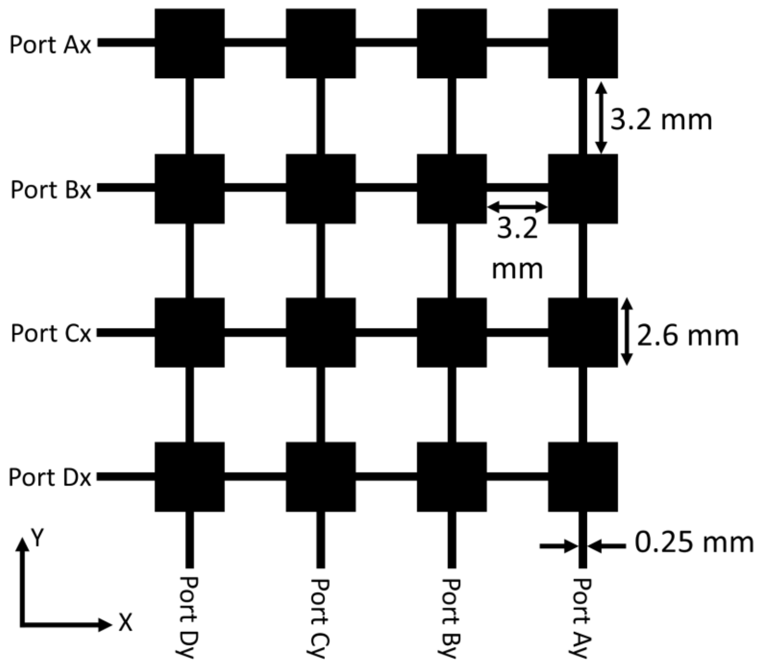

(a)

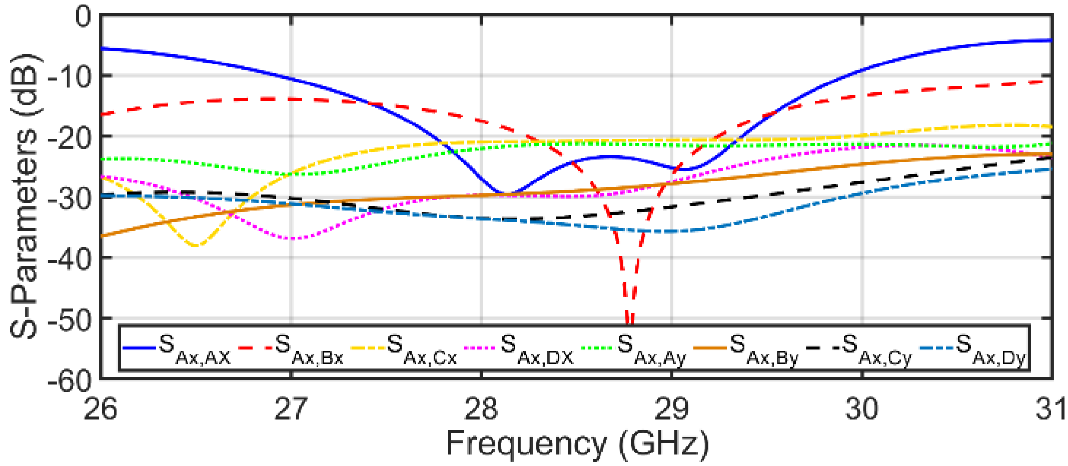

(b)

Figure 28. The arrangement of the square patches used as antenna layer for proposed structure. (b) Simulated S parameters of the proposed antenna array.

The simulated scattering parameters of the proposed array for Port Ax are shown in figure 28(b). It can be observed that impedance matching (<-10 dB) for this port is from 27 to 30 GHz. Moreover, the isolation between Port Ax and other ports is larger than 13 dB in the whole operating bandwidth.

In order to study the beam-scanning capability of the proposed array antenna, different values of the phase are adjusted for input ports. Figure 29 shows the 3-D radiation patterns and some properties, such as beam position and input phase. In the corner of each radiation pattern, the required value of input phase is written. These values can be achieved by the proposed Butler matrix.

The input ports are excited with uniform amplitudes with different phase distributions, which allows the antenna array to radiate beams tilted at different angles. According to phased array theory, the following formula can be used to calculate the beam pointing angles β [158]:

$$\beta = 90° - \cos^{-1}(-\frac{\alpha}{kd})$$

where $\boldsymbol{\alpha}$, k, and d represent the phase difference, the wave-number, and the distance between element, respectively. By selecting the α values to 0, ±π/4, ±π/2 and ±3π/4, the beam position will be approximately appeared at angles 0°, ±14°, ±28° and ±43°, respectively. The different graphs of figure 29 clarify that at each step, the different beam positions are near 0°, ±14°, ±28° and ±43° for different directions.

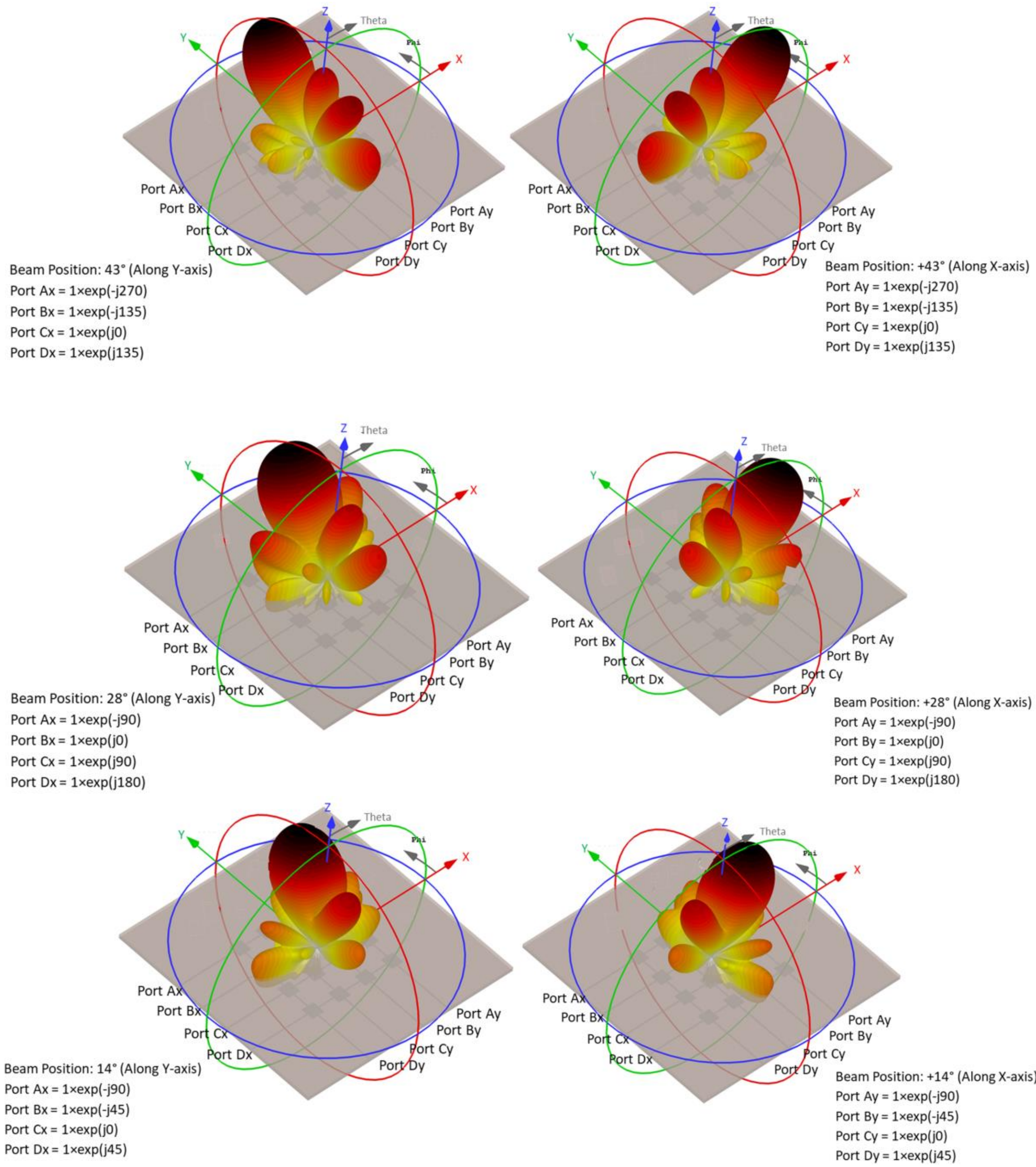

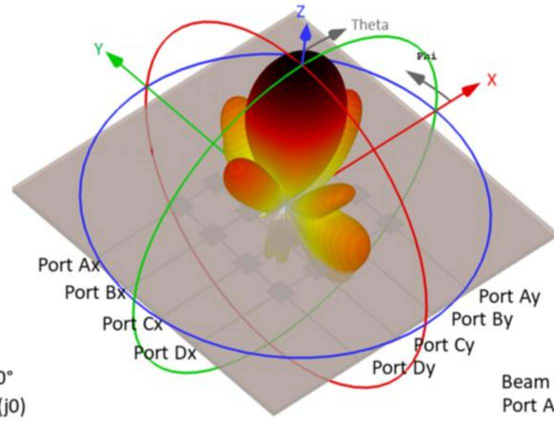

Beam Position: 0°
Port Ax = 1×exp(j0)
Port Bx = 1×exp(j0)
Port Cx = 1×exp(j0)
Port Dx = 1×exp(j0)

Or

Beam Position: 0°
Port Ay = 1×exp(j0)
Port By = 1×exp(j0)
Port Cy = 1×exp(j0)
Port Dy = 1×exp(j0)

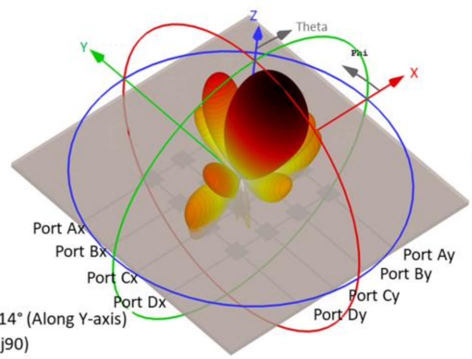

Beam Position: -14° (Along Y-axis)
Port Ax = 1×exp(j90)
Port Bx = 1×exp(j45)
Port Cx = 1×exp(j0)
Port Dx = 1×exp(-j45)

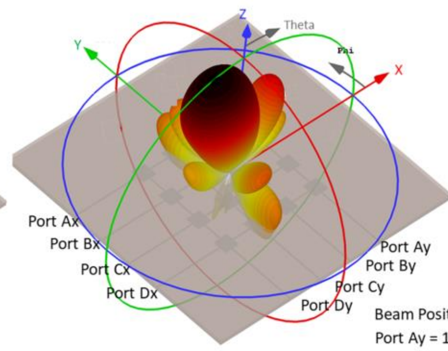

Beam Position: -14° (Along X-axis)
Port Ay = 1×exp(j90)
Port By = 1×exp(j45)
Port Cy = 1×exp(j0)
Port Dy = 1×exp(-j45)

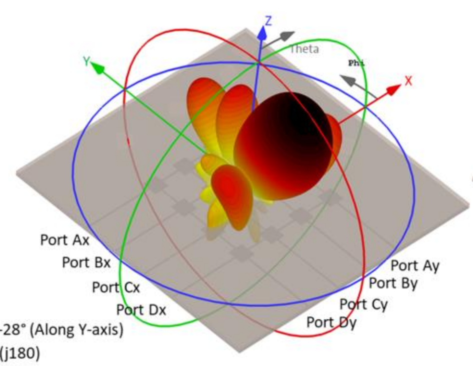

Beam Position: -28° (Along Y-axis)
Port Ax = 1×exp(j180)
Port Bx = 1×exp(j90)
Port Cx = 1×exp(j0)
Port Dx = 1×exp(-j90)

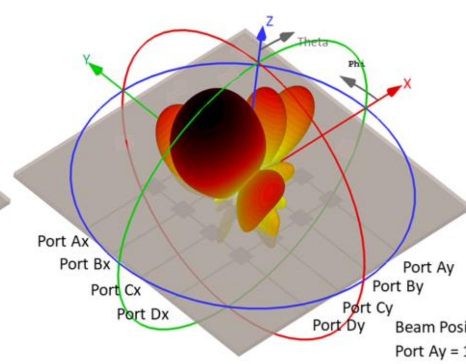

Beam Position: -28° (Along X-axis)
Port Ay = 1×exp(j180)
Port By = 1×exp(j90)
Port Cy = 1×exp(j0)
Port Dy = 1×exp(-j90)

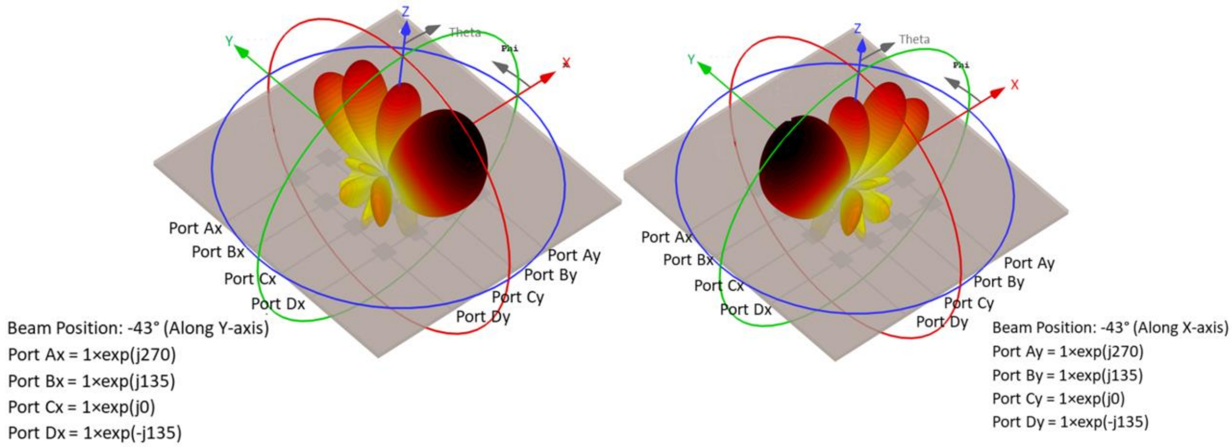

Figure 29. Simulated 3-D radiation patterns of the proposed antenna array with uniform amplitude and different phases at 28 GHz frequency.

D. Feeding Mechanism through half cavity transition:

In the proposed multifunctional architecture, a coupling mechanism is implemented to carry EM power out from the output of BFNs to the antenna array inputs. This coupling mechanism is comprised of eight half-circle cavities. Figure 30 illustrates the different perspectives of the proposed coupling topology.

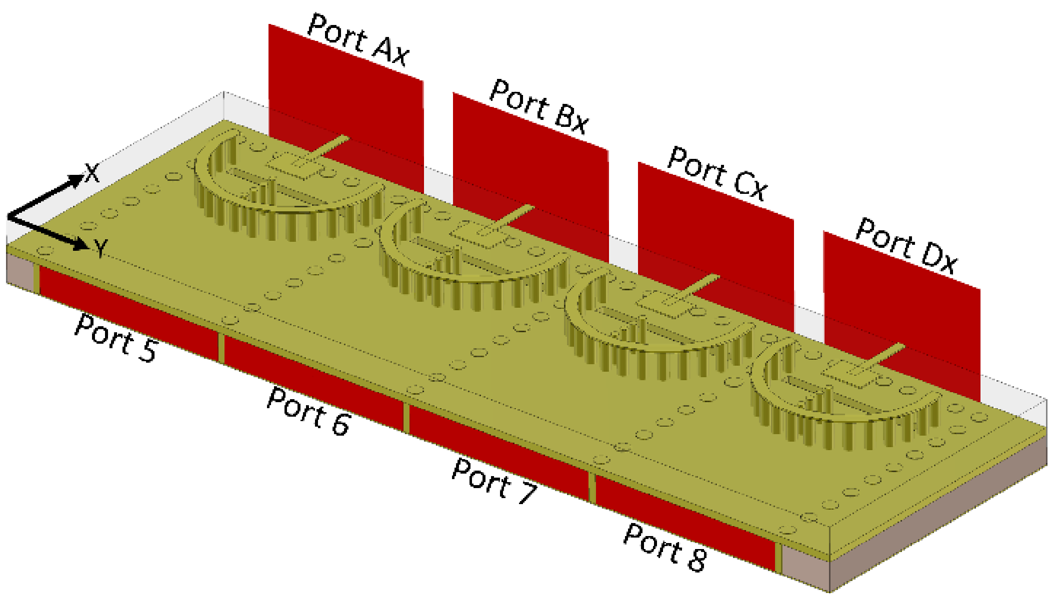

(a)

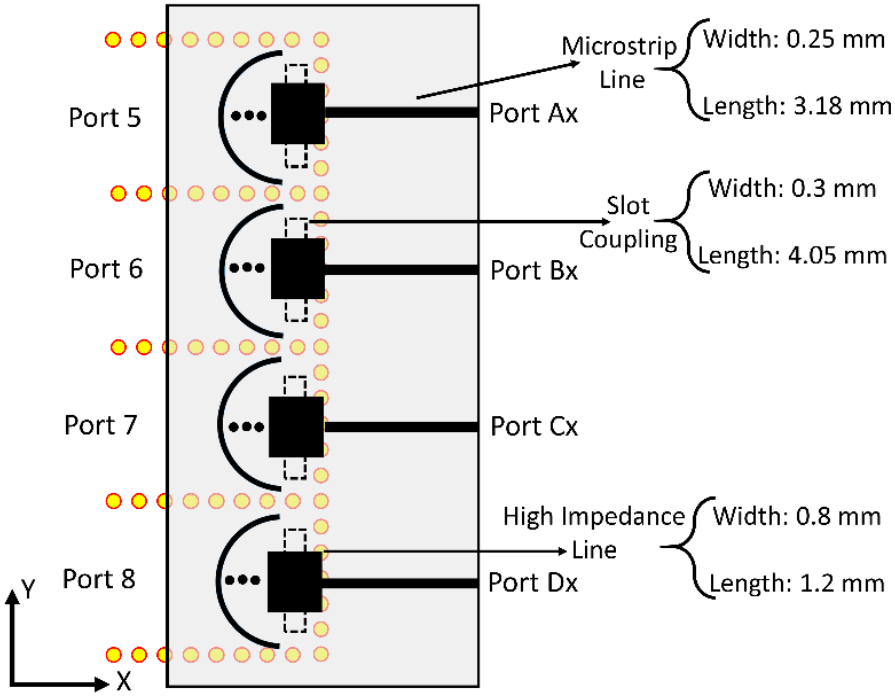

Port 5
Port 6
Port 7
Port 8
Port Ax
Port Bx
Port Cx
Port Dx
Microstrip Line
Width: 0.25 mm
Length: 3.18 mm
Slot Coupling
Width: 0.3 mm
Length: 4.05 mm
High Impedance Line
Width: 0.8 mm
Length: 1.2 mm
Y
X

(b)

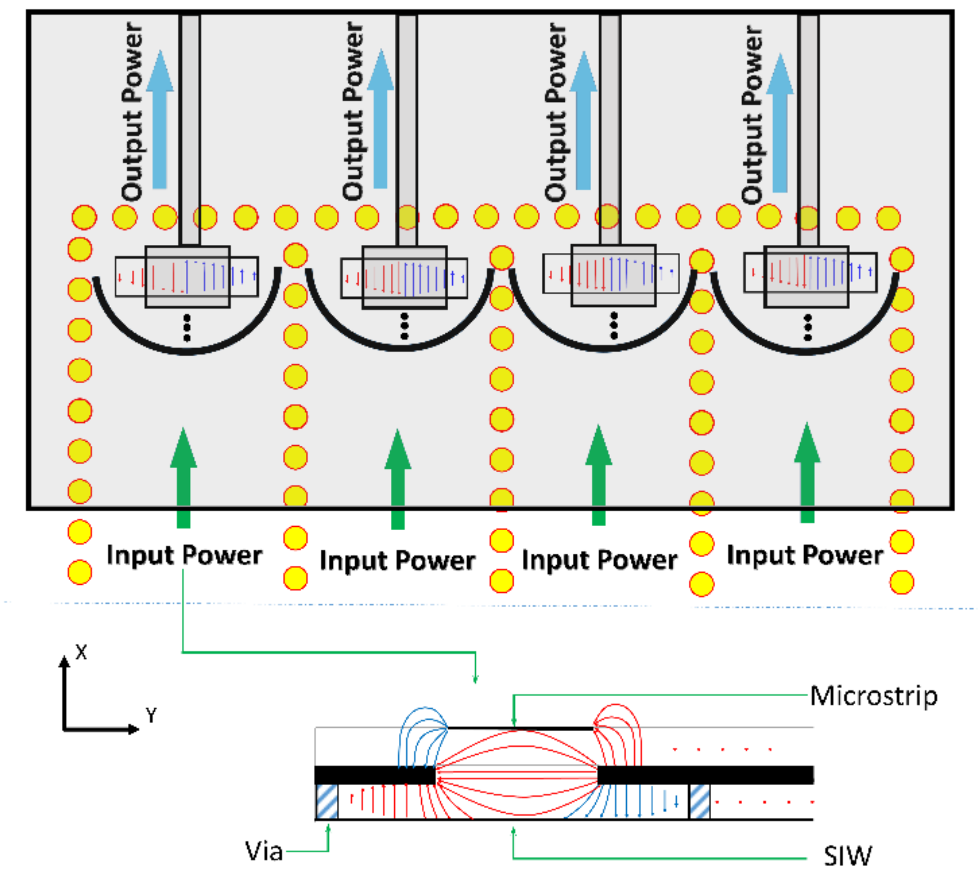

Output Power
Output Power
Output Power
Output Power
Input Power
Input Power
Input Power
Input Power
X
Y
Microstrip
Via
SIW

(c)

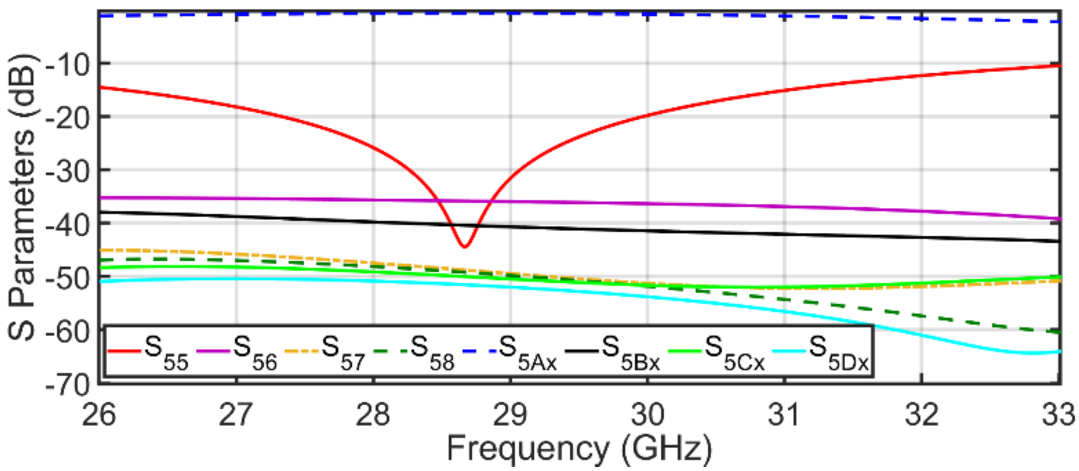

(d)

Figure 30. (a) 3D view of the proposed coupling mechanism. (b) Top view of the proposed SIW-slot-microstrip line transition. (c) The mechanism of electric fields of the proposed transition. (d) Simulated scattering parameters.

In the proposed coupling structure, Ports 5, 6, 7, and 8 are the same as output ports of the proposed Butler matrix (refer to figure 6). Meanwhile, Ports Ax, Bx, Cx, and Dx are the same as antenna array inputs (refer to figure 28(a)).

The proposed coupling system connects the output ports of the Butler matrix to the input ports of the antenna array through a coupling mechanism. In the proposed beamforming system, two identical coupling transitions can be observed; one along the X-axis and another along the Y-axis. Indeed, these coupling systems connect Butler matrices to the proposed antenna array to form a 2D beamforming system. In the proposed beamforming system, the process of propagating EM signals from the input ports of the Butler matrix toward the antenna is as follows. First, one of the input ports of the Butler matrices is activated. Through that port, the EM signal reaches the output ports of the Butler network. After that, the EM signals are transferred to the half-circle cavities by the created slots. These cavities direct the EM signals toward the microstrip lines that feed the antenna array. Using half-circle cavities around slot coupling brings several benefits. First, they contribute to transferring EM powers from the lower layer to the top layer more efficiently. Actually, cavities are associated to avoid unwanted radiation and emissions from slot-to-microstrip transition. Second, the slot-to-microstrip transitions often could cover a narrow operating bandwidth. The scattering parameters of the proposed coupling mechanism show that the proposed transition covers a frequency spectrum from 26 to 33 GHz. Moreover, from simulation results can be seen the isolation between input ports of the proposed coupling mechanism is more than 35 dB in the whole operating bandwidth. The cavities play an important role to suppress mutual coupling between adjacent slot-to-microstrip transitions.

E. Solar Panel Model and Integration:

Here a multifunctional system to create a communication link between vehicle and the sky for short to medium range communications. There is plenty of free space to add solar cells to the vehicle's roof top as shown in Figure 21 (target design). This surface covered with solar panels can generate a stable power supply for moving cars during the day, allowing them to store enough energy. An innovative study is proposed here, which aims to integrate an antenna propagation mechanism to the roof of the car in order to create a communication link with the sky [159]. Signal propagation and solar energy harvesting should have minimal interaction in this link. In this system several mono solar cell panels can surround the entire area around the antenna aperture. A suggested application for this structure is to be installed on the top roof of an upcoming generation of electric vehicles (design concept).

This section describes the information on a solar cell unit. A set of sixteen numbers of rectangular solar cell units (30 mA, 5V, 0.15 Watt) with dimensions of 53×30×5 mm3 are used in the proposed structure in the process of experimental measurement. These solar cells can generate 2.4 Watts of electrical power in total. This power is enough for the required microwave components for the antenna receive section including RF switches and amplifiers in a packed system. In addition to this integration with the propagation unit, additional solar panels can be mounted on a vehicle's roof to provide power for other functions. Figure 31 shows a photograph of used solar panels. In our full-wave simulator, CST Microwave Studio software, a dielectric material with properties of permittivity constant 1.5 and loss tangent 10 was used to model the solar panel layer [160].

Figure 31. Photo of used flexible solar cell panels.

F. Proposed Multifunctional Antenna Integrated with Solar Panels: Simulated Results and Performance

Figure 22 indicates the overall geometry of the proposed multifunctional antenna system that is integrated with solar panels. It is composed of three stacked layers including an antenna layer, BFN, and a solar panel layer. This section explains how layers are accompanied together to form the proposed system. Then the obtained simulation results of the proposed system are collected here. As shown in Figure 22, two SIW Butler matrix are orthogonally used in the lowest layer to provide the desired amplitude and phase to antenna array inputs. A topology of eight half-circle cavities propagates EM fields to the patch array using an aperture coupling mechanism. Cavities and eight slot-to-microstrip transitions provide aperture coupling mechanisms in the proposed structure. The proposed coupling mechanism ensures the existence of suitable isolation between the feed network and radiation face, suppressing the spurious emission from the feed network.

The solar panels are located on a surface where the system has a limited current distribution. Therefore, there is no interference between the solar panels and the offered array antenna on this surface. In the proposed system, a large number of solar cells could be used to surround the space around the physical aperture of the antenna array. However, only 16 solar panels have been used in the prototype to provide continuous energy for the system. The topology of the proposed prototype is designed such that the physical aperture of the antenna array is the smallest portion of the system, and its radiation performance has not been affected by adjacent solar cells. In commercial products of the proposed system, the number of solar panels could be increased.

The proposed system has eight input ports isolated from each other, namely Port 1x, Port 2x, Port 3x, Port 4x, Port 1y, Port 2y, Port 3y, and Port 4y. In Figure 32, the proposed system's simulated S parameters are shown. In view of the symmetrical topologies of the proposed antenna array and Butler matrices, Port 1x and Port 2x are expected to have the same S-parameters as Port 3x and Port 4x. The same is true for ports along the Y-axis as well. On the other hand, due to the symmetric structure, the scattering parameters of Port 1x, Port 2x, Port 3x, and Port 4x are as same Port 1y, Port 2y, Port 3y, and Port 4y, respectively. Consequently, in this paper, the simulated S-parameters for Port 1x, and Port 2x were only reported.

Figure 32(c) depicts simulated realized gain for the proposed system. Due to the symmetric structure, the realized gain is only reported for different types of excitation along the x-axis. From Figure 32 can be found that the return losses (<-10 dB) for Port 1x and Port 2x cover a frequency spectrum from 27-30 GHz. Additionally, the simulated scattering parameters show that isolation between input ports is approximately less than 15 dB in the whole operating bandwidth.

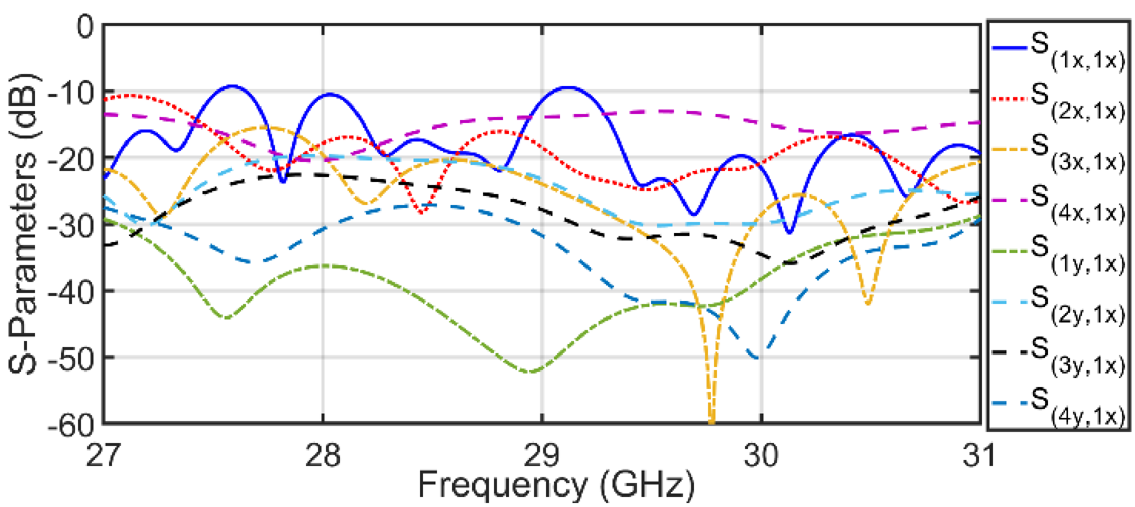

(a)

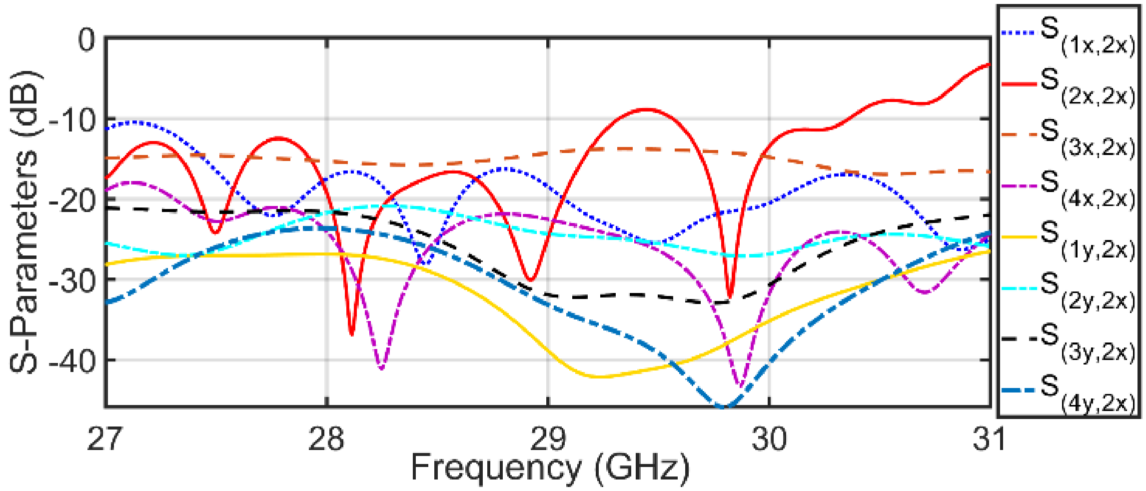

(b)

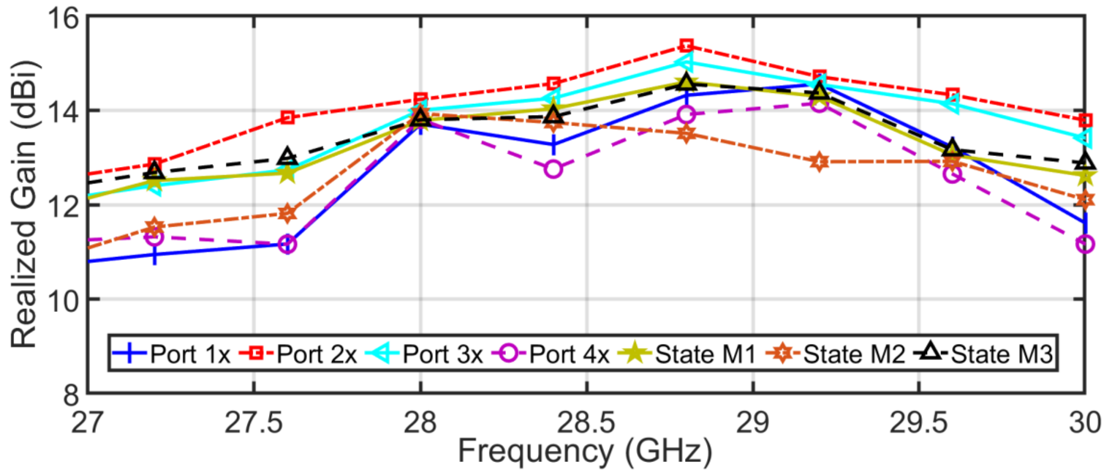

(c)

Figure 32. Simulated performance of the proposed multifunctional beamforming system. Scattering parameters: (a) when Port1x is excited. (b) When Port2x is excited. (c) Realized gain.

Figure 33 illustrates the simulated radiation patterns at 28 GHz. As shown in previous section (refer to figure 29), if the output phase of the designed BFN is set (according to mentioned values in figure 29) to the inputs of the proposed array, the antenna array could be able to scan angles of 0°, ±14°, ±28°, and ±43°. However, by a simple comparison can be found that there is a small deviation from the expected angles in figure 33 compared to figure 29. This deviation appears after connecting the proposed BFN to antenna array. These slight deviations can be explained by one fact. In figure 29, there was no BFN and the desired phase for scanning was manually entered into the input ports of the proposed array. After directly connecting BFN to the proposed antenna array, the effective ground size of the antenna would be increased. In this circumstance, the ground size of the structure effects on beam position and deflects it slightly. The simulated results of the proposed multifunctional structure show that after the excitation of Butler's input ports (according to tables 3 and 4), the main beam position touches angles of -38°, -27°, -12°, +1°, +15°, 26°, and +39°. In order to better understand the system's radiation performance, a 2D radiation pattern at two cutting planes XoZ and YoZ is shown in figure 33(a)-(b). Because of the symmetry structure, the simulated results of 2D radiation patterns at both XoZ and YoZ planes seem to be the same.

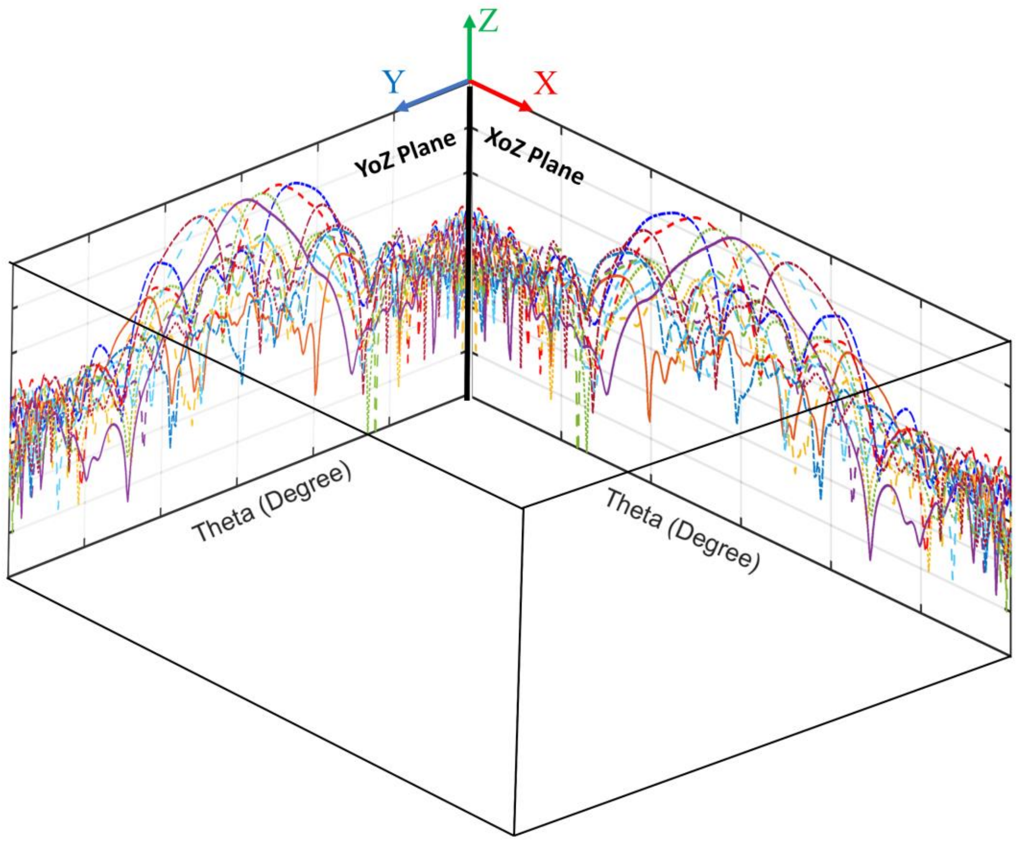

(a)

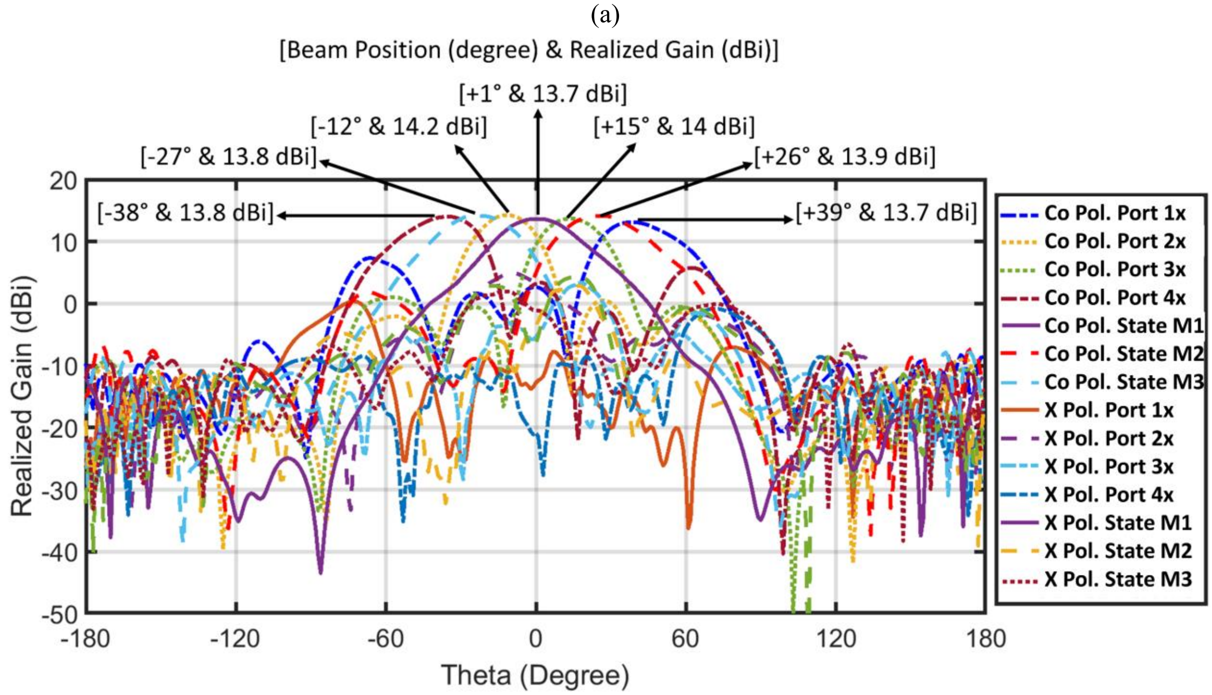

(b)

Figure 33. (a) 2D graph of the scanning capabilities of the proposed antenna array with different type of excitation at 28 GHz. (b) Radiation patterns at 28 GHz in YoZ plane. (Beam Position: BP). States M1, M2, and M3 refer to combination of excitations (Detail in table 4).

5.3.3 Fabrication and Experimental Results:

5.3.3.1 Antenna Characteristics:

In order to verify the obtained simulated results, a prototype of the proposed multifunctional antenna has been fabricated and experimentally measured. This fabricated prototype is shown in figure 34(a). It consists of two layers. Each layer was easily fabricated with PCB technology and then they were stacked together using plastic screws. Afterwards, the solar cells were placed on top of the feeding network.

A Spectrum Analyzer (Keysight, N9950B/0.3–32 GHz) has been used for the scattering measurement. The measured scattering parameters are shown in figure 34(b)-(c). Figure 34(b) shows the measured −10-dB reflection coefficient for all input ports. In summary, the measured impedance bandwidth for the proposed architecture supports a frequency range of 27 to 29.7 GHz. Moreover, the measured isolation between input ports were more than 15 dB over the whole operating bandwidth.

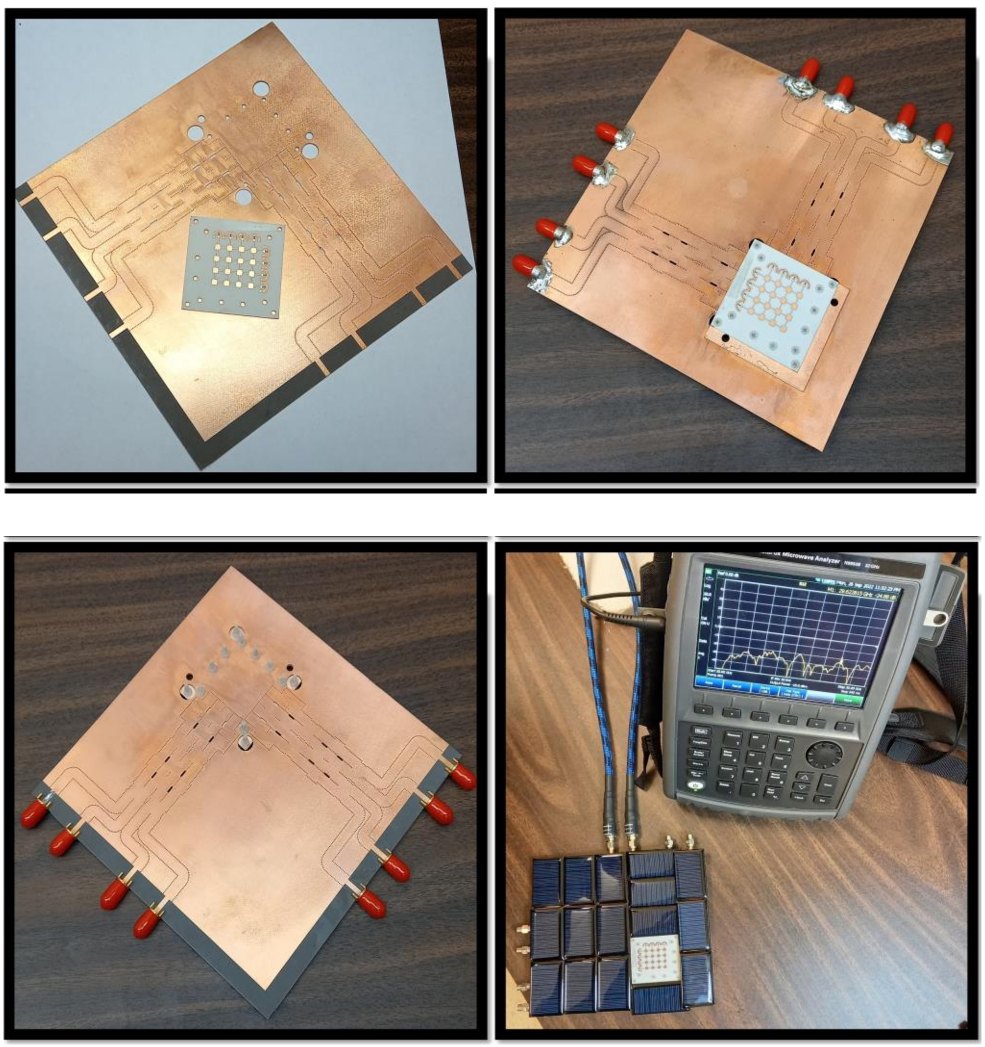

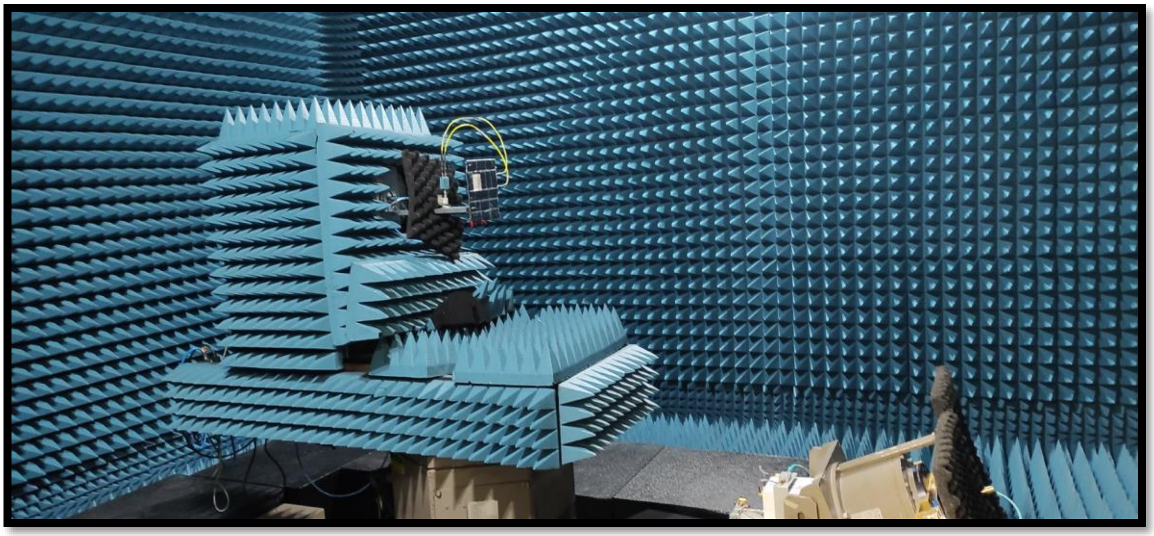

(a)

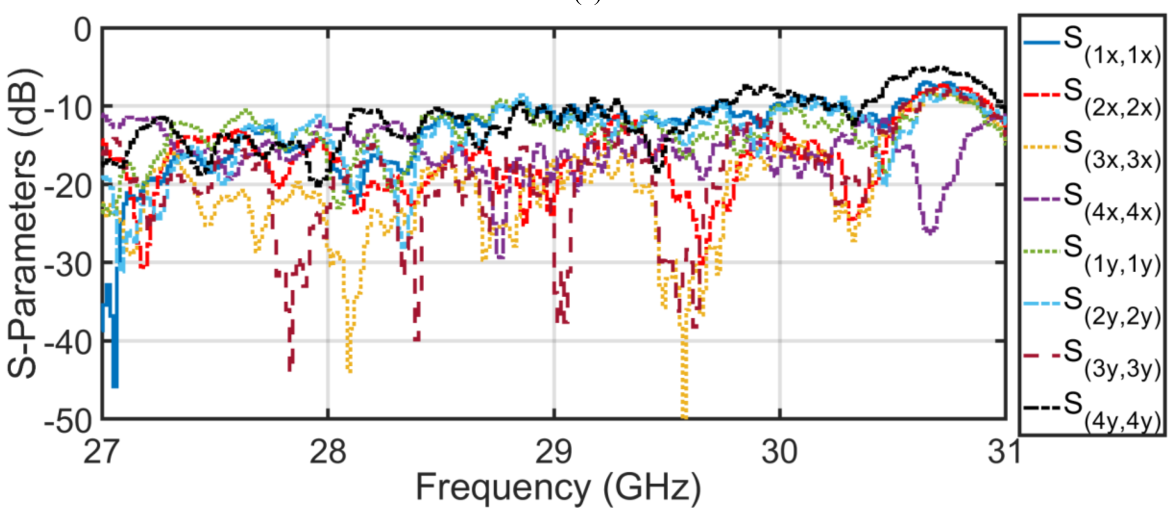
S-Parameters (dB)
0
-10
-20
-30
-40
-50
27
28
29
30
31
Frequency (GHz)
$S_{(1x,1x)}$
$S_{(2x,2x)}$
$S_{(3x,3x)}$
$S_{(4x,4x)}$
$S_{(1y,1y)}$
$S_{(2y,2y)}$
$S_{(3y,3y)}$
$S_{(4y,4y)}$

(b)

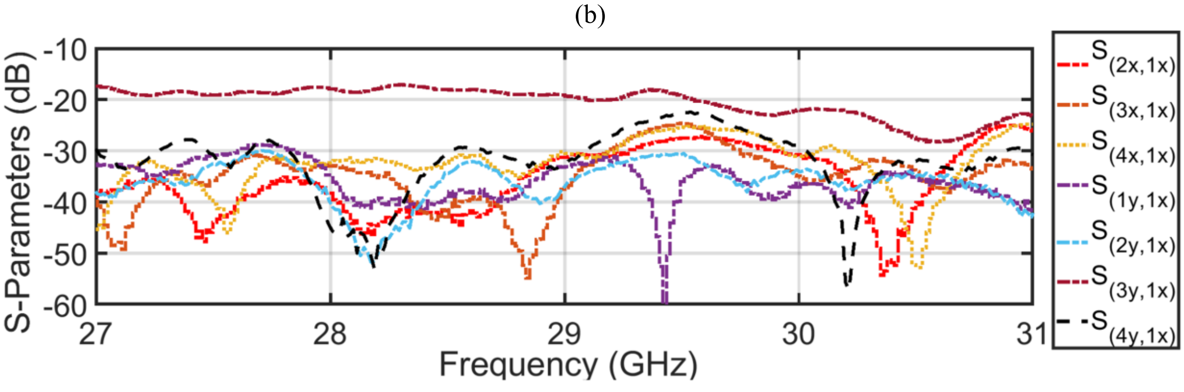
S-Parameters (dB)
-10
-20
-30
-40
-50
-60
27
28
29
30
31
Frequency (GHz)
$S_{(2x,1x)}$
$S_{(3x,1x)}$
$S_{(4x,1x)}$
$S_{(1y,1x)}$
$S_{(2y,1x)}$
$S_{(3y,1x)}$
$S_{(4y,1x)}$

(c)

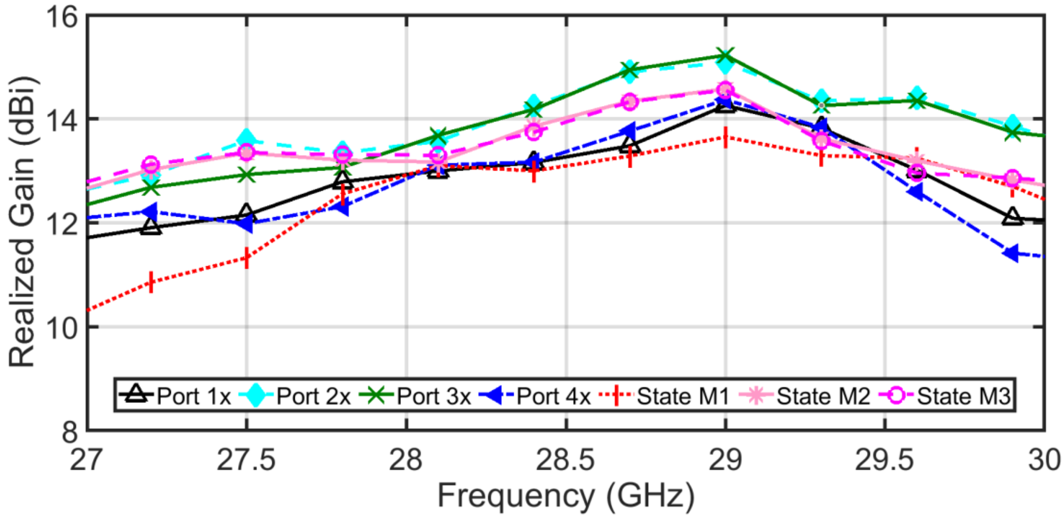

(d)

Figure 34. (a) Photographs of the proposed structure in detail. (top left: before assembly, top right: top view of the proposed antenna fed by a BFN, bottom left: the back view, and bottom right: fabricated multifunctional antenna integrated with solar panels). (b) Measured reflection coefficients for input ports. (c) Measured isolation between Port1x and other input ports. (d) Measured gain of the proposed antenna.

The proposed antenna system under test within the anechoic chamber for measuring its radiation characteristics can also be seen in figure 34 (a). To measure the radiation patterns of the prototype, a far field antenna chamber is exploited. The proposed antenna serves as a receiver, while a high-power emitter generates planar waves using a reflector screen. Both co- and cross-polarization patterns are also measured. For a standard horn antenna with constant gain, this radiation pattern mechanism is performed one more time. The power received by the horn antenna was noted carefully for further calculations. Then, by comparing the achieved results, a gain chart versus frequency is obtained. The calculated gains for the arrays are shown in figure 34(d) for different types of excitation. The maximum measured gain is 15.3 dBi at 29 GHz. The radiation patterns of the proposed antenna system were measured experimentally at 28 GHz. The 2D measured radiation patterns are depicted in figure 35. This section shows a 2D radiation pattern at two cutting planes YoZ and XoZ order to better understand the system's radiation performance. Then, cutting planes YoZ and XoZ are depicted in figure 35 (b) and (c), respectively. The radiation pattern shown in Figure 14 shows that the maximum side lobe level is about -10 dB at all scanning angles. The radiation efficiency of the proposed array is more than 70% in the whole operating bandwidth.

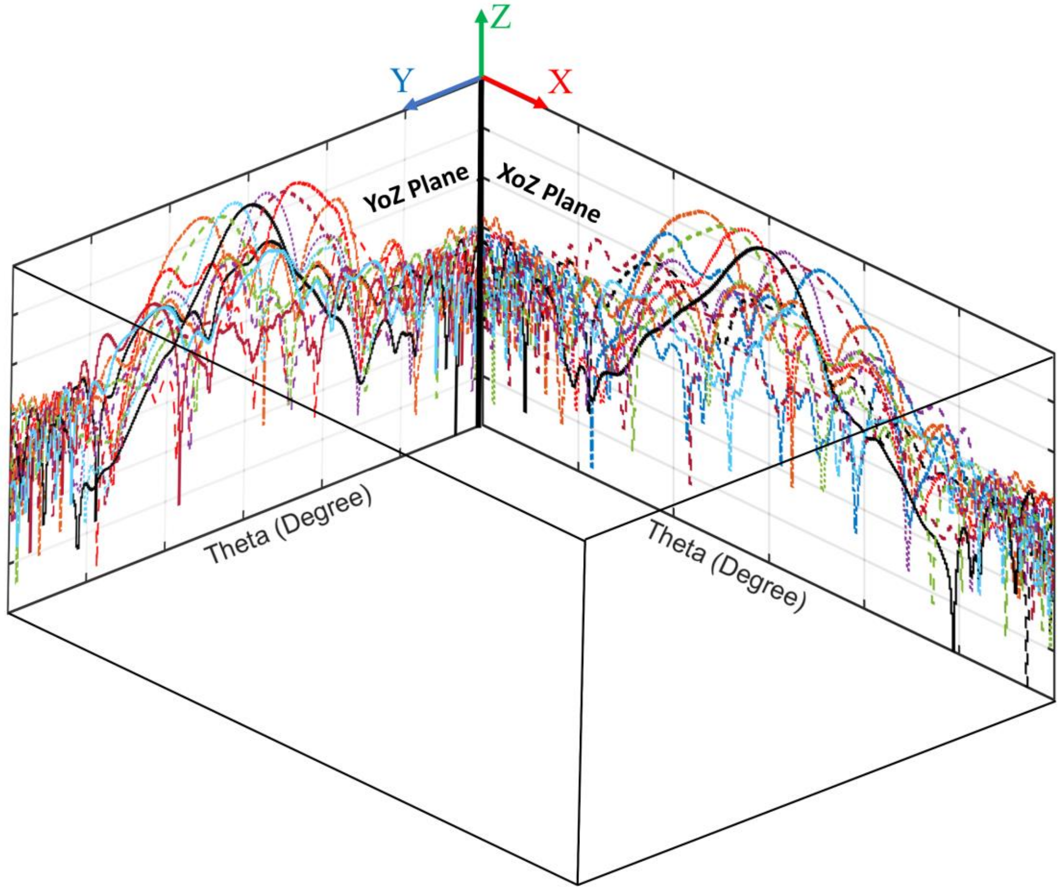
Z
Y
X
YoZ Plane
XoZ Plane
Theta (Degree)
Theta (Degree)

(a)

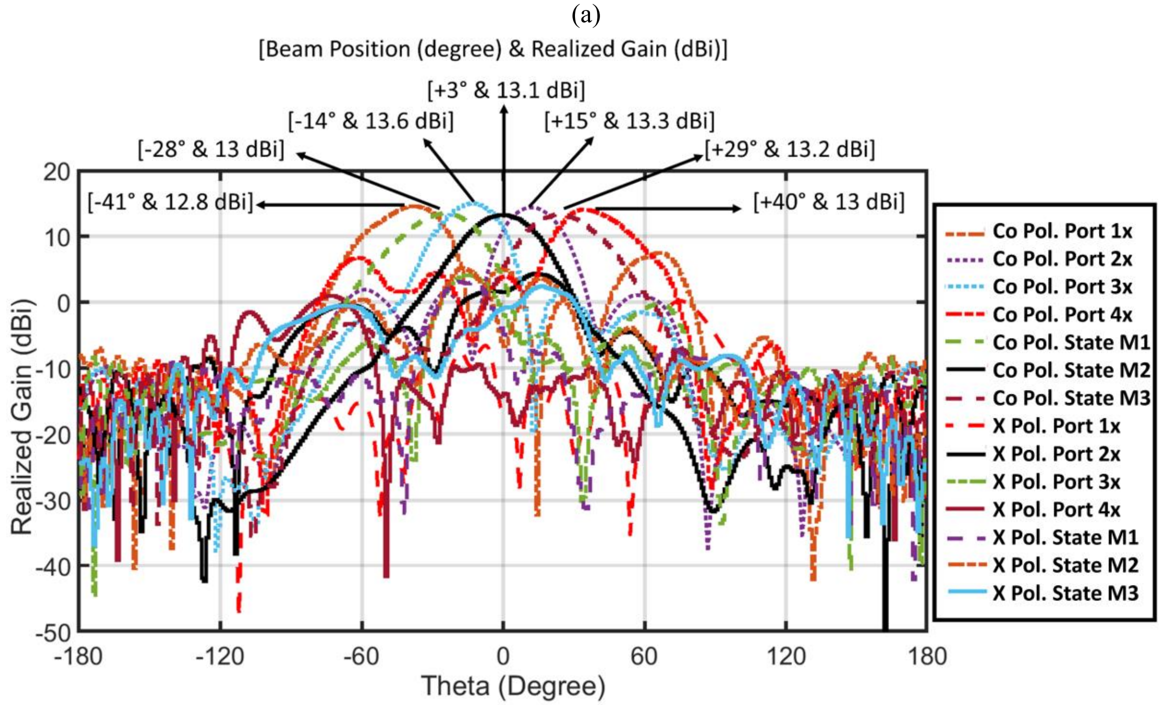
[Beam Position (degree) & Realized Gain (dBi)]
[+3° & 13.1 dBi]
[-14° & 13.6 dBi]
[+15° & 13.3 dBi]
[-28° & 13 dBi]
[+29° & 13.2 dBi]
[-41° & 12.8 dBi]
[+40° & 13 dBi]
Realized Gain (dBi)
Theta (Degree)
20
10
0
-10
-20
-30
-40
-50
-180
-120
-60
0
60
120
180
Co Pol. Port 1x
Co Pol. Port 2x
Co Pol. Port 3x
Co Pol. Port 4x
Co Pol. State M1
Co Pol. State M2
Co Pol. State M3
X Pol. Port 1x
X Pol. Port 2x
X Pol. Port 3x
X Pol. Port 4x
X Pol. State M1
X Pol. State M2
X Pol. State M3

(b)

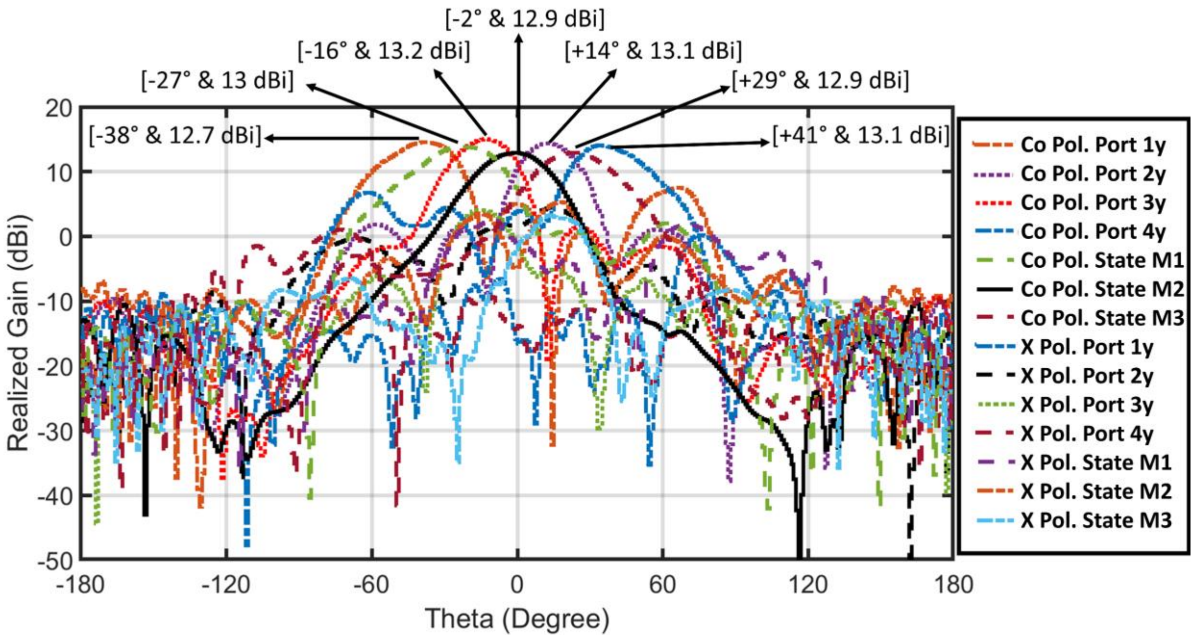

(c)

Figure 35. (a) Measured radiation patterns at 28 GHz for different type of excitation. (a) Both YoZ and XoZ cutting planes. (b) Radiation patterns at YoZ cutting plane. (c) Radiation patterns at XoZ cutting plane. States M1, M2, and M3 refer to combination of excitations.

Due to the limited size of the top roof of an electric vehicle, the main objective of the paper is to design a beam-forming system that can be fitted to the top roof in a compact form for vehicular applications. For vehicular applications, the proposed 2D beam-scanning system offers many advantages. Solar panels can be incorporated into the entire area surrounding the antenna's radiation aperture (BFN region) as one of the main advantages of the proposed structure. Solar panels could be placed in a more efficient manner on vehicles as a result of this advancement. The proposed beam-scanning antenna scans angles between -55 and +55 degrees, considering half-power beam widths in two orthogonal directions. With this proposed 2D beamforming system, the multipath fading phenomenon can be mitigated by directing the radiation beams in two orthogonal directions. The proposed system is a multifunctional system that creates a communication link between vehicles and the sky for short and medium range communications in vehicular applications.

5.3.4 Conclusion:

Nowadays, leader vehicular companies are developing an upcoming generation of electric vehicles (design concept). These smart vehicular are equipped with high efficiency solar panel systems covering their roof. This surface covered with solar panels can generate a stable power supply for moving cars, allowing them to store enough energy. An innovative study is proposed here, which aims to integrate an antenna propagation mechanism to the roof of the car in order to create a communication link with the sky. In such circumstance, signal propagation and solar energy harvesting should have minimal interaction in this link. On this note, a solar-powered multifunctional 2D beam-steering antenna system is discussed in detail. The proposed multifunctional system can be installed on top of vehicles to create short to medium range communication links toward required system directions, including artificial satellites, drones, helicopters, and highway RFID tags. This structure has an overall dimension of 160×160 mm2. There are sixteen solar cells located on the non-radiating surface of the proposed structure to generate 2.4 watts of energy. This architecture is capable of generating high-gain radiation patterns to cover a wide range of angles for an electronically controlled multifunctional unit. Sunlight energy harvesting, antenna propagation, beamforming, vehicular application, and communication toward the sky are among the multidisciplinary aspects of the structure. The operating frequency of the design is between 27 and 29.7 GHz, reflecting the new trends in communication. The proposed structure covers 110-degree antenna pattern redirection in two orthogonal axes with several isolated ports and an engineered feeding network.

5.4 *Millimeter-Wave Broadband Monopulse Radar Antenna for Space Debris Detection*

Authors: Farzad Karami, Halim Boutayeb, and Larbi Talbi.

[161]: IEEE Internet of Things Journal, Impact factor: 10.6

5.4.1 Abstract:

Monopulse radar systems are essential for managing space debris during satellite exploration missions due to its high precision, angular measurement capabilities, and ability to track multiple objects at once, ensuring the safety and integrity of space assets. In this paper, a compact mm-wave, end-fire, high gain monopulse antenna is presented that could be fabricated on a thin PCB laminate. The reported results show good performances, a −10-dB impedance bandwidth of 62.5% (22–42 GHz) for the sum and difference ports, better than 24 dB isolation between the input ports, the difference radiation patterns better than −18 dB null-depth. The proposed monopulse radar system could be used in a wide range of practical applications, including detecting and managing space debris on satellite exploration missions.

5.4.2 Introduction:

Today, over 6,000 artificial satellites are orbiting the Earth. The main application of these satellites in communication, weather forecasting systems, Global Positioning System (GPS), imaging systems, and satellite Internet access coverage [162]. Starlink is one of the most famous examples of these emerging services. Over 60 countries are covered by SpaceX's Starlink satellite internet constellation.

The constant launch of artificial satellites may result in a significant increase in space debris. Because of this, artificial satellites are increasingly at risk of collisions with space debris. Recently, European Space Agency announced that space debris is the most serious threat to future space exploration missions and satellite communications [163]. Space debris fragments that are several centimeters in length are particularly more harmful. They behave like a bullet that can destroy an entire satellite system in a moment. For the purpose of maintaining control and minimizing damage caused by space debris, smart systems are being developed to detect small fragments. Detection and monitoring of these fragments can be accomplished efficiently using conventional radar techniques.

Since the 1960s, one of the most widely used tracking systems has been the monopulse radar, which compares the amplitude and phase of the signals received through the sum and difference beams [164]. In monopulse radar systems, the sum configuration produces a radiation beam with low sidelobe levels, while the difference configuration generates a deep in the boresight direction. The sum beam is used to detect the target and the difference beam provides the angle. A monopulse radar system typically has a comparator feeding network and radiation component. A sum or difference mode is generated by the former, while a pattern diversity is managed by the latter. In traditional monopulse radar systems, monopulse comparators (e.g., rectangular waveguides [165] and reflectors and monopulse feeders [166]) are complicated and bulky, making assembly difficult and expensive.

In detection and tracking systems, such as monopulse radar systems that are carried by high-speed aircraft, missiles, and artificial satellites, end-fire radiation patterns are highly useful. In end-fire antennas, electromagnetic waves are propagated into free space along the direction of antenna extension. In these antennas, the main direction of radiated EM waves is parallel with the antenna structure. Therefore, it seems that end-fire antennas could exhibit better aerodynamic performance than broadside antennas in mentioned specific applications [167-168].

The aim of this section is to design a wideband mm-wave monopulse antenna based on a thin single-layer PCB laminate to produce the difference and sum patterns simultaneously. The comparator of the proposed mm-wave monopulse antenna system that is realized by rat race 180 made up of parallel traces on a very thin substrate. The scenario of the end-fire monopulse radar system for detecting space debris in satellite missions is shown in figure 36. As bringing in this scenario, the proposed radar system could be embedded on an orbiting satellite. The main challenge of this research was to design an mm-wave monopulse radar system with features of low profile, wide operating bandwidth, high isolation, and high-end-fire gain.

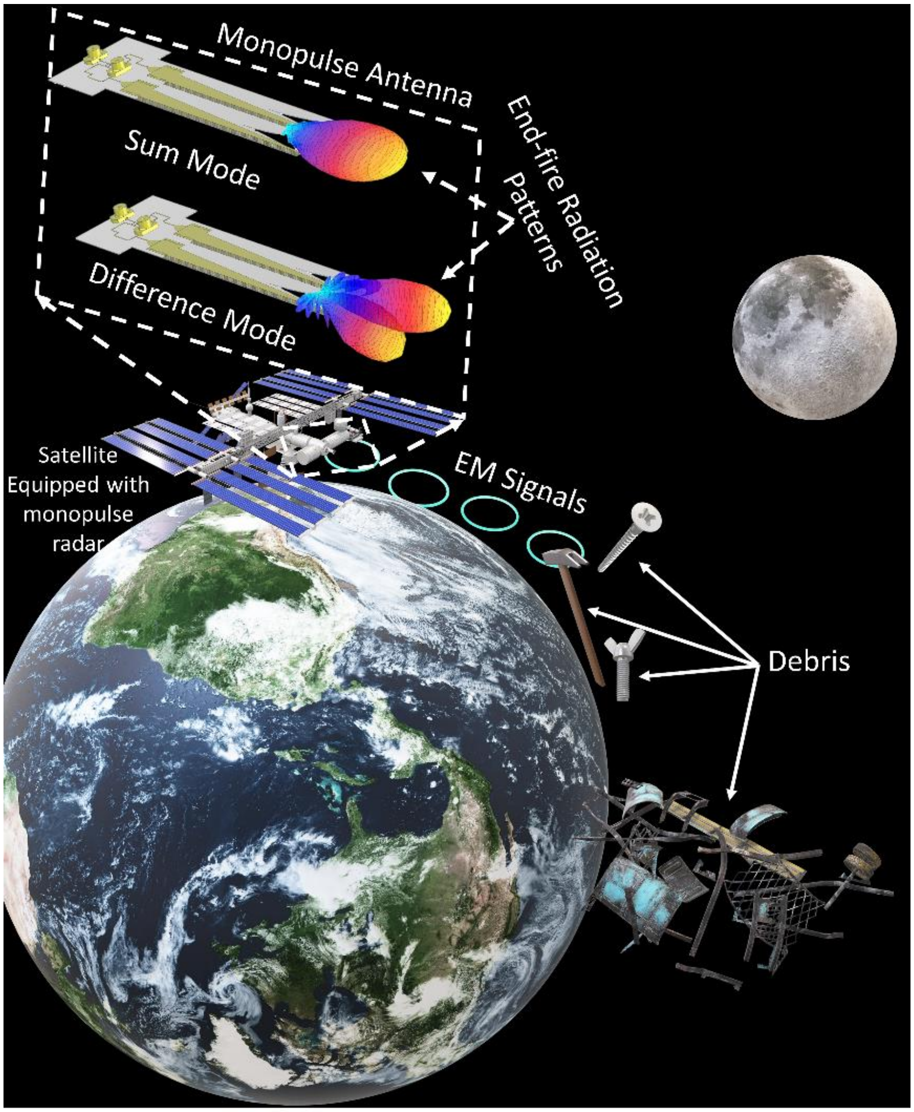

Figure 36. Illustration of the proposed end-fire monopulse antenna system for detecting space debris in satellite missions. The term space debris refers to any machinery or junk that humans have left behind during their space missions. It can refer to large objects, such as dead satellites that have failed or been left in orbit after their missions. As well, it can refer to paint flecks, debris, or other small fragments ejected from rockets.

5.4.3 Single-Layer Mm-Wave Monopulse Antenna Design

5.4.3.1 Comparator Network:

A circular line surrounded by three arms 90 degrees and one 270 degrees can form a rat race circuit. This kind of microwave hybrid 180-degree is the most appropriate device for providing phases 0 and 180 degrees in a comparator network. Rat races are extensively used in frequency amplifiers, mixers, balanced amplifiers, and push-pull amplifiers [169]. In spite of their outstanding features, they are generally less used in mm-wave applications that require a wide operating bandwidth [170].

Traditionally, a rat-race coupler has three $\frac{\lambda_g}{4}$ arms and one $\frac{3\lambda_g}{4}$ arm. Thus, a conventional rat-race coupler has an overall circumference of $1.5\lambda_g$. In the past, some miniaturization techniques have been introduced, such as folded lines, artificial lines, and synthetic meander lines, taking advantage of state-of-the-art fabrication technologies. It is possible to reduce the footprint of the rat-race coupler by 70% by implementing these strategies. These folders and meanders, however, add undesirable parasitic effects, that designers need to consider.

Other techniques for reducing the footprint of rat-race couplers is to use lumped elements. One of the major disadvantages of lumped elements is their parasitic effect beyond a particular frequency range. Other studies show that electromagnetic bandgaps (EBGs) structures and defected ground structures can be used to reduce size and suppress harmonics [171]. All these cases described above involved a reduction in size along with an increase in bandwidth. Nevertheless, the bandwidth improvement is limited, because they are based on structures that are frequency-dependent [172-173]. Ho et al. introduced an ideal 180 reverse-phase section which is independent of frequency, to achieve a wide bandwidth in [174]. Inverters of this type include CPW and slotline radial stubs for broadband impedance matching. Implementing these schemes, especially at mm-wave frequencies, seems complex. In the following, a mm-wave rat-race coupler based on parallel microstrip lines is presented for ka-band applications.

As shown in Fig. 37, a parallel transmission line is printed on both sides of a thin dielectric substrate. Transmission lines of this type are classified as balanced transmission lines. These double-sided lines have equal amplitudes and different phases, and electromagnetic waves flow between them. The proposed structure is shown in Figure 38. A dielectric substrate is covered with microstrip tracks on both sides. The lines are printed on a thin PCB laminate Ro 4350B, with a thickness of 0.17 mm.

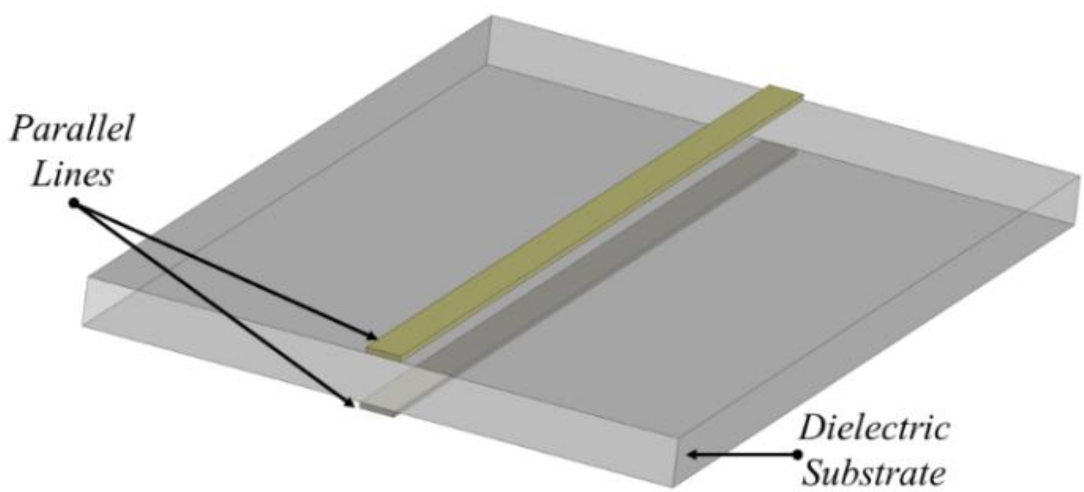

Figure 37. Parallel strip line printed on both side of a dielectric laminate.

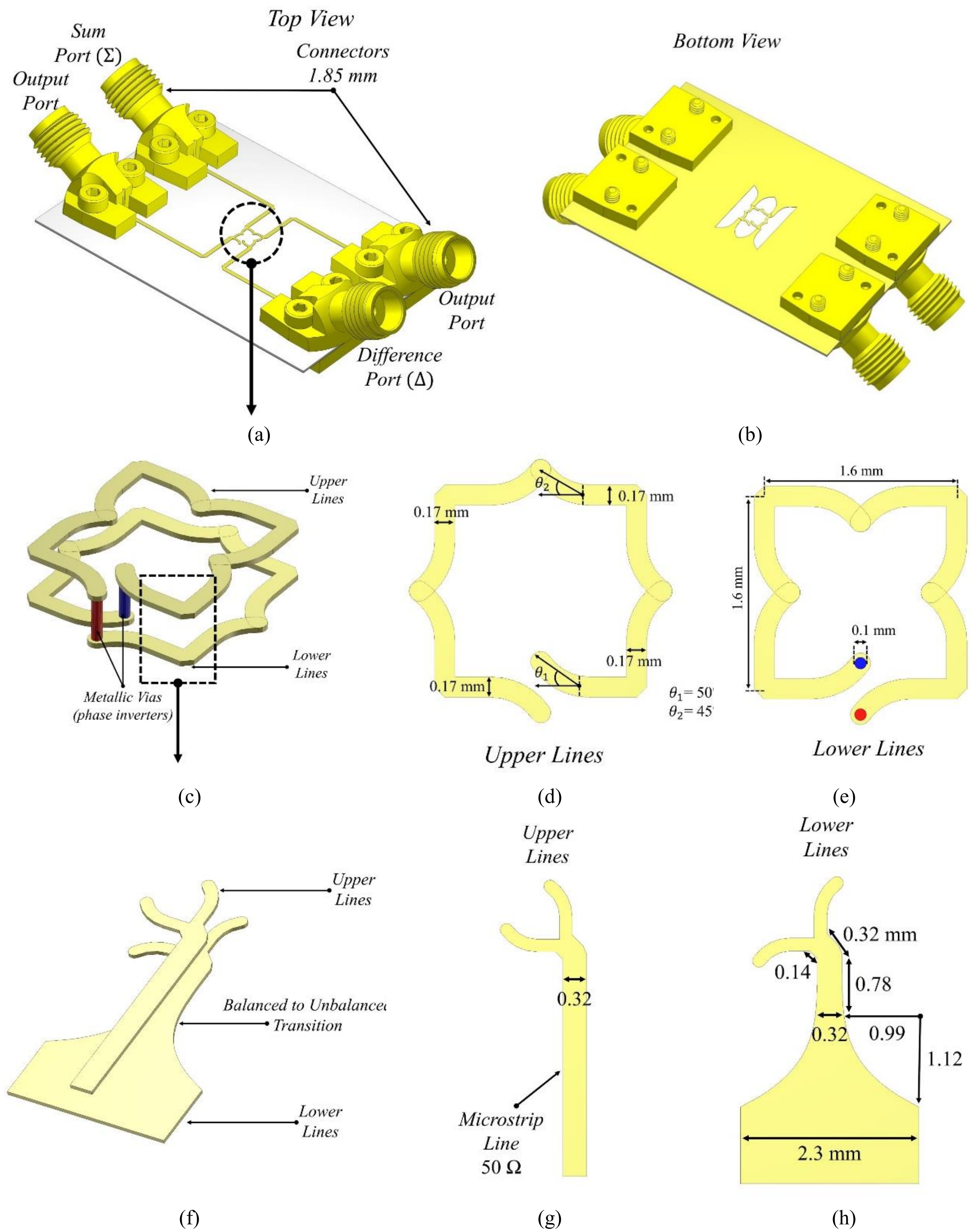

Figure 38. configuration of the proposed coupler. (a) Top view. (b) Bottom view. (c) 3-D perspective of the parallel arms. (d) Top view of the upper lines. (e) Top view of the bottom lines. (f) 3-D view of the proposed transition which connects microstrip lines 50-ohm to parallel tracks. (g) Top view of upper layer of transition. (h) Top view of bottom layer of transition.

In contrast to the conventional rat race, the proposed architecture has four arms that have 90 degrees electrical length. Two vias are placed in the middle of an arm to generate a 180-degree phase difference. Phase inversion is achieved by these cylindrical metallic vias in the proposed configuration.

5.4.3.2 Even-Odd Mode Analysis:

Figure 39(a) shows a schematic representation of the proposed architecture. A phase inverter and four arms form the main geometry of the proposed structure. The impedance of microstrip lines connecting arms to ports 1, 2, 3, and 4 is 50 ohms (0.32mm width). In parallel lines (arms), the impedance is √2×50 ohms (0.17 mm width). The following formulas can be used to calculate transmission line impedances in the proposed structure [175]:

$$Z_0 = \frac{120\pi}{2\sqrt{2}\pi\sqrt{\varepsilon_r+1}} \ln\left\{1 + \frac{4h}{W'}\left[\frac{14+8\varepsilon_{eff}}{11}\frac{4h}{w'} + \sqrt{\left(\frac{14+8\varepsilon_{eff}}{11}\right)^2\left(\frac{4h}{w'}\right)^2 + \frac{1+\frac{1}{\varepsilon_{eff}}}{2}\pi^2}\right]\right\} \quad (1)$$

where

$$W' = W + \Delta W' \quad (2)$$

$$\varepsilon_{eff} = \begin{cases} \frac{\varepsilon_R+1}{2} + \frac{\varepsilon_R-1}{2}\left[\frac{1}{\sqrt{1+12\left(\frac{H}{W}\right)}} + 0.04\left(1-\left(\frac{H}{W}\right)\right)^2\right] & \text{for } \left(\frac{H}{W}\right) < 1 \\ \frac{\varepsilon_R+1}{2} + \left[\frac{\varepsilon_R-1}{2\sqrt{1+12\left(\frac{H}{W}\right)}}\right] & \text{for } \left(\frac{H}{W}\right) > 1 \end{cases} \quad (3)$$

Using the even and odd modes technique, the proposed structure's performance can be evaluated in two steps. The first step involves using a signal with unit amplitude (A1=1) at port 1 (the sum port) of the coupler 180. The incident signal arrives at ports 2 and 3 with equal amplitude and phase and leaves port 4 with 180 degrees out of phase. As shown in figure 39(b), the proposed structure's equivalent circuit can be viewed in this state. Using the even-odd mode analysis technique, one can decompose this normalized circuit into a superposition of two simpler circuits and excitations as shown in Figure 39(c)-(f).

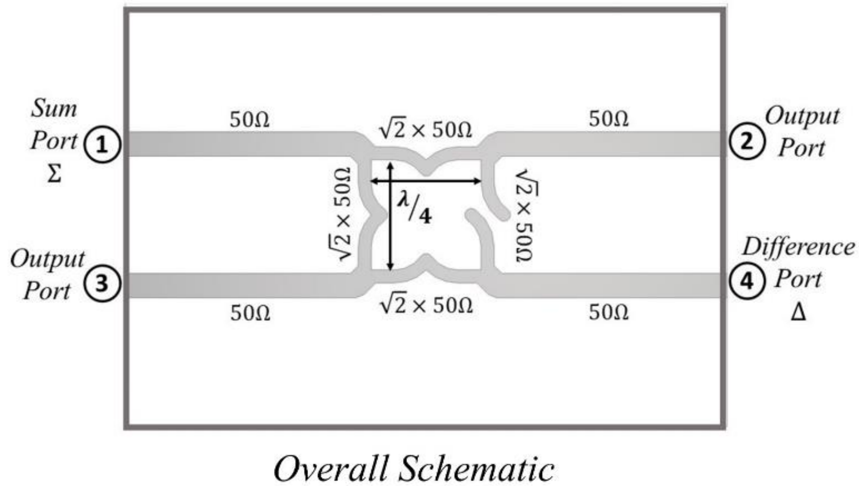
Sum Port ① Σ
50Ω
√2 × 50Ω
50Ω
② Output Port
√2 × 50Ω
λ/4
√2 × 50Ω
Output Port ③
Difference ④ Port Δ
50Ω
√2 × 50Ω
50Ω
Overall Schematic

(a)

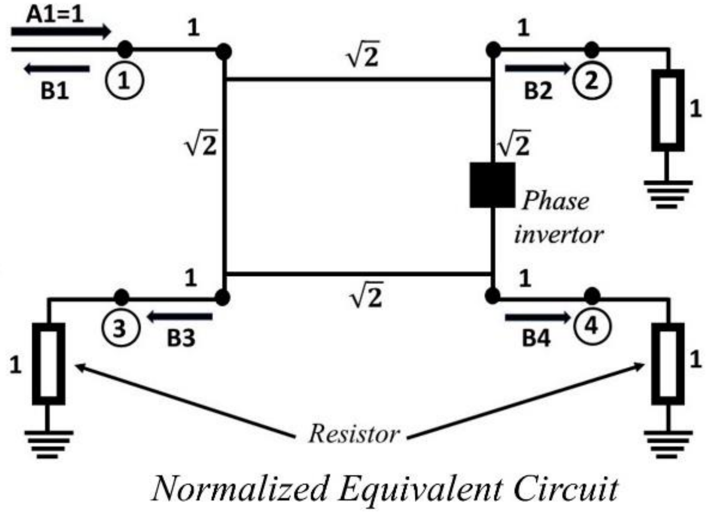
A1=1
B1
①
1
√2
1
B2
②
1
√2
√2
Phase invertor
1
√2
1
③
B3
B4
④
1
1
Resistor
Normalized Equivalent Circuit

(b)

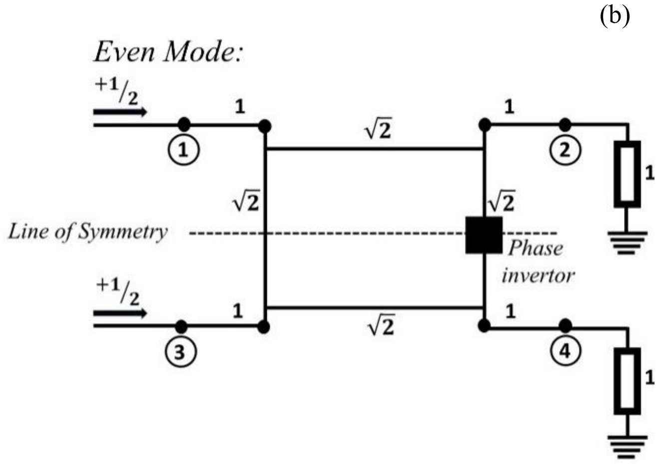
Even Mode:
+1/2
①
1
√2
1
②
1
√2
√2
Line of Symmetry
Phase invertor
+1/2
③
1
√2
1
④
1

(c)

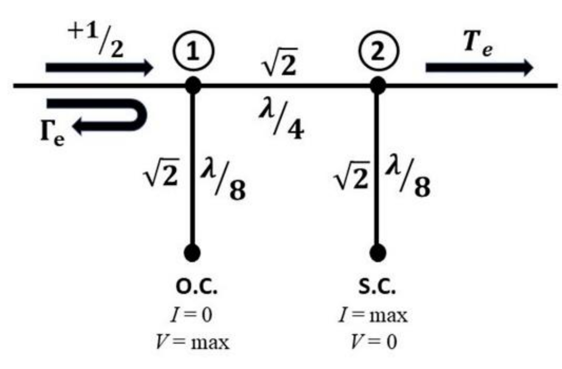
+1/2
①
√2
②
Te
Γe
λ/4
√2 λ/8
√2 λ/8
O.C.
I = 0
V = max
S.C.
I = max
V = 0

(d)

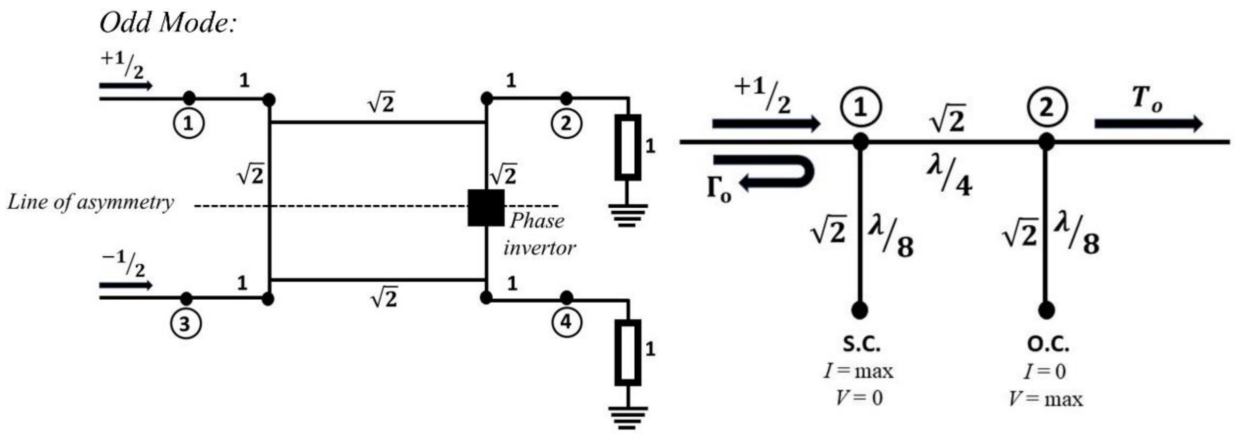

(e) (f)

Figure 39. Even and odd modes decomposition of the proposed rat race after the excitation of port 1 (Sum port) with a unit amplitude incident signal. (a) Overall schematic of the proposed hybrid coupler 180°. (b) Equivalent circuit of the rat race in normalized form when port 1 is excited. (c), (d) Even mode. (e), (f) Odd mode.

In the analytical process, it is assumed that vias have minimal reactance at the center frequency. So, their reactance effect can be ignored, and vias can be modelled as short circuits in such cases. Considering the scenario mentioned above, in the even mode of the half structure (Figure 39(d)), there are three sections: an open-circuit stub, a series transmission line, and a short-circuit stub. Thus, according to [175], the ABCD matrix for the even mode is as follows:

$$\begin{bmatrix} A & B \\ C & D \end{bmatrix}_e = \begin{bmatrix} Shunt \\ O.C. \\ Z_0 = \sqrt{2} \\ \frac{\lambda}{8} \end{bmatrix} \times \begin{bmatrix} Transmission \\ Line \\ Z_0 = \sqrt{2} \\ \frac{\lambda}{4} \end{bmatrix} \times \begin{bmatrix} Shunt \\ S.C. \\ Z_0 = \sqrt{2} \\ \frac{\lambda}{8} \end{bmatrix} \tag{4}$$

The ABCD parameters for a shunt could be determined through:

$$\begin{bmatrix} 1 & 0 \\ Y_{in} & 1 \end{bmatrix} \tag{5}$$

where

$$Y_{in} = \frac{1}{Z_{in}}, \tag{6}$$

$$Z_{in} = Z_o \frac{Z_L + jZ_0 \tan BL}{Z_0 + jZ_L \tan BL} \tag{7}$$

$$\begin{Bmatrix} For\ Short\ Circuits: Z_L = 0, Z_0 = \sqrt{2};\ Z_{in} = jZ_0 \tan BL \quad (8) \\ For\ Opern\ Circuits: Z_L = \infty, Z_0 = \sqrt{2};\ \ Z_{in} = -jZ_0 \cot BL \quad (9) \end{Bmatrix}$$

ABCD parameters for series transmission lines are as follows:

$$\begin{bmatrix} \cos BL & j\,Z_0 \sin BL \\ jY_0 \sin BL & \cos BL \end{bmatrix} \tag{10}$$

Consequently, the ABCD matrix for even mode of half structure shown in figure 3(d) is:

$$\begin{bmatrix} 1 & 0 \\ \frac{1}{-jZ_0 \cot BL} & 1 \end{bmatrix} \times \begin{bmatrix} \cos BL & j\,Z_0 \sin BL \\ jY_0 \sin BL & \cos BL \end{bmatrix} \times \begin{bmatrix} 1 & 0 \\ \frac{1}{jZ_0 \tan BL} & 1 \end{bmatrix} = \begin{bmatrix} 1 & 0 \\ \frac{1}{-j\sqrt{2}} & 1 \end{bmatrix} \times \begin{bmatrix} 0 & j\sqrt{2} \\ \frac{j}{\sqrt{2}} & 0 \end{bmatrix} \times$$

$$\begin{bmatrix} 1 & 0 \\ \frac{1}{j\sqrt{2}} & 1 \end{bmatrix} = \begin{bmatrix} 1 & j\sqrt{2} \\ j\sqrt{2} & -1 \end{bmatrix}$$

$$\begin{bmatrix} A & B \\ C & D \end{bmatrix}_e = \begin{bmatrix} 1 & j\sqrt{2} \\ j\sqrt{2} & -1 \end{bmatrix}$$

The odd mode of the half structure (figure 39(f)) consists of a short-circuit (S.C.) stub, a series transmission line, and an open-circuit (O.C.) stub. The ABCD matrix for the odd mode is as follows:

$$\begin{bmatrix} A & B \\ C & D \end{bmatrix}_O = \begin{bmatrix} Shunt \\ S.C. \\ Z_0 = \sqrt{2} \\ \frac{\lambda}{8} \end{bmatrix} \times \begin{bmatrix} Transmission \\ Line \\ Z_0 = \sqrt{2} \\ \frac{\lambda}{4} \end{bmatrix} \times \begin{bmatrix} Shunt \\ O.C. \\ Z_0 = \sqrt{2} \\ \frac{\lambda}{8} \end{bmatrix} \quad (11)$$

$$\begin{bmatrix} 1 & 0 \\ \frac{1}{jZ_0 \tan BL} & 1 \end{bmatrix} \times \begin{bmatrix} \cos BL & j\,Z_0 \sin BL \\ jY_0 \sin BL & \cos BL \end{bmatrix} \times \begin{bmatrix} 1 & 0 \\ \frac{1}{-jZ_0 \cot BL} & 1 \end{bmatrix} = \begin{bmatrix} 1 & 0 \\ \frac{1}{j\sqrt{2}} & 1 \end{bmatrix} \times \begin{bmatrix} 0 & j\sqrt{2} \\ \frac{j}{\sqrt{2}} & 0 \end{bmatrix} \times$$

$$\begin{bmatrix} 1 & 0 \\ \frac{J}{\sqrt{2}} & 1 \end{bmatrix} = \begin{bmatrix} -1 & j\sqrt{2} \\ j\sqrt{2} & 1 \end{bmatrix}$$

$$\begin{bmatrix} A & B \\ C & D \end{bmatrix}_O = \begin{bmatrix} -1 & j\sqrt{2} \\ j\sqrt{2} & 1 \end{bmatrix}$$

When the port sum is excited, the reflection coefficients and transmission coefficients can be calculated by even and odd ABCD matrices:

$$\Gamma_e = \frac{A+B-C-D}{A+B+C+D}, T_e = \frac{2}{A+B+C+D}, \Gamma_O = \frac{A+B-C-D}{A+B+C+D}, T_O = \frac{2}{A+B+C+D} \quad (12)$$

which leads to:

$$\Gamma_e = \frac{-j}{\sqrt{2}}, T_e = \frac{-j}{\sqrt{2}}, \Gamma_o = \frac{j}{\sqrt{2}}, T_o = \frac{-j}{\sqrt{2}}.$$

The amplitudes of the scattered waves from the proposed structure (refer to Fig. 39(b)) can also be obtained by:

$$B_1 = \frac{1}{2}\Gamma_e + \frac{1}{2}\Gamma_O = 0, \quad (13)$$

$$B_2 = \frac{1}{2}\mathrm{T}_e + \frac{1}{2}\mathrm{T}_O = \frac{-j}{\sqrt{2}}, \quad (14)$$

$$B_3 = \frac{1}{2}\Gamma_e - \frac{1}{2}\Gamma_O = \frac{-j}{\sqrt{2}}, \quad (15)$$

$$B_4 = \frac{1}{2}\mathrm{T}_e - \frac{1}{2}\mathrm{T}_O = 0, \quad (16)$$

Based on the results obtained in step 1, it is confirmed that input port 1 is matched (sum port), port 4 (difference port) is isolated, and the input signal is divided into ports 2 and 3 with equal amplitude and phase.

In the second step, a unitary amplitude signal (A1=1) is incident on port 4 (the difference port) of the proposed structure. In this state, two equal-amplitude but out-of-phase signals enter output ports 2 and 3. Figure 40(a) depicts the equivalent circuit of the proposed structure in this state. For this state, the same superposition is used both for the even and odd modes of analysis. According to Figure 40(b-e), this case can be decomposed into a superposition of two simple circuits and excitations.

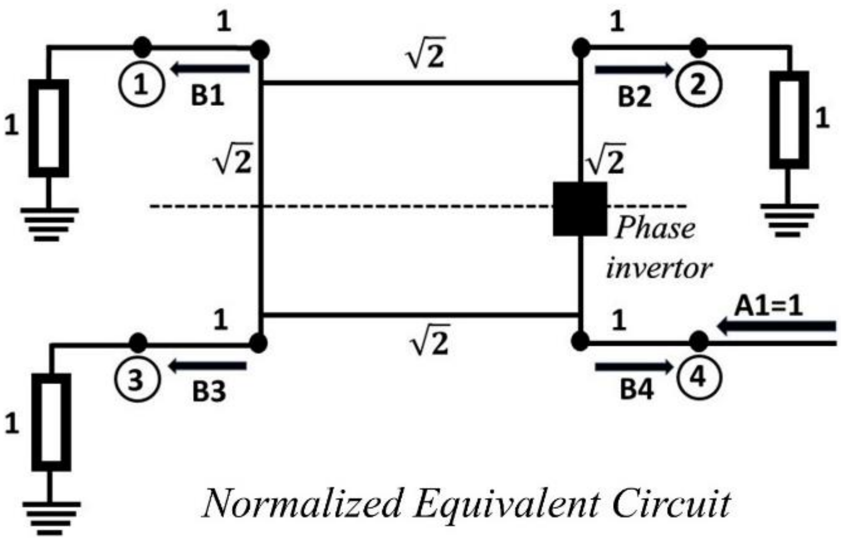

(a)

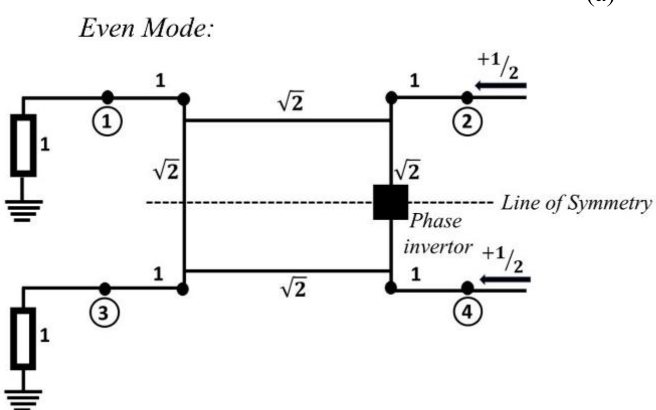

(b)

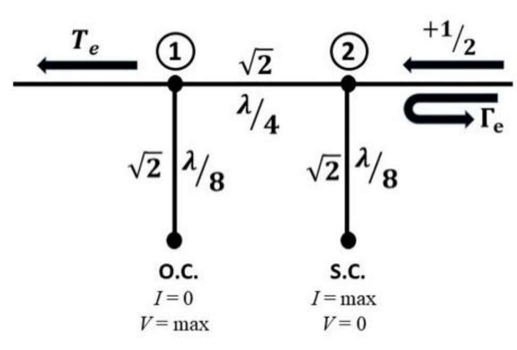

(c)

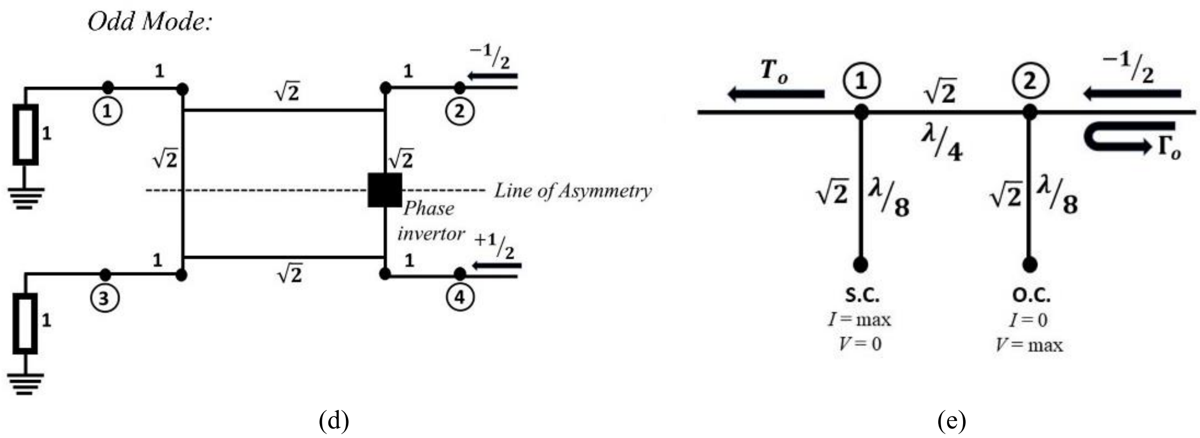

Figure 40. Even and odd modes decomposition of the proposed rat race after the excitation of port 4 (Difference port) with a unit amplitude incident signal. (a) Equivalent circuit of the rat race in normalized form when port 4 is excited. (b), (c) Even mode. (d), (e) Odd mode.

From left to right, there are three sections of the half structure in the even mode (figure 40(c)): a short-circuit stub, a series transmission line, and an open-circuit stub. For even mode, the ABCD matrix is as follows:

$$\begin{bmatrix} A & B \\ C & D \end{bmatrix}_e = \begin{bmatrix} Shunt \\ S.C. \\ Z_0 = \sqrt{2} \\ \frac{\lambda}{8} \end{bmatrix} \times \begin{bmatrix} Transmission \\ Line \\ Z_0 = \sqrt{2} \\ \frac{\lambda}{4} \end{bmatrix} \times \begin{bmatrix} Shunt \\ O.C. \\ Z_0 = \sqrt{2} \\ \frac{\lambda}{8} \end{bmatrix}, \quad (17)$$

According to relations (5)-(9):

$$\begin{bmatrix} 1 & 0 \\ \frac{1}{\frac{1}{j\,Z_0 \tan BL}} & 1 \end{bmatrix} \times \begin{bmatrix} \cos BL & j\,Z_0 \sin BL \\ jY_0 \sin BL & \cos BL \end{bmatrix} \times \begin{bmatrix} 1 & 0 \\ \frac{1}{\frac{1}{-jZ_0 \cot BL}} & 1 \end{bmatrix} = \begin{bmatrix} 1 & 0 \\ \frac{1}{j\sqrt{2}} & 1 \end{bmatrix} \times \begin{bmatrix} 0 & j\sqrt{2} \\ \frac{j}{\sqrt{2}} & 0 \end{bmatrix} \times \begin{bmatrix} 1 & 0 \\ \frac{J}{\sqrt{2}} & 1 \end{bmatrix} = \begin{bmatrix} -1 & j\sqrt{2} \\ j\sqrt{2} & 1 \end{bmatrix}$$

$$\begin{bmatrix} A & B \\ C & D \end{bmatrix}_e = \begin{bmatrix} -1 & j\sqrt{2} \\ j\sqrt{2} & 1 \end{bmatrix}$$

In the odd mode of half structure (figure 40(e)), from right to left, can be observed that there are an open-circuit (O.C.) stub, a series transmission line, and a short-circuit (S.C.) stub. For odd mode, the ABCD matrix is determined:

$$\begin{bmatrix} A & B \\ C & D \end{bmatrix}_O = \begin{bmatrix} Shunt \\ O.C. \\ Z_0 = \sqrt{2} \\ \frac{\lambda}{8} \end{bmatrix} \times \begin{bmatrix} Transmission \\ Line \\ Z_0 = \sqrt{2} \\ \frac{\lambda}{4} \end{bmatrix} \times \begin{bmatrix} Shunt \\ S.C. \\ Z_0 = \sqrt{2} \\ \frac{\lambda}{8} \end{bmatrix}, \quad (18)$$

According to relations (5)-(9):

$$\begin{bmatrix} 1 & 0 \\ \frac{1}{-jZ_0 \cot BL} & 1 \end{bmatrix} \times \begin{bmatrix} \cos BL & j\,Z_0 \sin BL \\ jY_0 \sin BL & \cos BL \end{bmatrix} \times \begin{bmatrix} 1 & 0 \\ \frac{1}{j\,Z_0 \tan BL} & 1 \end{bmatrix} = \begin{bmatrix} 1 & 0 \\ \frac{J}{\sqrt{2}} & 1 \end{bmatrix} \times \begin{bmatrix} 0 & j\sqrt{2} \\ \frac{j}{\sqrt{2}} & 0 \end{bmatrix} \times \begin{bmatrix} 1 & 0 \\ \frac{1}{j\sqrt{2}} & 1 \end{bmatrix} = \begin{bmatrix} 1 & j\sqrt{2} \\ j\sqrt{2} & -1 \end{bmatrix}$$

$$\begin{bmatrix} A & B \\ C & D \end{bmatrix}_o = \begin{bmatrix} 1 & j\sqrt{2} \\ j\sqrt{2} & -1 \end{bmatrix}$$

According to equation (12), the reflection and transmission coefficients can be calculated by obtaining ABCD matrices for even and odd modes when the port difference is excited:

$$\Gamma_e = \frac{j}{\sqrt{2}}$$

$$T_e = \frac{-j}{\sqrt{2}}$$

$$\Gamma_o = \frac{-j}{\sqrt{2}}$$

$$T_o = \frac{-j}{\sqrt{2}}$$

Also, the amplitudes of the scattered waves from the proposed structure in figure 40(a) can be obtained by relations (19-22):

$$B_1 = \frac{1}{2}\mathrm{T}_e - \frac{1}{2}\mathrm{T}_O = 0, \ (19)$$

$$B_2 = \frac{1}{2}\Gamma_e - \frac{1}{2}\Gamma_O = \frac{j}{\sqrt{2}}, \ (20)$$

$$B_3 = \frac{1}{2}\mathrm{T}_e + \frac{1}{2}\mathrm{T}_O = \frac{-j}{\sqrt{2}}, \ (21)$$

$$B_4 = \frac{1}{2}\Gamma_e + \frac{1}{2}\Gamma_O = 0, \ (22)$$

As a result of step 2, it could be concluded that input port 4 is matched (Difference port), port 1 is isolated, and the input signal to difference port is divided evenly between ports 2, and 3.

5.4.3.3 Numerical Results:

This section describes how the proposed structure is designed using the full-wave software, CST Microwave Studio. Figure 38(a) shows that the proposed coupler has two input ports: sum and difference (ports 1 and 4), and two output ports: 2 and 3. In the proposed configuration, four 50-ohm microstrip lines are connected to parallel traces through a balanced to unbalanced transition (Balun). In the following, microstrip lines are connected to 50-ohm 1.85 connectors.

A simulation of scattering parameters as well as a phase performance analysis of the proposed coupler 180° are depicted in figures 39 and 40. Using figure 41, it can be seen that after the excitation of the sum port, the input signal is divided into input and output ports with the same amplitude and phase. Here, S_{11}, S_{14}, S_{12}, and S_{13} represent the reflection coefficient, the isolation between the sum and difference ports, the transmission coefficient from input 1 to output 2, and the transmission coefficient from input 1 to output 3, respectively.

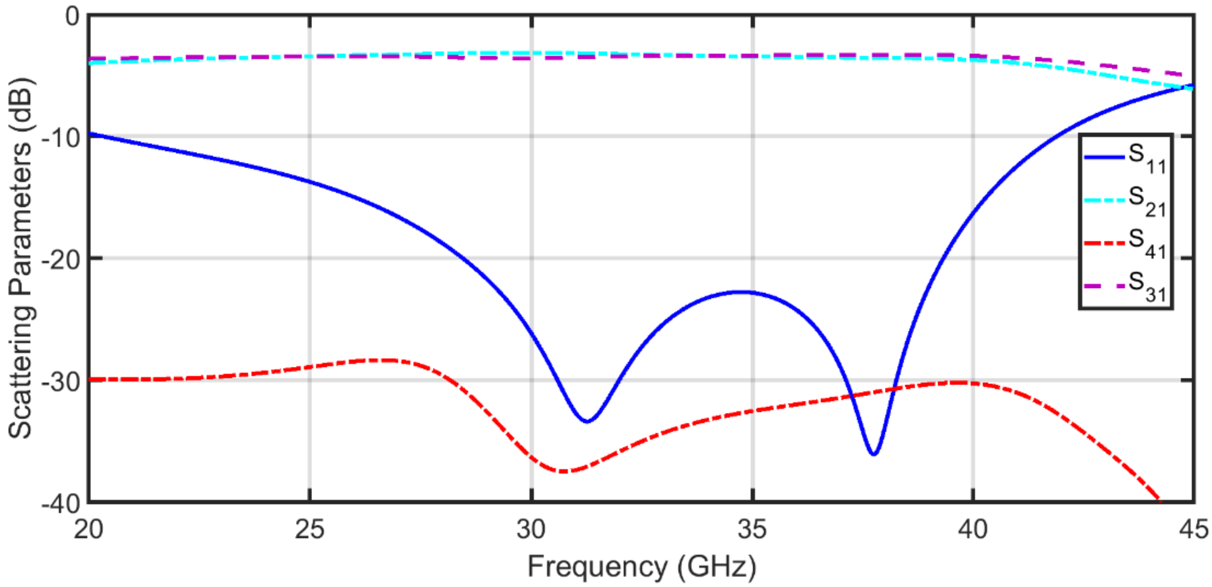

(a)

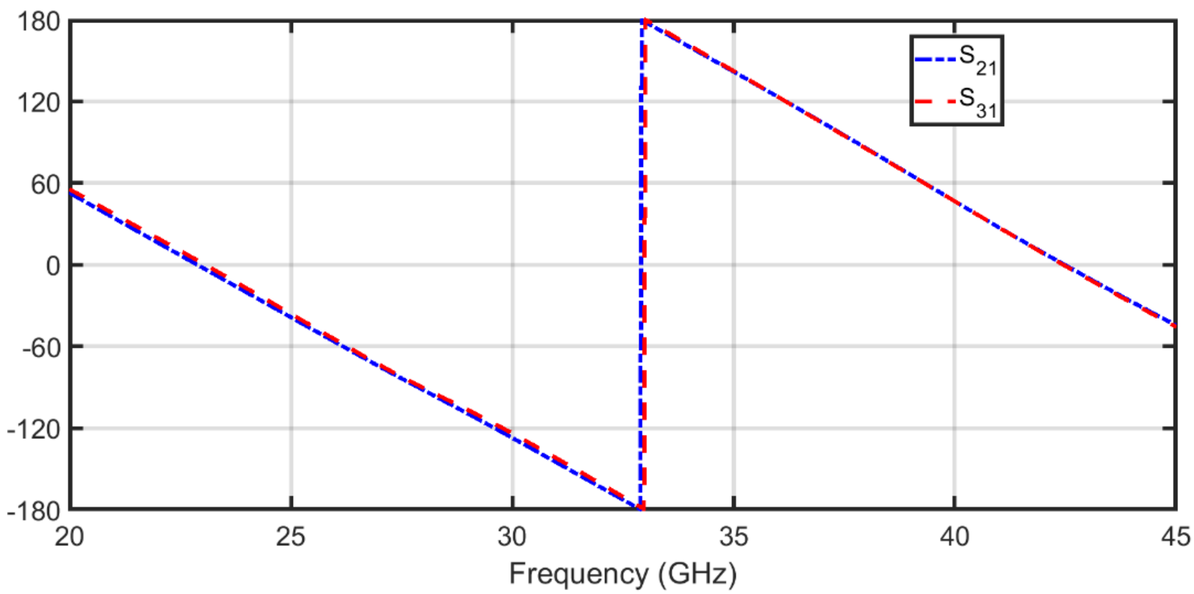

(b)

Figure 41. Simulated results of scattering parameters and phase difference of the proposed rat race by excitation of Sum port (Port 1).

According to the simulated results, the sum port will cover an impedance bandwidth of -10 dB in the frequency range of 20–42 GHz, while the isolation between the sum and difference ports will be much greater than 28 dB in the entire operating bandwidth.

As a result of the excitation of the difference port, two signals with the same amplitude but out of phase flow to the output ports. The S44, S41, S42, and S43 are the reflection coefficients, the isolation between the sum and difference ports, the transmission coefficient between input 4 and output 2, and the transmission coefficient between input 1 and output 3, respectively. Figure 42 shows that a difference port operates between 20-42 GHz (-10 dB) while the isolation between input ports is much greater than a 28 dB. It is clear that the difference port operates within a spectrum from 20-42 GHz.

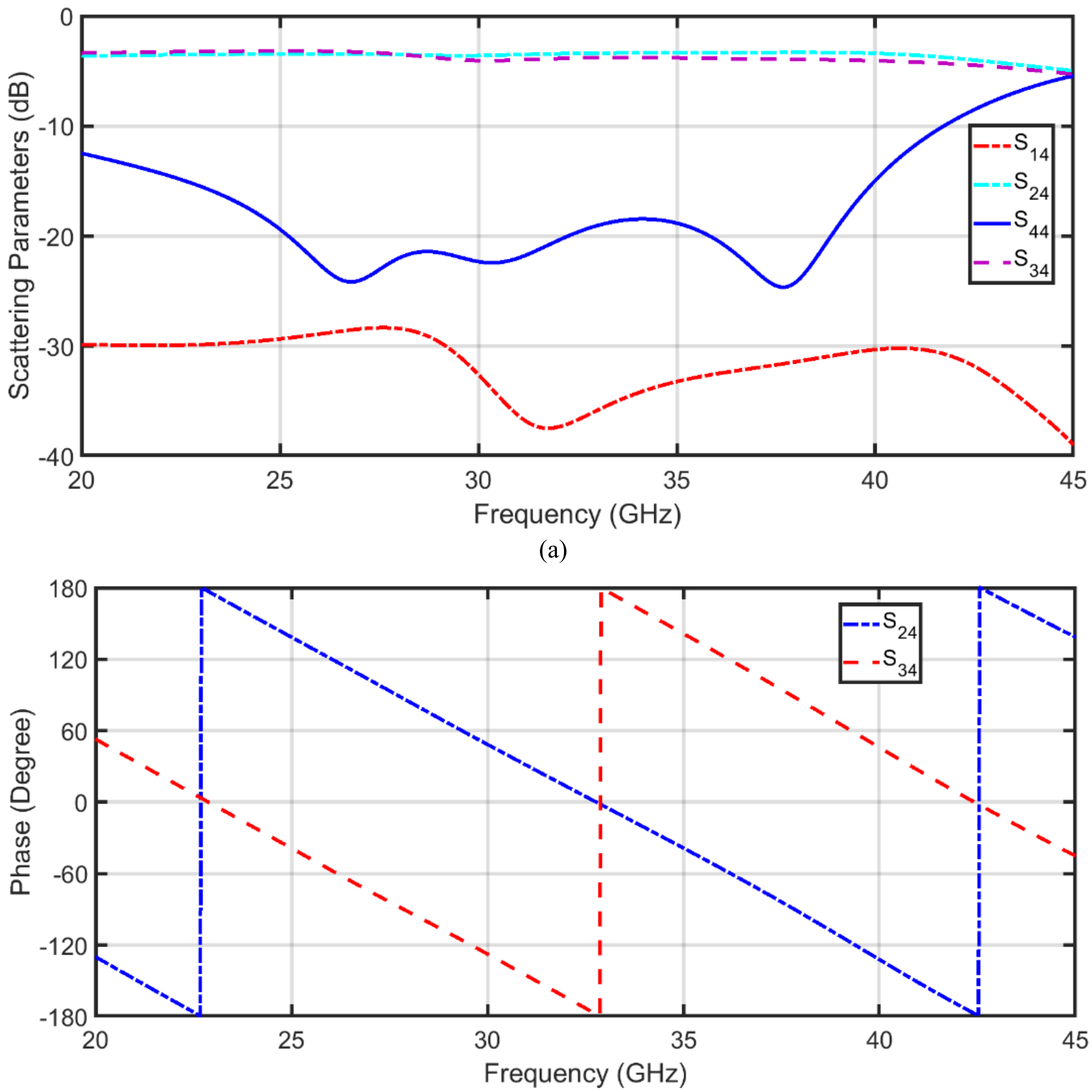

(b)

Figure 42. Simulated results of scattering parameters and phase difference of the proposed rat race by excitation of difference port (Port 4).

5.4.4 Monopulse Antenna:

Figure 43 illustrates the general configuration and dimensions of the proposed mm-wave monopulse antenna. It consists of a comparator network and a pair of tapered slot antennas. In all cases, dimensions are reported in millimeters. There are many benefits to tapered slot antennas, including simplicity, ease of fabrication, end-fire radiation pattern, high gain, low fabrication cost, and high gain [176]. Depending on the antenna type, the slot tapers may take various shapes, such as exponentially, linearly, or broken linearly. These antennas are designed according to these guidelines. The tapered slot has an opening width that is at least equal to or even larger than.

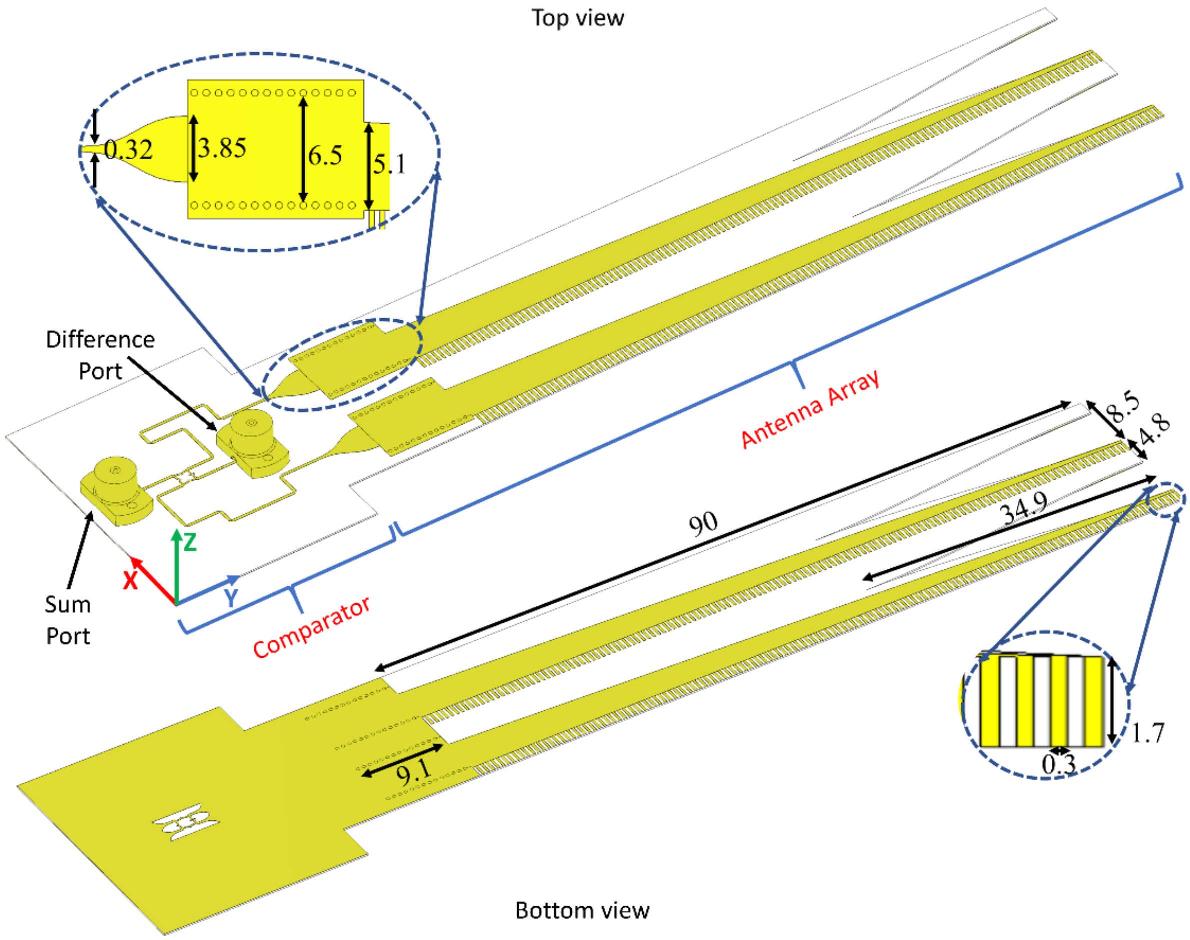

Figure 43. Top and bottom views of the proposed single-layer monopulse antenna.

The slot opening has the following effective width:

$$0.005 < \frac{t_{eff}}{\lambda_0} < 0.03, \text{ and } t_{eff} = (\sqrt{\varepsilon_r} - 1) \times h \ (23)$$

In this equation, h (=0.17 mm), and and $\varepsilon_r (= 3.48)$ represent the dielectric thickness and permittivity, respectively. Additionally, the antenna length can be selected between $3\lambda_0$ and $8\lambda_0$. In Figure 41, the tapered slot antenna is illustrated with corrugated shapes printed on its edges. [177] reports that these corrugations lead to a positive effect on reflection coefficients, gains, and cross-polarization levels. Tapered taper slot antennas can be excited by a variety of transitions, including multilayer microstrip lines, strip lines, and grounded coplanar waveguides. The proposed tapered slot antenna is fed by a microstrip-to-SIW tapered transition. With this transition, an effective impedance match could be achieved. For a single element of the proposed tapered slot antenna, Figure 8 shows the simulated return loss and the realized gain. As shown in figure 44, the simulated return loss of this antenna covers a frequency bandwidth of 20–45 GHz. According to the simulated results, the antenna's gain varies between 11-14 dBi over the entire operating bandwidth. In this kind of antenna, the antenna gain is independent of the aperture size.

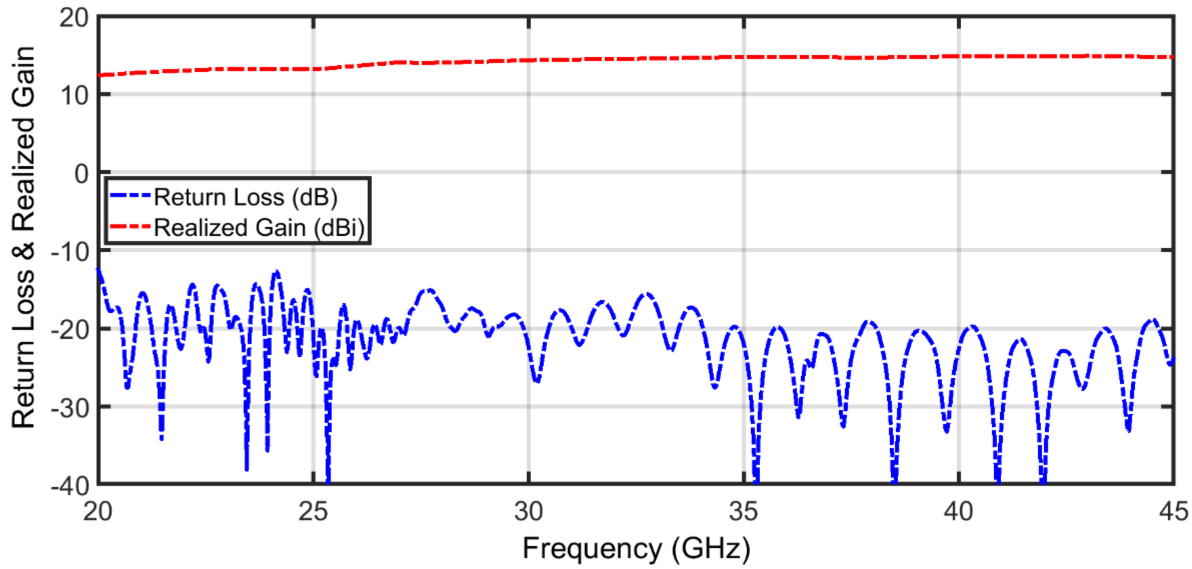

Figure 44. Simulated return loss and realized gain of a single element tapered slot antenna.

Figure 43 shows multiple views of the proposed monopulse radar system. Two vertical connectors are presented in this architecture: sum and difference ports. A "sum" radiation pattern is formed by the in-phase current distribution generated by the Sum port, while a "difference" radiation pattern is formed by the out-of-phase current distribution generated by the Difference port. Figure 45 shows the simulated scattering parameters and realized gain for the proposed design.

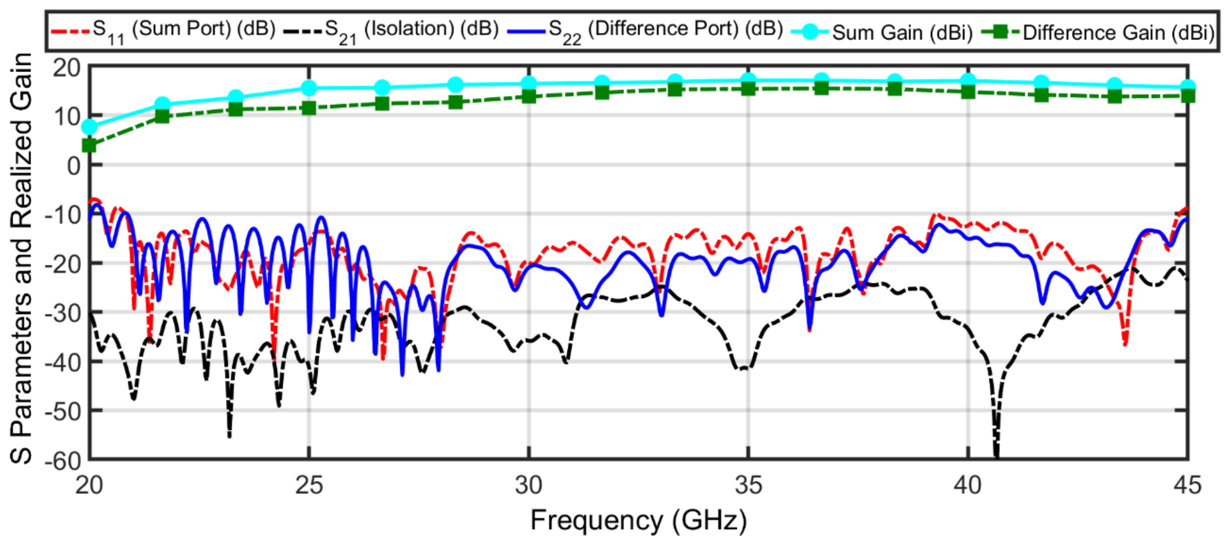

Figure 45. Simulated scattering parameters and realized gain of the proposed mm-wave monopulse antenna for sum and difference states.

Using the results from the simulation, the simulated fractional impedance bandwidth is 72.7% and corresponds to the frequency range between 21 GHz and 45 GHz. Also, the results show that the sum and difference ports are isolated by more than 20 dB over the full frequency range.

Furthermore, Fig. 45 shows the simulated realized gains for the "Sum Port" and "Difference Port". The maximum value of gain for sum and difference ports are 16.5 dBi and 9.5–14.2 dBi, respectively. In Figure 46, two-dimensional radiation patterns at frequency points 21, 33, and 45 GHz are shown. In the entire operating bandwidth, it seems that the simulated null-depth ranges from -25 to -35 dB. The cross-polarization levels at the boresight direction are also less than 15 dB for sum patterns.

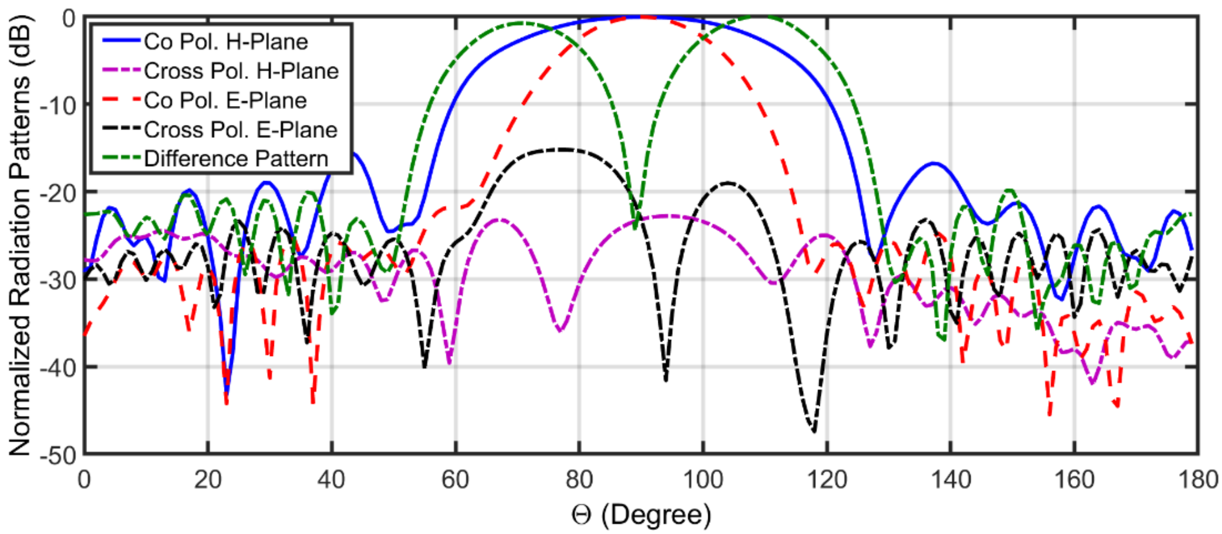

(a)

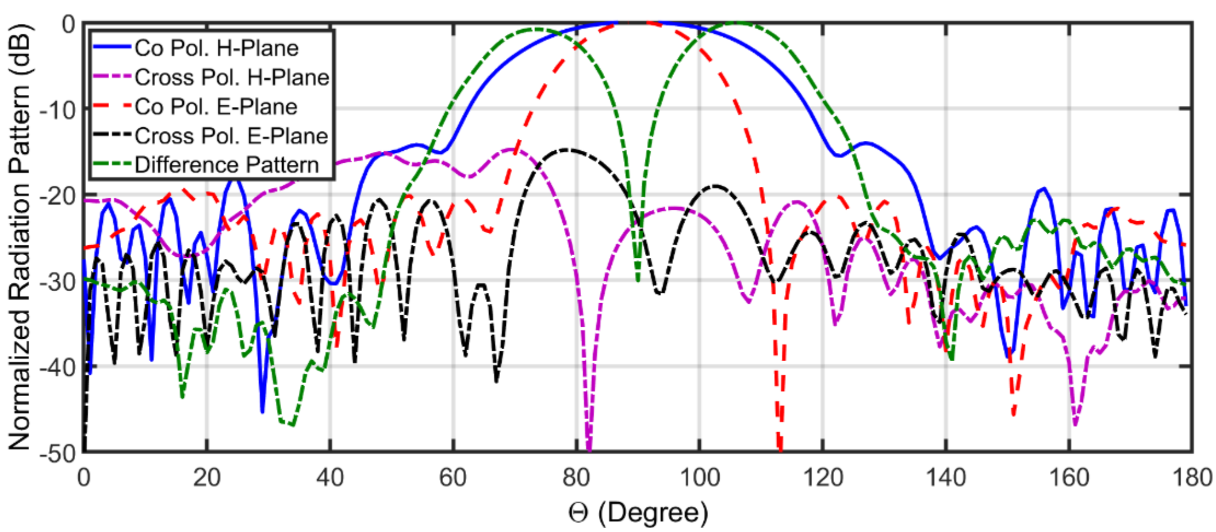

(b)

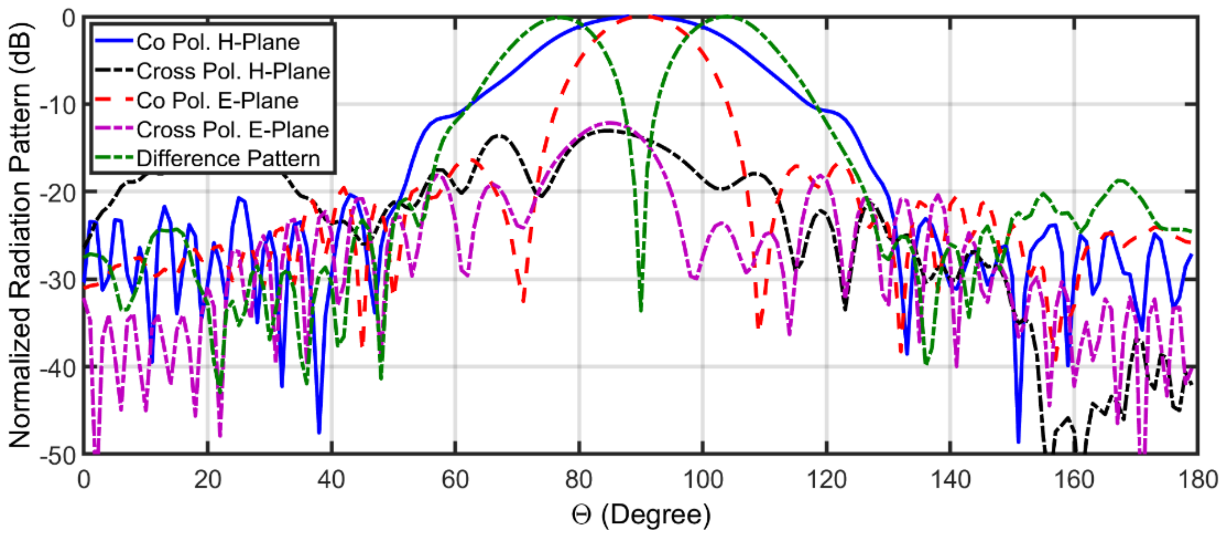

(c)

Figure 46. Simulated normalized radiation patterns of the proposed mm-wave monopulse antenna for sum and difference states. (a) 21 GHz, (b) 33 GHz, and (c) 45 GHz.

5.4.5 Experimental Results and Performance:

5.4.5.1 Antenna Characteristics:

To validate the proposed concept, a prototype of the end-fire mm-wave monopulse antenna system was fabricated and measured. A photograph of the fabricated monopulse antenna system is illustrated in Fig. 47(a). The measured impedance bandwidth for sum and difference ports is shown in Fig. 47(b). According to this figure, the proposed monopulse antenna covers a frequency range of 22-42 GHz, which corresponds to an operating bandwidth of 62.5%. Moreover, the end-fire sum and difference radiation patterns of the proposed monopulse antenna system were measured and depicted at 22, 33, and 42 GHz in an anechoic chamber. The monopulse antenna under test within the anechoic chamber can be seen in Fig. 47(c). The measured sum and difference radiation patterns at frequencies of 22, 33, and 42 GHz are shown in Fig. 47(d). The main beam direction of the measured radiation patterns is observed along the antenna direction. According to measurement results, the null-depth varies from -18 to -37 dB in the entire operating bandwidth. Sum patterns also exhibit cross-polarization levels less than 15 dB in the boresight direction.

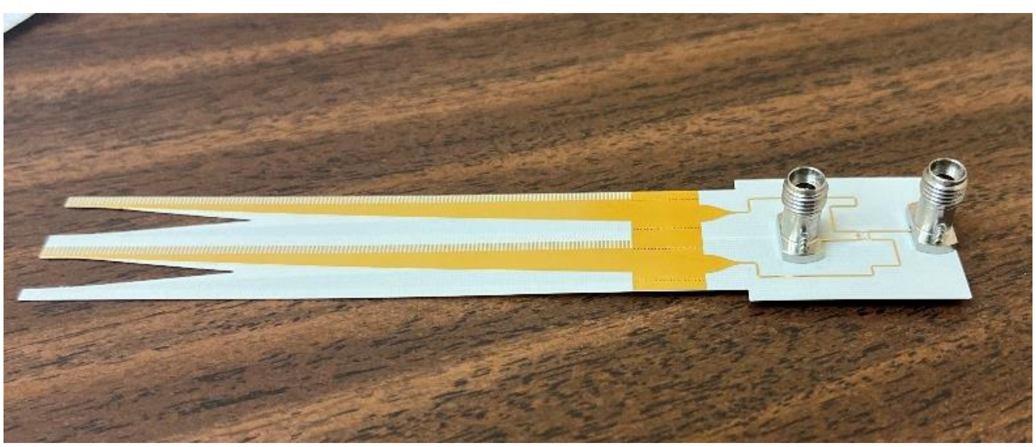

(a)

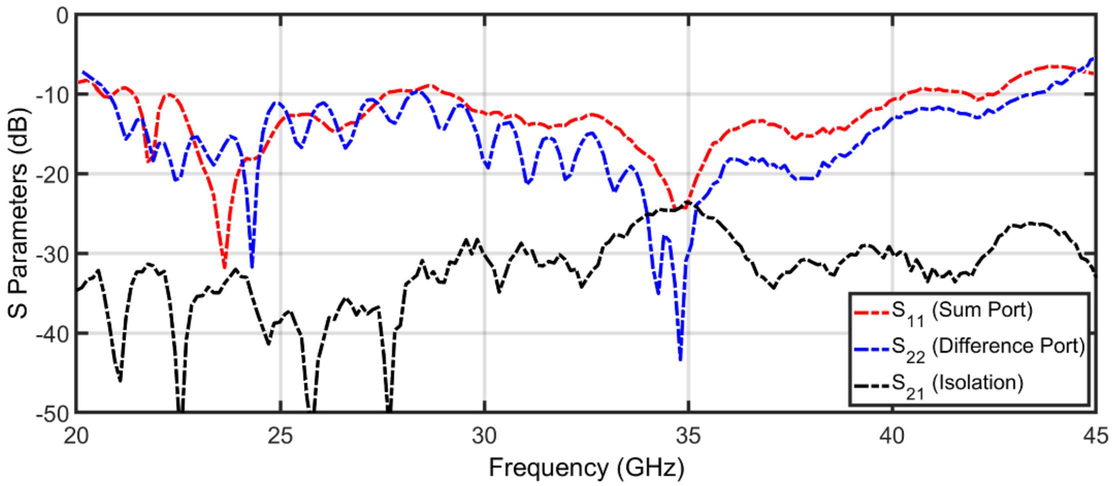
S Parameters (dB)
Frequency (GHz)
S_{11} (Sum Port)
S_{22} (Difference Port)
S_{21} (Isolation)

(b)

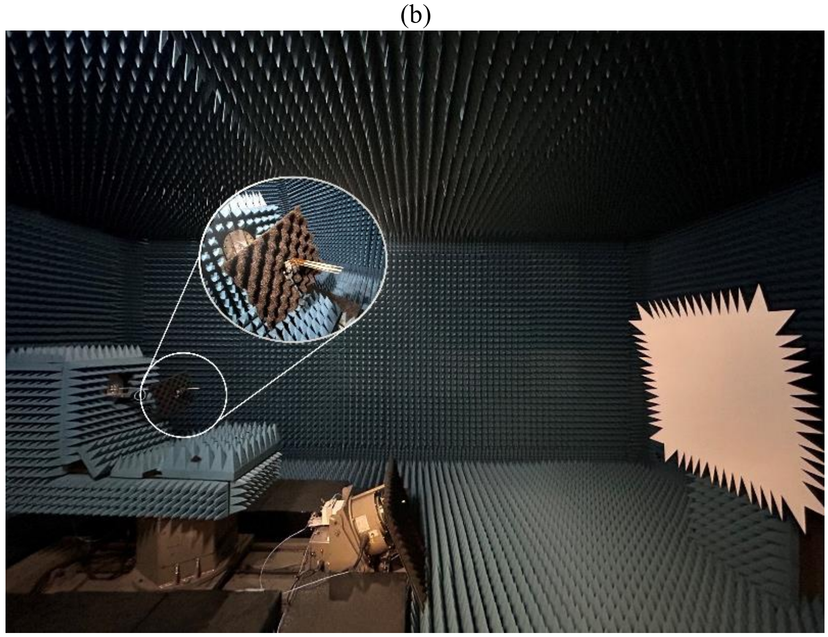

(c)

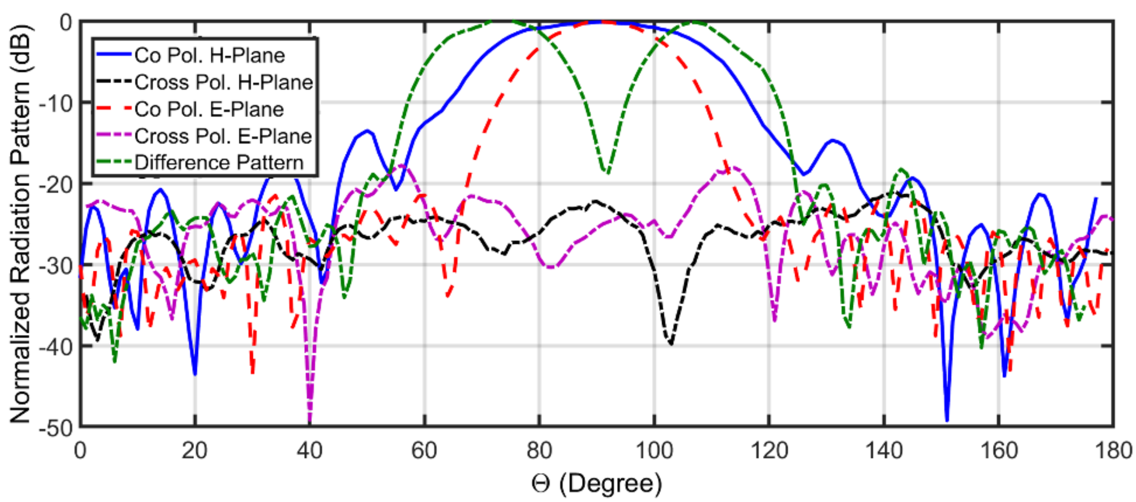
Normalized Radiation Pattern (dB)
Θ (Degree)
Co Pol. H-Plane
Cross Pol. H-Plane
Co Pol. E-Plane
Cross Pol. E-Plane
Difference Pattern

(d)

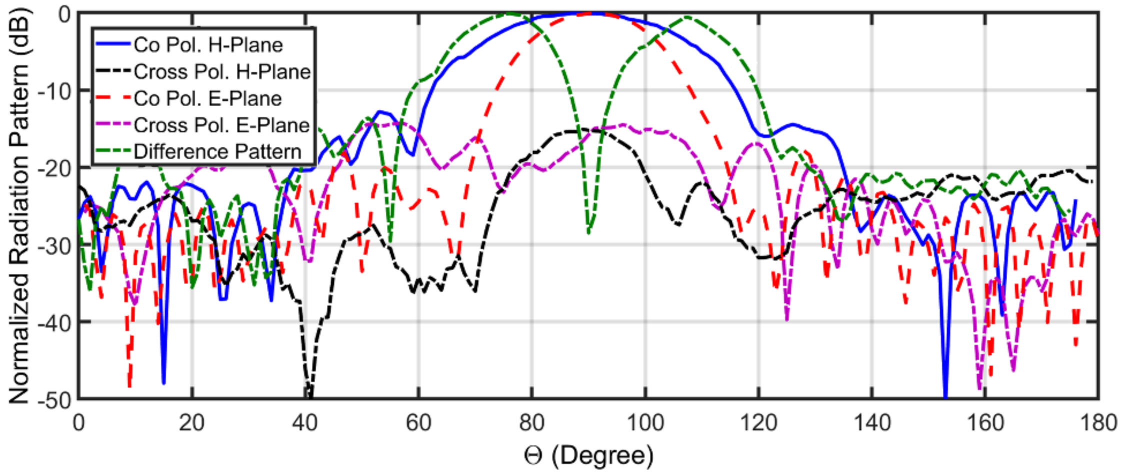

(e)

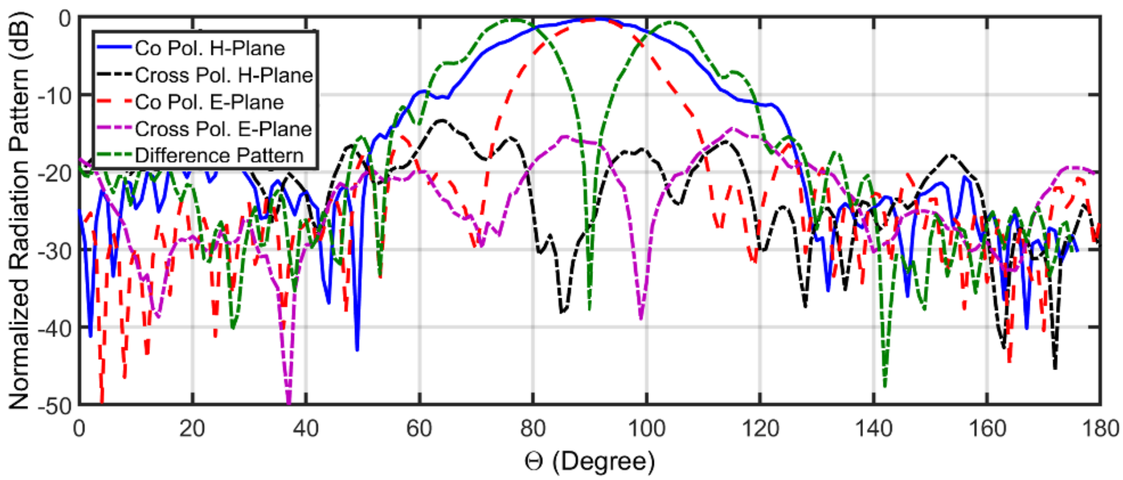

(f)

Figure 47. Configuration of the proposed mm-wave monopulse antenna system: (a) Photograph of the fabricated prototype. (b) Measured S parameters. (c) Photograph of the antenna under test in the anechoic chamber. (d) Measured radiation patterns at frequencies 22, 33, and 42 GHz.

5.4.5.2 Comparison and Discussion:

The proliferation of artificial satellites, numbering over 6,000, has revolutionized communication, weather forecasting, navigation, and various other critical functions. However, this advancement comes with a significant concern: the escalating threat of space debris. The constant launch of satellites has led to a surge in space debris, posing an imminent risk of collision with operational satellites. In addition to jeopardizing the billions invested in satellite technology, such collisions might also have broader implications. In response to this urgent challenge, the development of smart systems for satellite installation aimed at detecting and mitigating the impact of space debris is underway. Radar techniques could be a promising avenue for efficiently detecting and monitoring space debris fragments. By leveraging radar technology, satellite operators can enhance their capabilities to track and anticipate potential collisions, thus safeguarding critical satellite infrastructure. Among radar techniques, monopulse radar systems could be an appropriate option to use in satellite missions to detect space debris. Table 5 compares the characteristics and performances of the proposed monopulse antenna system with those of other antennas from the literature.

Table 5**.** Comparison between the proposed antenna and state-of-the-art.

Reference		[78]	[79]	[169]	This work
Technology		Gap Waveguide	Stacked PCB	Multi-layer PCB	Single PCB
Number of Layer		2	2	4	1
Antenna Type		Radial line slot array	Patch array	Patch array	Tapered slot
Size	Length	150	55	100	120
	Width	60	50	93.9	30
	Thickness	7.8	1.3	3.3	0.17
Bandwidth (%) @ Central frequency		0.83% @ 94 GHz	2.1% @ 10 GHz	13.45% @ 10 GHz	62.5% @ 32 GHz
Peak Gain (dBi)		27.8	12.5	16	14.2
Isolation (dB)		20	25	> 30	> 25
Max. Null-depth (dB)		50	-24	< -38	-37
Radiation Pattern Type		Broadside	Broadside	Broadside	End-fire

A millimeter-wave monopulse radial line slot array antenna is proposed in [78]. While this antenna offers good radiation performance, its narrow operating bandwidth can limit its practical use. Furthermore, it appears that this structure is bulky and extensive. In [79], another monopulse antenna was described for X-band applications, but its operating frequency bandwidth was relatively small. A multi-layer SIW monopulse antenna with a 13.45% operational bandwidth is described in [169]. At higher frequencies, this structure requires a complex fabrication process, and its fabrication is very challenging.

The proposed monopulse antenna is compact, low-cost, and presents good performance in terms of size, operating bandwidth, gain, isolation, and radiation performance. It does not require a complex and high-cost comparator. The overall size of the proposed system is 120×30×0.17 mm^3. It covers 20 GHz bandwidth for both sum and difference modes. Directive end-fire radiation patterns are obtained, with a low sidelobe level and a low front-to-back ratio. The proposed monopulse antenna exhibits a great aerodynamic condition compared with broadside monopulse antennas.

6 CONCLUSION

This thesis has presented a series of novel designs addressing key challenges in microwave and millimeter-wave communication systems, with a particular focus on satellite communications, high-speed railway networks, and vehicular-to-satellite applications. Through innovative diplexing, beamforming, and monopulse radar antenna technologies, this research has contributed to advancing the state of the art in high-frequency wireless systems.

The first contribution of this work was the development of a compact Ku-band diplexing structure and a directive end-fire antenna, optimized for high-speed railway communication. The proposed design successfully demonstrated improved isolation, reduced interference, and enhanced performance for future high-speed train networks.

The second major contribution was the design of a multifunctional switched-beam antenna system integrated with solar panels, aimed at vehicular-to-satellite communication. This system significantly improved scanning coverage and channel capacity while integrating sustainable energy solutions, offering a promising approach for intelligent transportation and next-generation connectivity.

Finally, this research introduced a broadband millimeter-wave rat-race coupler and its application in a monopulse radar antenna system for space debris detection. The proposed system, operating in the 20–42 GHz range, provides high-resolution tracking capabilities for satellite missions, contributing to the growing need for space situational awareness.

These contributions not only address the specific challenges outlined in this thesis but also pave the way for future advancements in microwave and millimeter-wave systems. As emerging wireless applications demand higher data rates, improved efficiency, and compact designs, the methodologies developed in this research can serve as a foundation for next-generation communication and radar technologies. Future research can build upon these findings by exploring further miniaturization, integration with reconfigurable intelligent surfaces, and enhanced adaptive beamforming techniques to meet the evolving demands of wireless and satellite communication.

PUBLICATIONS

Journal Papers:

1. F. Karami, H. Boutayeb, A. Amn-e-Elahi, L. Talbi, and A. Ghayekhloo. "Analysis and Design of a Diplexing Power Divider for Ku-Band Satellite Applications." *Sensors* 23, no. 21 (2023): 8726.

2. F. Karami, H. Boutayeb and L. Talbi, "Directive Millimeter-wave End-Fire Diplexing Antenna for IoT Applications," *IEEE Internet of Things Journal*, vol. 10, no. 22, pp. 19874-19882, Nov. 2023.

3. F. Karami, H. Boutayeb, L. Talbi, K. Hettak and A. Ghayekhloo, "Multifunctional Switched-Beam Antenna Located on Solar Cell for Vehicular to Satellite Communication," IEEE Transactions on Vehicular Technology, vol. 73, no. 3, pp. 3457-3468, March 2024, doi: 10.1109/TVT.2023.3323419.

4. F. Karami, H. Boutayeb and L. Talbi, "Millimeter-Wave Broadband Monopulse Radar Antenna for Space Debris Detection," IEEE Internet of Things Journal, vol. 11, no. 18, pp. 30376-30384, 15 Sept.15, 2024, doi: 10.1109/JIOT.2024.3411040.

Conference Papers:

5. F. Karami, A. Amn-e-Elahi, H. Boutayeb, F. Hyjazie and L. Talbi, "A Ku-Band SIW Diplexer-Power divider," *IEEE International Symposium on Antennas and Propagation and USNC-URSI Radio Science Meeting* (AP-S/URSI), Denver, CO, USA, 2022, pp. 2032-2033,
6. F. Karami, H. Boutayeb and L. Talbi, "IoT-based Transceiver Antenna System for 5G Future High-Speed Train Communications," *17th European Conference on Antennas and Propagation* (EuCAP), Florence, Italy, 2023, pp. 1-3.
7. F. Karami, H. Boutayeb, A. Amn-e-Elahi and L. Talbi, "Compact Broadband Rat-Race Coupler for Millimiter-Wave Applications," *IEEE International Symposium on Antennas and Propagation and USNC-URSI Radio Science Meeting* (USNC-URSI), Portland, OR, USA, 2023, pp. 475-476
8. F. Karami, H. Boutayeb and L. Talbi, " Mm-Wave Monopulse Radar System for Detecting Space Debris in Satellite Exploration Missions," *18th European Conference on Antennas and Propagation* (EuCAP), Glasgow, UK, 2024.

REFERENCES

[1] K. Guan et al., “On millimeter wave and THz mobile radio channel for smart rail mobility,” *IEEE Trans. Veh. Technol*., vol. 66, no. 7, pp. 5658– 5674, Jul. 2017.

[2] B. Ai et al., “Future railway services-oriented mobile communications network,” *IEEE Commun. Mag*., vol. 53, no. 10, pp. 78–85, Oct. 2015.

[3] “NGMN 5G white paper,” NGMN Alliance, Frankfurt, Germany, Tech. Rep., Final deliverable V1.0, Feb. 2015.

[4] F. Lyu et al., “Characterizing urban vehicle-to-vehicle communications for reliable safety applications,” *IEEE Trans. Intell. Transp. Syst*., vol. 21, no. 6, pp. 2586–2602, Jun. 2020.

[5] F. Meneghello, M. Calore, D. Zucchetto, M. Polese and A. Zanella, "IoT: Internet of Threats? a survey of practical security vulnerabilities in real IoT devices," *IEEE Internet Things J*., vol. 6, no. 5, pp. 8182-8201, Oct. 2019.

[6] N. Pathak, P. K. Deb, A. Mukherjee and S. Misra, "IoT-to-the-rescue: a survey of IoT solutions for COVID-19-Like pandemics," *IEEE Internet Things J*., vol. 8, no. 17, pp. 13145-13164, 1 Sept.1, 2021.

[7] J. An et al., "Toward global IoT-enabled smart cities interworking using adaptive semantic adapter," IEEE Internet Things J., vol. 6, no. 3, pp. 5753-5765, June 2019.

[8] D. Yu et al., "Empirical study on directional millimeter-wave propagation in railway communications between train and trackside," *IEEE J. Sel. Areas Commun*, vol. 38, no. 12, pp. 2931-2945, Dec. 2020.

[9] Railisa UIC Statistics. [Online]. Available: https://uicstats.uic.org/select

[10] J. Kim, H. -S. Chung, S. -W. Choi, I. G. Kim and Y. Han, "Mobile hotspot network enhancement system for high-speed railway communication," *11th Euro. Conf. Antennas Propag. (EUCAP)*, 2017, pp. 2885-2889.

[11] R. Hussain and M. S. Sharawi, "5G MIMO antenna designs for base station and user equipment: some recent developments and trends," *IEEE Antennas Propag. Mag*., vol. 64, no. 3, pp. 95-107, June 2022.

[12] M. Aguado, O. Onandi, P. S. Agustin, M. Higuero, and E. J. Taquet, “WiMax on rails,” *IEEE Veh. Technol. Mag*., vol. 3, no. 3, pp. 47–56, Sep. 2008.

[13] A. K. Arya et al., “Shark-fin antenna for railway communications in LTE-R, LTE, and lower 5G frequency bands,” *Progr. Electromagn. Res.*, vol. 167, pp. 83–94, Jul. 2020.

[14] M.-C. Chuang and M. C. Chen, “A mobile proxy architecture for video services over high-speed rail environments in LTE—A networks,” *IEEE Syst. J*., vol. 9, no. 4, pp. 1264–1272, Dec. 2015.

[15] Rath Vannithamby; Shilpa Talwar, "Low-latency radio-interface perspectives for small-cell 5G networks," in Towards 5G: Applications, Requirements and Candidate Technologies, *Wiley*, 2017, pp.275-302.

[16] A. Liu, C. Tao, J. Qiu, et al., “Position-based modeling for wireless channel on high-speed railway under a viaduct at 2.35 GHz’’ *IEEE J. Sel. Areas Commun*., vol. 30, no. 4, pp. 834-845, 2012.

[17] N. Hussain and N. Kim, "Integrated microwave and mm-wave MIMO antenna module with 360∘ pattern diversity for 5G Internet-of-Things," *IEEE Internet Things J*., Early Access.

[18] R. Ebhrahimzadeh, H. Boutayeb, L. Talbi, F. Hyjazie and A. S. Nooramin, "Analysis of Transmit Piano Board Based Metasurface Illuminated by a Dual Polarized Antenna*," IEEE Int. Symp. Antennas Propagation USNC-URSI Radio Sci. Meet. (USNC-URSI)*, Portland, OR, USA, 2023, pp. 653-654.

[19] S. Louati, H. Boutayeb, L. Talbi, K. Hettak and F. Karami, "A reconfigurable SIW antenna array for sub-6GHz 5G communication systems," *2023 IEEE International Symposium on Antennas and Propagation and USNC-URSI Radio Science Meeting (USNC-URSI)*, Portland, OR, USA, 2023, pp. 387-388

[20] R. Chataut, and R. Akl. "Massive MIMO systems for 5G and beyond networks—overview, recent trends, challenges, and future research direction." *Sensors*, 20.10 (2020): 2753.

[21] Y. -F. Tsao, A. Desai and H. -T. Hsu, "Dual-band and dual-polarization CPW fed MIMO antenna for fifth-generation mobile communications technology at 28 and 38 GHz," *IEEE Access*, vol. 10, pp. 46853-46863, 2022.

[22] G. Li et al., "Channel characterization for mobile hotspot network in subway tunnels at 30 GHz band," *IEEE 83rd Vehi. Techno. Conf. (VTC Spring)*, 2016, pp. 1-5.

[23] D. He, B. Ai, C. Briso-Rodriguez, and Z. Zhong, “Train-to-infrastructure channel modeling and simulation in mmWave band,” *IEEE Commun. Mag*., vol. 57, no. 9, pp. 44–49, Sep. 2019.

[24] F. Karami, P. Rezaei, A. Amn-e-Elahi, and JS. Meiguni, “A compact and wideband array antenna with efficient hybrid feed network,” *Int J RF Microw. Computer-Aided Eng*.. 2020 Nov;30(11):e22393.

[25] A. K. Arya, S. Kim, K. Ko and S. Kim, "Antenna for IoT-based future advanced (5G) railway communication with end-fire radiation," *IEEE Internet Things J*., vol. 9, no. 9, pp. 7036-7042, 1 May1, 2022.

[26] R. Hussain, “Shared-aperture slot-based sub-6-GHz and mm-Wave IoT antenna for 5G applications,” *IEEE Internet Things J*., vol. 8, no. 13, pp. 10807–10814, Jul. 2021

[27] B. Xiao, H. Wong, D. Wu and K. L. Yeung, "Design of small multiband full-screen smartwatch antenna for IoT applications," *IEEE Internet Things J.*, vol. 8, no. 24, pp. 17724-17733, 15 Dec.15, 2021.

[28] A. E. Forooshani, A. A. Lotfi-Neyestanak, and D. G. Michelson, “Optimization of antenna placement in distributed MIMO systems for underground mines,” *IEEE Trans. Wireless Commun*., vol. 13, no. 9, pp. 4685–4692, Sep. 2014.

[29] F. Fuschini and G. S. Falciasecca, “A mixed rays—modes approach to the propagation in real road and railway tunnels,” *IEEE Trans. Antennas Propag*., vol. 60, no. 2, pp. 1095–1105, Feb. 2012.

[30] A. Li, K. -M. Luk and Y. Li, "A dual linearly polarized end-fire antenna array for the 5G applications," *IEEE Access*, vol. 6, pp. 78276-78285, 2018,

[31] F. Hyjazie and H. Boutayeb, "Multi-band/wide band printed quad helical antenna," *14th Euro. Conf. Antennas Propag. (EuCAP)*, 2020, pp. 1-3.

[32] Y. Cao, Y. Cai, L. Wang, Z. Qian and L. Zhu, "A review of substrate integrated waveguide end-fire antennas," *IEEE Access*, vol. 6, pp. 66243-66253, 2018.

[33] H. Boutayeb, W. Tong, F. Hyjazie, W. Zhai and X. Feng, "Substrate integrated dual linearly polarized end-fire antenna array operating at 28GHz," *14th Euro. Conf. Antennas Propag. (EuCAP)*, 2020, pp. 1-5.

[34] A. Li and K. -M. Luk, "Millimeter-wave end-fire magneto-electric dipole antenna and arrays with asymmetrical substrate integrated coaxial line feed," *IEEE Op. J. Antennas Propag.*, vol. 2, pp. 62-71, 2021.

[35] A. A. Diman, F. Karami, P. Rezaei, A. Amn-e-Elahi, Z. Mousavirazi, T. Denidni, and A. Kishk, "Efficient SIW-feed network suppressing mutual coupling of slot antenna array," *IEEE Trans Antennas Propag*., vol. 69, no. 9, pp. 6058-6063, Sept. 2021.

[36] F. Karami, P. Rezaei, A. Amn-e-Elahi, M. Sharifi and J. S. Meiguni, "Efficient transition hybrid two-layer feed network: polarization diversity in a satellite transceiver array antenna," *IEEE Antennas Propag. Mag*., vol. 63, no. 1, pp. 51-60, Feb. 2021.

[37] S. V. Sanghami, J. J. Lee and Q. Hu, "Machine learning enhanced blockchain consensus with transaction prioritization for smart cities," *IEEE Internet Things J.* 2022, Early access. doi: 10.1109/JIOT.2022.3175208.

[38] M. Khodaei, H. Boutayeb and L. Talbi, "High efficiency and dual-band rf rectifier circuit for energy harvesting systems," *2023 IEEE International Symposium on Antennas and Propagation and USNC-URSI Radio Science Meeting (USNC-URSI)*, Portland, OR, USA, 2023, pp. 671-672

[39] F. Hyjazie and H. Boutayeb, "Miniaturization of quad port helical antenna for wireless 5G massive MIMO application," *12th European Conference on Antennas and Propagation (EuCAP 2018)*, London, UK, 2018, pp. 1-4.

[40] F. Karami, A. Amn-e-Elahi, H. Boutayeb, F. Hyjazie, and L. Talbi. "A Ku-band SIW diplexer-power divider." *IEEE Int. Symp. Antennas Propag. USNC-URSI Radio Sci. Meeting (AP-S/URSI)*, pp. 2032-2033. July 2022.

[41] https://www.who.int/health-topics/climate-change#tab=tab_1

[42] A. Belova, M. V. Martinovich and V. A. Skolota, "Application of photovoltaic cells with an intelligent control system for railway transport," *13th Int. Sci.-Techn. Conf. Actual Problems Electronics Instrument Eng. (APEIE)*, 2017, pp. 64-68.

[43] H. Boutayeb, X. Feng, W. Zhai, F. Hyjazie, and W. Tong, inventors; Huawei Technologies Co Ltd, assignee. Dual-polarized substrate-integrated 360° beam steering antenna. United States patent US 11,394,114. 2022 Jul 19.

[44] H. Boutayeb, F. Hyjazie, W. Tong, inventors; Huawei Technologies Co Ltd, assignee. Dual-polarized substrate-integrated beam steering antenna. United States patent US 10,854,996. 2020 Dec 1.

[45] D. Guan, Y. Zhang, Z. Qian, Y. Li, M. Asaadi and C. Ding, "A novel 2D multibeam antenna without beamforming network," *IEEE Trans. Antennas Propag*., vol. 64, no. 7, pp. 3177-3180, July 2016.

[46] X. Wang, X. Fang, M. Laabs and D. Plettemeier, "Compact 2D multibeam array antenna fed by planar cascaded butler matrix for millimeter-wave communication," *IEEE Antennas Wireless Propag. Lett*., vol. 18, no. 10, pp. 2056-2060, Oct. 2019.

[47] Y. J. Cheng, W. Hong, and K. Wu, "Millimeter-wave substrate integrated waveguide multibeam antenna based on the parabolic reflector principle," *IEEE Trans. Antennas Propag*., vol. 56, no. 9, pp. 3055–3058, Sep. 2008.

[48] M. Rajabalian and B. Zakeri, "Optimisation and implementation for a nonfocal Rotman lens design," *IET Microw. Antennas Propag*., vol. 9, no. 9, pp. 982–987, Jun. 2015.

[49] H. Boutayeb, W. Tong and F. Hyjazie, "28GHz dual polarized beam steering antenna with substrate integrated frequency selective structure," *2019 13th European Conference on Antennas and Propagation (EuCAP)*, Krakow, Poland, 2019, pp. 1-5.

[50] H. Boutayeb, P. R. Watson, W. Lu and T. Wu, "Beam switching dual polarized antenna array with reconfigurable radial waveguide power dividers," *IEEE Trans. Antennas Propag*., vol. 65, no. 4, pp. 1807-1814, April 2017.

[51] W. Kong, Y. Hu, J. Li, L. Zhang and W. Hong, "2D orthogonal multibeam antenna arrays for 5G millimeter-wave applications," *IEEE Trans. Micro. Theory Tech*., vol. 70, no. 5, pp. 2815-2824, May 2022.

[52] M. Poveda-García, E. Andreu-García, J. García-Fernández, D. C. Rebenaque and J. L. Gómez-Tornero, "Frequency-scanned leaky-wave antenna topologies for two-dimensional direction of arrival estimation in IoT wireless networks," *15th Euro. Conf. Antennas Propag. (EuCAP)*, 2021, pp. 1-5.

[53] YB Li, LL Li, BG Cai, Q Cheng, and TJ Cui, "Holographic leaky-wave metasurfaces for dual-sensor imaging" *Sci. Rep*. 10;5(1):1-7, Dec. 2015.

[54] J. -W. Lian, Y. -L. Ban, H. Zhu and Y. J. Guo, "Uniplanar beam-forming network employing eight-port hybrid couplers and crossovers for 2D multibeam array antennas," *IEEE Trans Micro. Theory Techn*., vol. 68, no. 11, pp. 4706-4718, Nov. 2020.

[55] J. -W. Lian, Y. -L. Ban, Q. -L. Yang, B. Fu, Z. -F. Yu and L. -K. Sun, "Planar millimeter-wave 2D beam-scanning multibeam array antenna fed by compact SIW beam-forming network," *IEEE Trans. Antennas Propag*, vol. 66, no. 3, pp. 1299-1310, March 2018.

[56] S. H. Wang, S. Y. Zheng, K. W. Leung and M. H. Xia, "A self-matched multi-band rectifier for efficient electromagnetic energy harvesting," *IEEE Trans. Circuits Systems I: Regular Papers*, vol. 68, no. 11, pp. 4556-4565, Nov. 2021.

[57] Y. Shi, Y. Fan, Y. Li, L. Yang, and M. Wang, "An efficient broadband slotted rectenna for wireless power transfer at LTE band, " *IEEE Trans. Antennas Propag*., vol. 67, no. 2, pp. 814–822, Feb. 2019.

[58] Song et al., "A novel six-band dual CP rectenna using improved impedance matching technique for ambient RF energy harvesting," *IEEE Trans. Antennas Propag*., vol. 64, no. 7, pp. 3160–3171, Jul. 2016.

[59] T. S. Almoneef, F. Erkmen, and O. M. Ramahi, "Harvesting the energy of multi-polarized electromagnetic waves," *Sci. Rep*., vol. 7, no. 1, Nov. 2017, Art. no. 14656.

[60] Y. Hu, S. Sun, H. Xu, and H. Sun, "Grid-array rectenna with wide angle coverage for effectively harvesting RF energy of low power density, " *IEEE Trans. Microw. Theory Techn*., vol. 67, no. 1, pp. 402–413, Jan. 2019.

[61] Y. Hu, M. Pinuela, P. D. Mitcheson, and S. Lucyszyn, "Ambient RF energy harvesting in urban and semi-urban environments, " *IEEE Trans. Microw. Theory Techn*., vol. 61, no. 7, pp. 2715–2726, Jul. 2013.

[62] P. Zhang, X. Zhang and L. Li, "An optically transparent metantenna for RF wireless energy harvesting," *IEEE Trans. Antennas Propag*., vol. 70, no. 4, pp. 2550-2560, April 2022.

[63] S. Zarbakhsh, M. Akbari, M. Farahani, A. Ghayekhloo, T. A. Denidni and A. -R. Sebak, "Optically transparent subarray antenna based on solar panel for CubeSat application," *IEEE Trans. Antennas Propag.*, vol. 68, no. 1, pp. 319-328, Jan. 2020.

[64] J. Bito, R. Bahr, J. G. Hester, S. A. Nauroze, A. Georgiadis, and M. M. Tentzeris, "A novel solar and electromagnetic energy harvesting system with a 3-D printed package for energy efficient Internet-of Things wireless sensors," *IEEE Trans. Microw. Theory Techn*., vol. 65, no. 5, pp. 1831–1842, May 2017.

[65] A. Ghayekhloo, M. Akbari, M. Afsahi, A. A. Orouji, A. R. Sebak and T. A. Denidni, "Multifunctional transparent electromagnetic surface based on solar cell for backscattering reduction," *IEEE Trans. Antennas Propag.*, vol. 67, no. 6, pp. 4302-4306, June 2019.

[66] K. Niotaki, A. Collado, A. Georgiadis, S. Kim, and M. M. Tentzeris, "Solar/electromagnetic energy harvesting and wireless power transmission," *Proc. IEEE*, vol. 102, no. 11, pp. 1712–1722, Nov. 2014.

[67] K. Niotaki, F. Giuppi, A. Georgiadis, and A. Collado, "Solar/EM energy harvester for autonomous operation of a monitoring sensor platform," *Wireless Power Transf*., vol. 1, no. 1, pp. 44–50, Mar. 2014.

[68] L. Chioukh, H. Boutayeb, D. Deslandes and K. Wu, "Noise and sensitivity of harmonic radar architecture for remote sensing and detection of vital signs," *IEEE Trans. Microw. Theory Tech*., vol. 62, no. 9, pp. 1847-1855, Sept. 2014.

[69] M. Torky, A. E. Hassanein, A. H. El Fiky, and Y. Alsbou, "Analyzing space debris flux and predicting satellites collision probability in LEO orbits based on Petri nets," *IEEE Access*, vol. 7, pp. 83461–83473, 2019.

[70] Y. Liu, S. Chang, Z. Wei, K. Zhang and Z. Feng, "Fusing mmWave Radar with Camera for 3-D Detection in Autonomous Driving," *IEEE Internet Things J.*, vol. 9, no. 20, pp. 20408-20421, 15 Oct.15, 2022.

[71] F. Karami, H. Boutayeb and L. Talbi, "Mm-wave monopulse radar system for detecting space debris in satellite exploration missions," *2024 18th European Conference on Antennas and Propagation (EuCAP)*, Glasgow, United Kingdom, 2024, pp. 1-3.

[72] R. Ebrahimzadeh, S. E. Hosseininejad, B. Zakeri, A. Darvish, M. Khalily and R. Tafazolli, "Ultra-Compact 60-GHz Near-Field Focusing Configuration Using SIW Slot Array Loaded by Transmission Coding Metasurface Lens," *IEEE Trans. Antennas Propag.*, vol. 72, no. 2, pp. 1977-1982, Feb. 2024

[73] Serving European Cooperation and Innovation. *European Space Agency*, The ESA Effect, Paris, France, 2014.

[74] M. I. Skolnik, Radar Handbook. New York, NY, USA: McGraw-Hill, 1970.

[75] L. Chioukh, H. Boutayeb, K. Wu and D. Deslandes, "f/nf harmonic radar system with optimal detection of vital signs," *2012 42nd European Microw. Conf.*, Amsterdam, Netherlands, 2012, pp. 25-28.

[76] X. Xu, J. Hirokawa, and M. Ando, "An E-band slotted waveguide monopulse array antenna with corporate-feed using diffusion bonding of laminated plates," *Proc. ISAP*, Oct. 2016, pp. 308–309.

[77] Z. Sun, S. Liu, Z. Hu, W. He, X. Zheng and Y. Yang, "A Compact dual linearly-polarized single-plane monopulse antenna array based on SIW and strip-line feed," *IEEE Trans. Antennas Propag*., vol. 70, no. 8, pp. 6732-6739, Aug. 2022.

[78] A. Tamayo-Domínguez, J. -M. Fernández-González and M. Sierra-Castañer, "Monopulse radial line slot array antenna fed by a 3-D-printed cavity-ended modified butler matrix based on gap waveguide at 94 GHz," *IEEE Trans. Antennas Propag*., vol. 69, no. 8, pp. 4558-4568, Aug. 2021.

[79] S. A. Khatami, J. Meiguni, A. Amn-e Elahi and P. Rezaei, "Compact via-coupling fed monopulse antenna with orthogonal tracking capability in radiation pattern," *IEEE Antennas Wireless Propag. Lett*., vol. 19, no. 8, pp. 1443-1446, Aug. 2020.

[80] D. C. Lugo, R. A. Ramirez, J. Wang and T. M. Weller, "Multilayer dielectric end-fire antenna with enhanced gain," *IEEE Antennas Wireless Propag. Lett.*, vol. 17, no. 12, pp. 2213-2217, Dec. 2018.

[81] J. Zhang, K. Zhao, L. Wang, S. Zhang and G. F. Pedersen, "Dual-polarized phased array with end-fire radiation for 5G handset applications," *IEEE Trans Antennas Propag*., vol. 68, no. 4, pp. 3277-3282, April 2020.

[82] E. Tolin, A. Bahr and F. Vipiana, "Miniaturized and reconfigurable rat-race coupler based on artificial transmission lines," *IEEE Microw. Wireless Comp. Lett*., vol. 30, no. 4, pp. 375-378, April 2020, doi: 10.1109/LMWC.2020.2972738.

[83] X. Zou, C. -M. Tong, J. -S. Bao and W. -J. Pang, "SIW-fed yagi antenna and its application on monopulse antenna," *IEEE Antennas Wireless Propag. Lett*., vol. 13, pp. 1035-1038, 2014.

[84] F. Karami, H. Boutayeb, A. Amn-e-Elahi and L. Talbi, "Compact broadband rate-race coupler for millimiter-wave applications," *IEEE Int. Symp. Antennas Propag. USNC-URSI Radio Science Meeting (USNC-URSI)*, Portland, OR, USA, 2023, pp. 475-476.

[85] F. Karami, H. Boutayeb, A. Amn-e-Elahi, L. Talbi, and A. Ghayekhloo, "Analysis and design of a diplexing power divider for Ku-band satellite applications" *Sensors*. 2023 Oct 26;23(21):8726..

[86] M. Pakdin, A. Ghayekhloo, P. Rezaei, M. Afsahi, "Transparent dual band Wi-Fi filter for double glazed energy saving window as a smart network" *Microwave Opt. Tech. Lett*. 2019 Nov;61(11):2545-50.

[87] T. Peter, T. A. Rahman, S. W. Cheung, R. Nilavalan, H. F. Abutarboush and A. Vilches, "A novel transparent UWB antenna for photovoltaic solar panel integration and RF energy harvesting," *IEEE Trans. Antennas Propag*., vol. 62, no. 4, pp. 1844-1853, April 2014,

[88] S. Zarbakhsh, and A.R. Sebak, "Multifunctional drone-based antenna for satellite communication" *IEEE Trans. Antennas Propag*. 2022, 70, 7223–7227.

[89] X. Wang. J. Wang, G. Zhang, and J.S. Hong, "Dual-wideband filtering power divider with good isolation and high selectivity" *IEEE Microw. Wirel. Compon. Lett*. 2017, 27, 1071–1073.

[90] L. Wu, H. Yilmaz, T. Bitzer, and A.P.M Berroth, "A dual-frequency Wilkinson power divider: For a frequency and its first harmonic" *IEEE Microw. Wirel. Compon. Lett*. 2005, 15, 107–109.

[91] D. Psychogiou, R. Gómez-García, A.C Guyette, and D. Peroulis, "Reconfigurable single/multi-band filtering power divider based on quasi-bandpass sections" *IEEE Microw. Wirel. Compon*. Lett. 2016, 26, 684–686.

[92] L. Guo, H. Zhu, and A.M. Abbosh, "Wideband tunable in-phase power divider using three-line coupled structure" *IEEE Microw. Wirel. Compon. Lett.* 2016, 26, 404–406.

[93] L. Chiu, and Q.A. Xue, "A parallel-strip ring power divider with high isolation and arbitrary power-dividing ratio" *IEEE Trans. Microw. Theory Tech*. 2007, 55, 2419–2426.

[94] W. Zhai, V. Miraftab, and H. Boutayeb, "Millimeter wave dual-mode diplexer and method" U.S. Patent US 9,660,316, 23 May 2017.

[95] S. Mukherjee, and A. Biswas, "Design of self-diplexing substrate integrated waveguide cavity-backed slot antenna" *IEEE Antennas Wirel. Propag. Lett*. 2016, 15, 1775–1778.

[96] G.L. James, P.R. Clark, and K.J. Greene, "Diplexing feed assemblies for application to dual-reflector antennas" *IEEE Trans. Antennas Propag*. 2003, 51, 1024–1029.

[97] S. Zarbakhsh, and R. Gholami, "A simple UWB antenna with dual stop-band performance using rectangular slot and strip line ended up shorting PIN" *Prog. Electromagn. Res. C*, 2013, 42, 83–94.

[98] D. Zhang, B. Yang, G Li, and L. Shao, "The control system of one space probe small satellite. in spacecraft guidance, navigation control systems" *NASA*: Washington, DC, USA, 2000; Volume 425, p. 49.

[99] M.T. Islam, M. Cho, M. Samsuzzaman, and K. Kibria, "Compact antenna for small satellite applications Antenna Applications Corner" *IEEE Antennas Propag. Mag*. 2015, 57, 30–36.

[100] M. Rohaninezhad, A. Ghayekhloo, M. Afsahi, and T.A. Denidni, "Design of a transparent system for mutual coupling reduction of microstrip array antennas with confined water" *Phys. Status Solidi A*, 2022, 219, 2200082.

[101] E. Ofli, R. Vahldieck, and S. Amari, S, "Novel E-plane filters and diplexers with elliptic response for millimeter-wave applications" *IEEE Trans. Microw. Theory Tech*. 2005, 53, 843–851.

[102] J.M. Rebollar, J.R. Montejo-Garai, and A. Ohoro, "Asymmetric H-plane T-junction for broadband diplexer applications" *Proceedings IEEE Antennas and Propaga. Society Int. Symp., Transmitting Waves of Progress to the Next Millennium. 2000 Digest. Held in Conjunction with: USNC/URSI National Radio Science Meeting*, Salt Lake City, UT, USA, 16–21 July 2000; IEEE: Piscataway, NJ, USA, 2000; Volume 4, pp. 2032–2035.

[103] A. Chakraborty, and S. Dwari, "Analysis of field propagation inside a waveguide diplexer using cavity model analysis," *Int. J. Adv. Microw. Technol*. 2023, 8, 296–300.

[104] S. Roshani, S.I. Yahya, and et.al, "Design of a compact quad-channel microstrip diplexer for l and s band applications" *Micromachines*, 2023, 14, 553.

[105] F. Teberio, I. Arregui, P. Soto, M.A. Laso, V.E. Boria, and M. Guglielmi, "High-performance compact diplexers for Ku/K-band satellite applications" *IEEE Trans. Microw. Theory Tech*. 2017, 65, 3866–3876.

[106] Y. Lin, Y. You, S. Shen, J. Huang, and Y. Lu, "A K-/Ka-band diplexer-integrated simplified rotary joint using gap waveguide technology" *IEEE Microw. Wirel. Technol. Lett*. 2023, 33, 1139–1142

[107] T. Shen, K.A. Zaki, and T.G. Dolan, "Rectangular waveguide diplexers with a circular waveguide common port" *IEEE Trans. Microw. Theory Tech*. 2003, 51, 578–582.

[108] R. Ebrahimzadeh, B. Zakeri, A. Darvish, and S.E. Hosseininejad, "Multi beam scanning programmable metasurface using miniaturized unit cells for 5G applications" J. Electromagnetic Waves and Applications, 36(15), 2164–2177.

[109] X. Feng, H. Boutayeb, F. Hyjazie, W. Zhai, D. Wessel and W. Tong, "360-degree beam steering antenna based on subsrate integrated frequency selective structure," *IEEE Int. Symp. Antennas Propag. USNC-URSI Radio Science Meeting (APS/URSI)*, Singapore, Singapore, 2021, pp. 543-544,

[110] FD Wappi, B Mnasri, A Ghayekhloo, L Talbi, H Boutayeb, "Miniaturized compact reconfigurable half-mode SIW phase shifter with PIN diodes" *Technologies*. 2023 Apr 23;11(3):63.

[111] C. Tang, and S. You, "Design methodologies of LTCC bandpass filters, diplexer, and triplexer with transmission zeros" *IEEE Trans. Microw. Theory Tech.* 2006, 54, 717–723.

[112] J.-X. Xu, and X.Y. Zhang, "Compact high-isolation LTCC diplexer using common stub-loaded resonator with controllable frequencies and bandwidths" *IEEE Trans. Microw. Theory Tech*. 2017, 65, 4636–4644.

[113] D. Chen, L. Zhu, H. Bu, and C. Cheng, "A novel planar diplexer using slotline-loaded microstrip ring resonator" *IEEE Microw. Wirel. Compon. Lett.* 2015, 25, 706–708.

[114] R. Ebrahimzadeh, M. Mousavipour, M. Yazdi, and A. Darvish, "Stub-based 6–18 GHz UWB filter with very steep Rolloff for radar measurement systems" *Proc. IEEE Int. Symp. Antennas Propag*.,—North American Radio Science Meeting, Montreal, QC, Canada, 5–10 July 2020; pp. 1461–1462.

[115] P. Deng, R. Liu, W. Lin, W. Lo, "Design of a microstrip low-pass-bandpass diplexer using direct-feed coupled-resonator filter" *IEEE Microw. Wirel. Compon. Lett*. 2017, 27, 254–256.

[116] S. Louati, L. Talbi, H. Boutayeb, K. Hettak and A. Ghayekhloo, "Reconfigurable SIW phase shifter based on parallel stubs loaded with surface mount P-I-N diodes," *IEEE Trans. Comp., Pack. Manufac. Tech.*, vol. 14, no. 1, pp. 176-179, Jan. 2024

[117] F. Karami, P. Rezaei, A. Amn-e-Elahi, Z. Mousavirazi, T.A. Denidni, and A.A. Kishk, "A compact high-performance patch array with suppressed cross polarization using image feed configuration" *AEU Int. J. Electron. Commun*. 2020, 127, 153479.

[118] F. Karami, H. Boutayeb, A. Amn-e-Elahi, A. Ghayekhloo, and L. Talbi, "Developing broadband microstrip patch antennas fed by SIW feeding network for spatially low cross-polarization situation" *Sensors*, 2022, 22, 3268.

[119] A. Amn-e-Elahi, and P. Rezaei, "SIW corporate-feed network for circular polarization slot array antenna" *Wireless Personal Communications*. 2020 Apr;111(4):2129-36.

[120] R.S. Chen, S. Wong, L. Zhu, Q.-X. and Chu, "Wideband bandpass filter using u-slotted substrate integrated waveguide (SIW) cavities", *IEEE Microw. Wireless Compon. Lett*. 2015, 25, 532–534.

[121] R. Ebrahimzadeh, B. Zakeri, M. Yousefzadeh, and S.E. Hosseininejad, "Optically controlled reconfigurable substrate integrated waveguide slot array antenna for 5G applications" *Proc. 10th Int. Symp. Telecomm. (IST)*, Tehran, Iran, 15–17 December 2020; pp. 107–110.

[122] S. Kiani, and P. Rezaei, "Microwave substrate integrated waveguide resonator sensor for non-invasive monitoring of blood glucose concentration: low cost and painless tool for diabetics" *Measurement*, 2023, 219, 113232.

[123] C. Chen, C. Lin, B. Tseng, and S. Chang, "High-isolation and high-rejection microstrip diplexer with independently controllable transmission zeros" *IEEE Microw. Wirel. Compon. Lett*. 2014, 24, 851–853.

[124] M.F. Hagag, M.A. Khater, M.D. Hickle, and D Peroulis, "Tunable SIW cavity-based dual-mode diplexers with various single-ended and balanced ports" *IEEE Trans. Microw. Theory Tech*. 2018, 66, 1238–1248.

[125] C. Segura-Gómez, A. Palomares-Caballero, Á.; Alex-Amor, J. Valenzuela-Valdés, and P. Padilla, "Modular design for a stacked SIW antenna array at Ka-band" *IEEE Access*, 2020, 8, 158568–158578.

[126] J. Hautcoeur, A. Ghayekhloo, K. Hettak, L. Talbi, H. Boutayeb, and K. Wu, "60 GHz frequency sensor antenna for short-range millimeter-wave detection application" *IEEE Sens. Lett*. 2022, 6, 1–4.

[127] T.V. Duong, W. Hong, Z.C. Hao, W.C. Huang, J.X. Zhuang, and V.P. Vo, "A millimeter wave high-isolation diplexer using selectivity improved dual-mode filters" *IEEE Microw. Wireless Compon. Lett*. 2016, 26, 104–106.
[128] K. Song, Y. Zhou, Y. Chen, A.M. Iman, S.R. Patience, and Y. Fan, "High-isolation diplexer with high frequency selectivity using substrate integrate waveguide dual-mode resonator" *IEEE Access*, 2019, 7, 116676–116683.
[129] H. Boutayeb, "Reconfigurable radial waveguides with switchable artificial magnetic conductors" U.S. Patent US 10,903,569, 26 January 2021.
[130] A. M. Hussien, Y. S. Farag, A. F. Daw and M. A. Abdalla, "A Novel ultra compact four-way power divider with integrated filtering function for WLAN applications," *IEEE Int. Symp. Antennas Propag. & USNC/URSI National Radio Science Meeting*, San Diego, CA, USA, 2017, pp. 465-466.
[131] M. Sorkherizi, A. Vosoogh, A.A. Kishk, and P.S. Kidal, "Design of integrated diplexer-power divider" *Proc. IEEE MTT-S Int. Microwave Symp., IMS*, San Francisco, CA, USA, 22–27 May 2016.
[132] F. Karami, H. Boutayeb and L. Talbi, "Directive Millimeter-Wave End-Fire Diplexing Antenna for IoT Applications," *IEEE Internet of Things Journal*, vol. 10, no. 22, pp. 19874-19882, 15 Nov.15, 2023.
[133] F. Karami, H. Boutayeb, and L. Talbi, "IoT-based Transceiver Antenna System for 5G Future High-Speed Train Communications" *17th Euro. Conf. Antennas Propag. (EuCAP)*, Florence, Italy, 26–31 March 2023; pp. 1–3.
[134] A. Kumar, D. Chaturvedi, and S. Raghavan, "Dual-Band, dual-fed self-diplexing antenna" *Proc. 13th Euro. Conf. Antennas Propag.* (EuCAP), Krakow, Poland, 31 March–5 April 2019; pp. 1–5.
[135] A. Vosoogh, A.U. Zaman, J. Yang, M. Sharifi, and A.A. Kishk, "An E-band antenna-diplexer compact integrated solution based on gap waveguide technology" *Proc. IEEE Int. Symp. Antennas Propag*., San Diego, CA, USA, 9–14 July 2017; pp. 1–2.
[136] G. Zhang, Z. Qian, and J. Yang, "Design of a compact microstrip power-divider diplexer with simple layout" *Electron. Lett*. 2018, 54, 1007–1009.
[137] A. Ghayekhloo, M. Afsahi and A. A. Orouji, "An optimized checkerboard structure for cross-section reduction: producing a coating surface for bistatic radar using the equivalent electric circuit model," *IEEE Antennas Propag. Mag.*, vol. 60, no. 5, pp. 78-85, Oct. 2018.
[138] D. M. West, How 5G technology enables the health internet of things, Center Technol. Innovat. Brookings, Washington, DC, USA, Jul. 2016.
[139] O. Jo, Y.-K. Kim, and J. Kim, "Internet of Things for smart railway: feasibility and applications," *IEEE Internet Things J.*, vol. 5, no. 2, pp. 482–490, Apr. 2018.
[140] J. Hannula, T. Saarinen, J. Holopainen and V. Viikari, "Frequency reconfigurable multiband handset antenna based on a multichannel transceiver," *IEEE Trans. Antennas Propag*., vol. 65, no. 9, pp. 4452-4460, Sept. 2017.
[141] S. Louati, L. Talbi, K. Hettak and H. Boutayeb, "28 GHz digital SIW phase shifter using embedded PIN diodes," *IEEE Int. Symp. Antennas Propag. USNC-URSI Radio Sci. Meeting (AP-S/URS*I), Denver, CO, USA, 2022, pp. 848-849
[142] S. A. Ali, M. Wajid, A. Kumar and M. Shah Alam, "Design challenges and possible solutions for 5G SIW MIMO and phased array antennas: a review," *IEEE Access*, vol. 10, pp. 88567-88594, 2022.
[143] F. Karami, P. Rezaei, A. Amn-e-Elahi and A. Abolfathi, "An x-band substrate integrated waveguide fed patch array antenna: overcoming low efficiency, narrow impedance bandwidth, and cross-polarization radiation challenges," *IEEE Antennas Propag. Mag*., vol. 63, no. 5, pp. 25-32, Oct. 2021.
[144] L. Varghese, B. Choudhury and R. U. Nair, "Design optimization of 15–34 GHz Ultrawideband Tapered Slot Antenna Array with Defected Ground," *IEEE Indian Conf. Antennas Propag.*, India, 2018, pp. 1-4.
[145] S. Sugawara, Y. Maita, K. Adachi, K. Mori, and K. Mizuno, "A mm-wave tapered slot antenna with improved radiation pattern," *IEEE MTT-S Int. Microw. Symp. Dig*., Denver, CO, USA, Jun. 1997, pp. 959–962.
[146] H. Sato, Y. Takagi, and K. Sawaya, "High gain antipodal Fermi antenna with low cross polarization," *IEICE Trans. Commun*., vol. E94-B, pp. 2292–2297, Aug. 2011.

[147] A. Amn-e-Elahi, F. Karami, P. Rezaei, H. Boutayeb, F. Hyjazie and L. Talbi, "A sequentially rotated 2×2 helix antenna array," *IEEE Int. Symp. Antennas Propag. USNC-URSI Radio Sci. Meet. (AP-S/URSI)*, pp. 371-372, July 2022.

[148] R. He et al., "High-speed railway communications: From GSM-R to LTE-R," *IEEE Veh. Technol. Mag.*, vol. 11, no. 3, pp. 49–58, Sep. 2016.

[149] T.-Y. Yun et al., "A 10- to 21-GHz, low-cost, multifrequency, and full-duplex phased-array antenna system," *IEEE Trans. Antennas Propag.*, vol. 50, no. 5, pp. 641–650, May 2002.

[150] A. Vosoogh, M. S. Sorkherizi, A. U. Zaman, J. Yang, and A. A. Kishk, "An integrated Ka-band diplexer-antenna array module based on gap waveguide technology with simple mechanical assembly and no electrical contact requirements," *IEEE Trans. Microw. Theo. Techn.*, vol. 66, no. 2, pp. 962-972, Feb. 2018.

[151] K. Hu, Y. Zhou, S. K. Sitaraman and M. M. Tentzeris, "Fully additively manufactured flexible dual-band slotted patch antenna for 5G/mm-wave wearable applications," *IEEE Int. Symp..Antennas Propag. USNC-URSI Radio Sci. Meet.* (AP-S/URSI), Denver, CO, USA, 2022, pp. 878-879.

[152] F. Karami, P. Rezaei, A. Amn-e-Elahi, A. Abolfathi, and A.A. Kishk, "Broadband and efficient patch array antenna fed by substrate integrated waveguide feed network for Ku-band satellite applications, " *Int. J. RF Microw. Computer-Aided Eng*.,31(9):e22772. Sep. 2021.

[153] P. Sohrabi, P. Rezaei, S. Kiani, and M. Fakhr, "A symmetrical SIW-based leaky-wave antenna with continuous beam scanning from backward-to-forward through broadside" *Wireless Networks*. 2021 Nov;27:5417-24.

[154] S. Louati, L. Talbi, K. Hettak and H. Boutayeb, "Design of a SIW variable phase shifter for beamforming antenna systems," *IEEE 19th Int. Symp. Antenna Tech. Applied Electromag. (ANTEM*), Winnipeg, MB, Canada, 2021, pp. 1-2.

[155] S. Louati, H. Boutayeb, K. Hettak and L. Talbi, "New reconfigurable SIW phase shifter with transverse CPW-based stubs and PIN Diodes," *IEEE Inte. Symp. Antennas Propag. USNC-URSI Radio Sci. Meet. (AP-S/URSI),* Denver, CO, USA, 2022, pp. 850-851.

[156] S. Kiani, P. Rezaei, M. Karami, and R.A. Sadeghzadeh, "Band-stop filter sensor based on SIW cavity for the non-invasive measuring of blood glucose" *IET Wireless Sensor Systems*. 2019 Feb;9(1):1-5.

[157] F. Alessandri, M. Giordano, M. Guglielmi, G. Martirano and F. Vitulli, "A new multiple-tuned six-port Riblet-type directional coupler in rectangular waveguide," *IEEE Trans. Microwave Theo. Techn.*, vol. 51, no. 5, pp. 1441-1448, May 2003.

[158] R. J. Mailloux, Phased Array Antenna Handbook. Boston, MA, USA: Artech House, 2005.

[159] O. O'Conchubhair, P. McEvoy and M. J. Ammann, "Integration of antenna array with multicrystalline silicon solar cell," *IEEE Antennas Wireless Propag. Lett*., vol. 14, pp. 1231-1234, 2015.

[160] H. Lim and K. W. Leung, "Transparent dielectric resonator antennas for optical applications," *IEEE Trans. Antennas Propag*., vol. 58, no. 4, pp. 1054-1059, April 2010.

[161] F. Karami, H. Boutayeb, and L. Talbi " Millimeter-wave broadband monopulse radar antenna for space debris detection," *IEEE Internet Things J.*, vol. 11, no. 18, pp. 30376-30384, 15 Sept. 2024.

[162] H. Lamb, "Space agencies turn focus on small space debris," Eng. Technol., vol. 13, no. 1, pp. 48–49, Feb. 2018.

[163] https://www.starlink.com/

[164] https://www.nhm.ac.uk/discover/what-is-space-junk-and-why-is-it-a-problem.html#:~:text=Space%20junk%2C%20or%20space%20debris,have%20fallen%20off%20a%20rocket.

[165] H. Boutayeb, P. R. Watson, and T. Kemp, inventors; Huawei Technologies Co Ltd, assignee. Apparatus and method of a dual polarized broadband agile cylindrical antenna array with reconfigurable radial waveguides. United States patent US9502765B2. 2014 June 30.

[166] J. Soleiman Meiguni, SA. Khatami, A. Amn-e-Elahi, "Compact substrate integrated waveguide mono-pulse antenna array" *Int. J. RF Microw. Comput.-Aided Eng*.. 2018 Jan;28(1):e21155.

[167] K Ding, C Gao, Y Wu, D Qu, B Zhang, and Y Wang, "Dual-band and dual-polarized antenna with endfire radiation" *IET Microw. Antennas Propag.*. 2017 Oct;11(13):1823-8.

[168] M. M. Samadi Taheri, A. Abdipour, S. Zhang and G. F. Pedersen, "Integrated millimeter-wave wideband end-fire 5G beam steerable array and low-frequency 4G LTE antenna in mobile terminals," *IEEE Trans. Veh. Techn.*, vol. 68, no. 4, pp. 4042-4046, April 2019.

[169] F. Karami, A. Amn-e-Elahi, JS Meiguni, P Rezaei, TA Denidni, AA Kishk, "Monopulse antenna array based on three-modes with orthogonal radiation beams," *AEU-Int. J. Elec. Commun*. 2021 Dec 1; 142:154015.

[170] F. Karami, H. Boutayeb, L. Talbi, K. Hettak, and A. Ghayekhloo " Multifunctional switched-beam antenna integrated with solar cell for vehicular to satellite communication," *IEEE Trans. Veh. Techn*., vol. 73, no. 3, pp. 3457-3468, March 2024, doi: 10.1109/TVT.2023.3323419.

[171] A. Amn-E-Elahi, P. Rezaei, F. Karami, F. Hyjazie, and H. Boutayeb, "Analysis and design of a stacked PCBs-based quasi-Helix antenna," *IEEE Trans. Antennas Propag*., vol. 70, no. 12, pp. 12253-12257, Dec. 2022.

[172] C. L. Mak, K. M. Luk, K. F. Lee, and Y. L. Chow, “Experimental study of a microstrip patch antenna with an L-shaped probe,” *IEEE Trans. Antennas Propag*., vol. 48, no. 5, pp. 777–783, May 2000.

[173] T. T. Mo, Q. Xue and C. H. Chan, "A Broadband compact microstrip rat-race hybrid using a novel CPW inverter," *IEEE Trans Mic. Theory Tech*., vol. 55, no. 1, pp. 161-167, Jan. 2007.

[174] C. H. Ho, L. Fan, and K. Chang, “New uniplanar coplanar waveguide hybrid-ring couplers and magic-T’s,” *IEEE Trans. Microw. Theory Tech*., vol. 42, no. 12, pp. 2440–2448, Dec. 1994.

[175] DM. Pozar. Microwave engineering. John wiley & sons; 2011 Nov 22.

[176] K. S. Yngvesson, D. H. Schaubert, T. L. Korzeniowski, E. L. Kollberg, T. Thungren, and J. F. Johansson, “Endfire tapered slot antennas on dielectric substrates,” *IEEE Trans. Antennas Propag*., vol. 33, no. 12, pp. 1392–1400, Dec. 1985.

[177] A. Amn-e-Elahi, and P. Rezaei, "Axial corrugated horn antenna with elliptical tapering function", *J. Elec. Comput. Engineering Innovations (JECEI).* Jan. 2017, 1;5(1):65-9.